Novel Technologies for Mode-Locking of Solid-State Lasers

NIELS MEISER

KTH Engineering Sciences

Doctoral Thesis
Department of Applied Physics
KTH – Royal Institute of Technology
Stockholm, Sweden 2013

Novel Technologies for Mode-Locking of Solid-State Lasers

Laser Physics
Department of Applied Physics
KTH – Royal Institute of Technology
106 91 Stockholm
Sweden

ISBN 978-91-7501-840-9
TRITA-FYS 2013:48
ISSN 0280-316X
ISRN KTH/FYS/--13:48—SE
Akademisk avhandling som med tillstånd av Kungliga Tekniska Högskolan framlägges till offentlig granskning för avläggande av teknologie doktorsexamen tisdagen den 5 november kl. 10:00
i sal FA32, Albanova, Roslagstullsbacken 21, KTH, Stockholm.
Avhandlingen kommer att försvaras på engelska.
Printed by Universitetsservice US AB, Stockholm 2013

Niels Meiser
Novel Technologies for Mode-Locking of Solid-State Lasers
Laser Physics, Department of Applied Physics,
KTH – Royal Institute of Technology, 106 91 Stockholm, Sweden
ISBN 978-91-7501-840-9, TRITA-FYS 2013:48, ISSN 0280-316X, ISRN KTH/FYS/--13:48—SE

Abstract

The subject of this thesis is the investigation of novel technologies for mode-locking of diode-pumped, solid-state lasers. Novel saturable absorbers are used: quantum dots (QDs) and carbon nanotubes (CNTs), which both are low-dimensional nanoformations. In addition, mode-locking by cascaded nonlinearities is explored.

Absorber structures containing self-assembled InGaAs QDs are characterised in detail by pump-probe experiments, time-resolved photoluminescence spectroscopy, and measurement of the nonlinear reflectivity. The samples show sub-picosecond relaxation times of the reflectivity, modulation depths between 0.18 % and 2.9 %, as well as low saturation fluences on the order of 1–10 $\mu J/cm^2$. The structures' design parameters are related to their transient and nonlinear performance.

The characterised QD saturable absorbers are then used for mode-locking of diode-pumped, solid-state lasers, delivering picosecond pulses with optical spectra in the region of 1020–1040 nm. In particular, a QD absorber with a saturation fluence of 4 $\mu J/cm^2$ and a relaxation time <200 fs is successfully employed for fundamental mode-locking of an Yb:KYW laser at a repetition rate of 1 GHz. This laser emits pulses with a duration of 1.7 ps at an output power of 339 mW. Apart from this, an Yb-thin-disc laser is demonstrated, emitting pulses with a duration of 1.6 ps at an output power of 13 W, thereby showing, that the absorber withstands fluences of up to 2.4 mJ/cm^2 without being damaged.

An absorber with a linear loss of only 1 % is obtained by embedding CNTs in a thin plastic film, coated onto a glass substrate. Using this absorber, mode-locking of an optically-pumped semiconductor disc-laser is achieved. The laser emits pulses with a duration of 1.12 ps at a repetition rate of 613 MHz and with an average output power of 136 mW.

For cascaded mode-locking, a periodically-poled KTP crystal is placed inside a laser cavity and the two second-order nonlinearities from second-harmonic generation and back-conversion are used to emulate a third-order nonlinearity with an effective nonlinear refractive index of $2.33 \cdot 10^{-17}\,m^2/W$. For precise control of the nonlinearity, the laser's spectrum is fixed to a wavelength of 1029.1 nm by a volume Bragg grating. The laser emits pulses with a duration of 16 ps at a repetition rate of 210 MHz and with an output power of 690 mW.

Swedish abstract

Denna doktorsavhandling behandlar nya tekniker för modlåsning av diodpumpade fasta-tillståndslasrar. För modlåsningen har tre nya mättnadsbara absorbatorer utvecklats och undersökts. Dessa är lågdimensionella nanostrukturer i form av kvantpricksfilmer i halvledare och kolnanorör i polymerfilmer. Den tredje tekniken som har undersökts är att använda kaskaderade andra-ordningens ickelinjäriteter.

I den första delen av projektet studerade jag halvledarstrukturerna med självorganiserade InGaAs kvantprickar som hade tillverkats av externa projektpartner. De detaljstuderades genom pump-probexperiment, tidsupplöst fotoluminescensspektroskopi och mätning av den ickelinjära reflektansen. Proverna uppvisade relaxationstider i subpikosekundområdet med modulationsdjup på mellan 0,18 % och 2,9 %, och låga mättnadsintensiteter (1–10 µJ/cm^2). Strukturernas designparametrar relaterades till deras dynamiska och ickelinjära egenskaper och de mest lämpade strukturerna för modelåsning valdes ut för de påföljande laserexperimenten.

De mättningsbara kvantpricksabsorbatorerna som användes för att konstruera olika fasta-tillståndslasrar resulterade i pikosekundpulser i våglängdsintervallet 1020–1040 nm. Specifikt använde jag en kvantpricksabsorbator med 4 µJ/cm^2 mättnadsintensitet och med relaxationsstid <200 fs för modlåsning av en kompakt Yb:KYW-laser, vilket gav en repetitionsfrekvens av 1,036 GHz och en pulslängd på 1,7 ps vid en uteffekt på 339 mW. Utöver detta användes dessa absorbatorer i en Yb-*thin-disc-laser* som gav 1,6 ps långa pulser vid en medeluteffekt av 13 W. Härmed kunde vi visa att absorbatorerna tål höga intensiteter, minst upp till 2,4 mJ/cm^2, utan att skadas.

Kolnanorör erhöll vi från en annan samarbetspartner. Dessa kolnanorör blandades i en polymerlösning som spanns ut till en tunn film på ett glassubstrat och därefter härdades. Via pump-probexperiment kunde vi välja ut prover med lämplig mättnadsbar absorption för de planerade lasrarnas designvåglängd, dvs. med lämplig koncentration av kolnanorör och lämplig tjocklek. Med en sådan absorbator, med en linjär förlust av endast 1 %, kunde vi konstruera en modlåst, optiskt-pumpad halvledarlaser, vilken resulterade i 1,12 ps långa pulser med repetitionsfrekvensen 613 MHz och med 136 mW medeleffekt.

För experimenten med modlåsning via kaskaderade ickelinjära effekter användes en periodiskt polad KTP kristall. I denna teknik utnyttjas en balansering av två andra-ordningens ickelinjära processer: frekvensdubbling och återkonvertering till grundfrekvensen, för att emulera en tredje-ordningens ickelinjär effekt med ett effektivt ickelinjärt brytningesindex av $2,33 \cdot 10^{-17}$ m^2/W. För att låsa laserfrekvensen och bandbredden, och därmed stabilisera modlåsningen, användes ett volymbraggitter som ändspegel i laserkaviteten. Med volymbraggittret låstes laserns våglängd till 1029,1 nm. Den slutliga modlåsta lasern emitterade 16 ps långa pulser, med en repetitionsfrekvens av 210 MHz och med 690 mW uteffekt.

Contents

List of publications

This thesis is based on the following publications:

I V. Pasiskevicius, N. Meiser, M. Butkus, B. Resan, K. J. Weingarten, R. Hogg, Z. Zhang,
Semiconductor Quantum-Dot Saturable Absorber Mirrors for Mode-Locking Solid-State Lasers,
in *The Physics and Engineering of Compact Quantum Dot-based Lasers for Biophotonics*, E. Rafailov (ed.), Wiley-VCH Verlag GmbH & Co. KGaA, Berlin, pp. 123–172 (2014)
ISBN 978-3-527-41184-9

II N. Meiser, S. Marcinkevicius, and V. Pasiskevicius,
Transient behaviour of quantum-dot saturable absorber mirrors at varying excitation fluence,
(manuscript)

III N. Meiser, K. Seger, V. Pasiskevicius, H. Jang, E. Rafailov, and I. Krestnikov,
Gigahertz repetition rate mode-locked Yb:KYW laser using self-assembled quantum-dot saturable absorber,
Applied Physics B, **110(3)**, pp. 327–333 (2013)

IV K. Seger, N. Meiser, S. Y. Choi, B. H. Jung, D.-I. Yeom, F. Rotermund, O. Okhotnikov, F. Laurell, and V. Pasiskevicius,
Carbon nanotube mode-locked optically-pumped semiconductor disk laser,
Optics Express, **21(15)**, pp. 17806–17813 (2013)

V N. Meiser, K. Seger, V. Pasiskevicius, A. Zukauskas, and C. Canalias,
Cascaded mode-locking of a spectrally controlled Yb:KYW laser,
(accepted for publication in Applied Physics B)

Author contributions

My contributions in the original publications have been the following:

I I wrote Section 4.5, entitled *Quantum-Dot Saturable Absorbers for Mode-Locking of Solid-State Lasers at 1 μm*, which was afterwards edited by Valdas Pasiskevicius. I designed and conducted the experiments presented in that section with assistance from Theo van Oijen (pump-probe experiments) and Kai Seger (gigahertz-repetition-rate laser). I analysed the data presented in that section with assistance from Valdas Pasiskevicius.

II I conducted the experiments with assistance from Saulius Marcinkevicius. I analysed the data and wrote the paper together with the co-authors.

III I designed the experiments. I conducted the experiments together with Kai Seger. I analysed the data and wrote the paper with assistance from the co-authors.

IV I conducted the laser experiment together with Kai Seger. I assisted Sun Young Choi in fabricating the carbon nanotube absorber. I assisted in analysing the data and writing the paper together with the co-authors.

V I designed and conducted the experiments with assistance from Kai Seger. The PPKTP sample was fabricated by Andrius Zukauskas and Carlota Canalias. I analysed the data and wrote the paper with assistance from Valdas Pasiskevicius.

The quantum-dot saturable absorber samples used and investigated in Publications I-III were fabricated by Igor Krestnikov. I took part in designing the sample structures.

Further publications

- K. Seger, N. Meiser, S. Tjörnhammar, A. Zukauskas, C. Canalias, V. Pasiskevicius, and F. Laurell, *Intra-cavity frequency-doubled Yb:KYW laser using periodically poled Rb-doped KTP with a volume Bragg grating input coupler*, Applied Physics B, (2013).

- K. Seger, N. Meiser, C. Canalias, V. Pasiskevicius, and F. Laurell, *Tunable, passively Q-switched single-longitudinal-mode Nd:YVO_4 laser using a chirped volume Bragg grating*, Applied Physics B, **109(1)**, 99–103 (2012).

- N. Meiser and V. Pasiskevicius, *Full characterisation of semiconductor saturable absorbers for mode-locking of solid-state lasers*, Optik och Fotonikdagarna 2012, Oct. 18–19, Stockholm, Sweden.

- K. Seger, N. Meiser, S. Y. Choi, B. H. Jung, F. Rotermund, O. Okhotnikov, V. Pasiskevicius, and F. Laurell, *Carbon nanotube mode-locked semiconductor disk laser*, Optik och Fotonikdagarna 2012, Oct. 18–19, Stockholm, Sweden.

- V. Pasiskevicius, N. Meiser, and F. Rotermund, *Quantum dots and carbon nanotubes for ultrashort pulse generation in lasers*, 2nd Sweden-Japan Workshop on Nanophotonics and Related Technologies 2012, Jun. 18–19, Stockholm, Sweden.

- N. Meiser, K. Seger, V. Pasiskevicius, E. Rafailov, and I. Krestnikov, *Quantum dot saturable absorber mode-locked Yb:KYW-laser with 1 GHz repetition rate*, EPS-EQOD Europhoton 2010, Aug. 29–Sep. 3, Hamburg, Germany.

- S. Rausch, T. Binhammer, A. Harth, N. Meiser, F. X. Kärtner, and U. Morgner, *Few-cycle femtosecond waveform synthesizer*, CLEO/QELS 2008, May 4–9, San Jose, USA.

The research presented in this thesis is based on experiments that have been performed in the Laser Physics group at the Royal Institute of Technology (KTH), in Stockholm from 2009 to 2013. The main supervisor has been Prof. Valdas Pasiskevicius, the second supervisor has been Prof. Fredrik Laurell.

Acknowledgements

This thesis has been made possible by my two supervisors, Valdas Pasiskevicius and Fredrik Laurell. Thank you for accepting me to conduct doctoral studies in the Laser Physics group and providing valuable feedback and discussions on the way.

This work has been supported by the Swedish Research Council (VR) through its Linnæus Center of Excellence ADOPT and the European Community FP7 FASTDOT project. The semiconductor saturable absorbers have been provided by Igor Krestnikov from Innolume GmbH, Dortmund, Germany, in the context of the FASTDOT project. Research on CNT saturable absorbers at the Laser Physics group received an initial support by an ADOPT mini-project grant for PhD students.

I gratefully acknowledge support in the form of discussions on as well as supplying of CNTs and CNTSAs from the group of Fabian Rotermund at Ajou University, Suwon, Korea. In particular, I am indebted to Sun Young Choi for sharing her knowledge on CNTSA fabrication.

I am thankful for having had the opportunity of conducting experiments at Uwe Morgner's group at Leibniz Universität, Hannover, Germany. In particular, I received valuable help from Jana Kampmann, regarding dispersion measurements with a white-light interferometer and from Moritz Emons, regarding operation and measurements concerning the mode-locked thin-disc laser.

Additionally, I am grateful for receiving help from Saulius Marcinkevicius at the Department of Materials and Nanophysics at KTH, by providing the opportunity to conduct time-resolved photoluminescence spectroscopy experiments and discussing and interpreting the measured data.

My work also profited from several student projects, which were conducted at the Laser Physics group: First, Hoon Jang provided the first steps towards characterisation of the saturable absorbers' nonlinear reflectivity and the simulation of the electric field and dispersion in saturable-absorber structures as part of his Master thesis work. Second, Theo van Oijen assisted in the optimisation of the pump-probe setup and subsequent measurement of the saturable absorbers' transient response during his internship.

Many thanks to all those colleagues that made work more pleasant by their company. In particular, I am much obliged to those who proof-read this thesis and contributed with their critical comments. I am also thankful for innumerable technical and non-technical discussions, assistance during experiments, kayaking and the regular coffee breaks. I commit special thanks to Kai Seger, for continuous help and support and many hours of companionship, be it in the lab, at Don Corleone or out in the woods and on the water. Similarly, thanks to Martin Levenius and Hoon Jang, for offtopic discussions and activities outside our work.

Finally, the encouragement from family and friends from outside the work has been crucial, especially, my parents' unconditional support. Thank you all.

List of abbreviations and symbols

The following abbreviations and symbols for physical quantities and constants are used throughout this thesis.

	Abbreviations
APM	additive pulse mode-locking
CNT	(single walled) carbon nanotube
CML	cascaded mode-locking
CW	continuous wave
CWML	continuous-wave mode-locking
DCB	1,2-dichlorobenzene
DPSSL	diode-pumped solid-state laser
FWHM	full width at half maximum
GD	group delay
GDD	group delay dispersion
HR	high-reflective
KLM	Kerr-lens mode-locking
KTP	potassium titanyl phosphate ($KTiOPO_4$)
MBE	molecular beam epitaxy
ML	mode-locked, mode-locking
NIR	near infrared (spectral region)
NLM	nonlinear mirror
OPSDL	optically-pumped semiconductor disc-laser
PMMA	poly(methyl methacrylate)
PmPV	poly[(m-phenylenevinylene)-co-(2,5-dioctoxy-p-phenylenevinylene)]
PL	photoluminescence
PP	periodically poled
QS	Q-switched, Q-switching
QSML	Q-switched mode-locking
QD	quantum dot
QDSA	quantum-dot saturable absorber
QPM	quasi-phase matching, quasi-phase matched
QW	quantum well
RF	radio frequency
SA	saturable absorber
SAM	self-amplitude modulation
SHG	second-harmonic generation
SPM	self-phase modulation
SSA	semiconductor saturable absorber
TPA	two-photon absorption
WL	wetting layer

	Symbols
$a(t)$	electric field envelope
c	speed of light in vacuum
d_{eff}	effective nonlinearity
$\mathcal{E}$	electric field amplitude
E	energy
F	fluence
F_{p}	pulse fluence
F_{sat}	saturation fluence
F_2	two-photon absorption fluence
h ($\hbar$)	Planck's constant (reduced)
I	intensity
k	wave vector
Δk	wave-vector mismatch
L	length (of a medium)
m	mass
n	refractive index
n_2	nonlinear refractive index
P	power
q	loss
R	reflectivity
R_{ns}	non-saturable reflectivity, i.e. maximum reflectivity
ΔR	modulation depth
ΔR_{ns}	non-saturable loss (i.e. $1 - R_{\text{ns}}$)
S	saturation parameter
t	time (on a short scale)
T	time (on a long scale) or transmission
T_{r}	round-trip time (in a cavity)
ε_0	vacuum permittivity
γ	self-phase modulation coefficient
λ	wavelength
Λ	poling or patterning period of a material
ξ	field enhancement factor
τ_{r}	recovery time
τ_{p}	pulse duration
ϕ	phase
ϕ_{nl}	nonlinear phase
$\chi^{(n)}$	nth-order nonlinear susceptibility
ω	radial frequency

The symbols as listed above may be complemented by further subscripts, which are then explained in the surrounding text. Also, not all symbols used are listed, instead, those with a local scope have been omitted.

Part I

Theory and Experiments

Chapter 1

Introduction

Since the first observations of bursts of so-called *giant pulses* emitted from lasers during the mid 1960s [1, 2], mode-locked lasers have emerged as an important technology, enabling numerous applications in research and industry. Starting with the demonstration of a regular train of pulses emitted from a mode-locked dye laser in 1972 [3], equally-spaced pulses with similar amplitude, featuring pulse durations on the order of 1 ps and less, became available. Nowadays, a vast range of mode-locked lasers is available, from solid-state lasers emitting pulses with durations of only a few femtoseconds, all-semiconductor lasers with repetition rates of several tens of gigahertz, to high power, thin-disc and fibre lasers with average output powers exceeding 100 W [4]. In addition, various amplification and pulse shaping schemes have been invented for further tailoring the output of mode-locked lasers according to specific application needs. Although mode-locked lasers primarily operate in the near infrared spectral region, continuing progress in nonlinear optics greatly extends this range into both directions, further into the mid infrared as well as into the ultraviolet spectral regions.

High peak powers and short pulse durations are the key features offered by mode-locked lasers and have led to rapid developments in numerous fields, including microstructuring and micromachining [5], biomedical imaging [6], chemistry [7], telecommunication [8] as well as metrology [9]. In research, mode-locked lasers have been used to resolve ultrafast biochemical processes occurring on a time scale of tens of femtoseconds [10]. The combination of femtosecond pulses and high peak intensities facilitates studying of strong light-matter interactions and has opened up the field of attosecond science [11] and extreme nonlinear optics [12]. Highly stabilised, mode-locked lasers have revolutionised the fields of spectroscopy [9] and now belong to the most precise instruments for measuring frequencies [13]. Apart from the ground-breaking impact on fundamental research, mode-locked lasers also have numerous practical applications. In all-optical communication networks, mode-locked lasers have enabled multiplexing of several communication channels in the

time domain [14]. Mode-locked pulses are also advantageous in micromachining applications, where precise and clean cutting and ablation is desired [15]. Examples of medical applications are the uses of mode-locked lasers as light sources for optical coherence tomography [16], which exploits the broad bandwidth of the optical spectrum, or for nonlinear microscopy [17], which provides better resolution than ordinary single-photon microscopy. Consequently, in view of the many diverse applications, the optimal mode-locked laser source does not exist, but, instead, the huge range of demands have created the need for a wide variety of lasers.

1.1 Highlights of mode-locked laser development

The following section highlights some important developments in the field of mode-locked lasers. Since the field is quite wide and has seen extensive development over a very long time, the selection is subjective and represents but a small fraction. However, various aspects relevant for this thesis are portrayed in more detail at the beginning of each chapter. For further information on mode-locked lasers and saturable absorbers, the reader is referred to recent review articles, e.g. [4, 18–22], which will present a good starting point. More detailed treatments are available in, e.g. [23–27].

One important step in the development of mode-locked lasers has been the demonstration of a mode-locked Ti:Sapphire laser together with the technique of *Kerr-lens mode-locking* (KLM) at the beginning of the 1990s [28, 29]. These systems were continuously improved and soon proved to be extremely versatile devices which are still widely used even today. Several other laser gain media have been successfully mode-locked using the KLM technique [30–32]. However, some limitations exist, because the mechanism relies on the gain medium's third-order nonlinearity, i.e. a material parameter, and also puts constraints on the laser cavity design, e.g. with respect to the resonator's optical stability. With the advent of reliable laser diodes [33] for efficient pumping of new solid-state laser materials [19, 34], a wider wavelength range as well as more efficient laser systems were available. In order to exploit the benefits of these diode-pumped solid state lasers (DPSSLs), though, more versatile mode-locking mechanisms were needed.

A crucial step towards mode-locking of DPSSLs was the development of engineered semiconductor saturable absorbers (SSAs) [35, 36], further boosting the field of mode-locked solid-state lasers during the 1990s. These devices comprised an all-semiconductor structure incorporating a thin, absorbing film (quantum well, QW) inside a layered super-structure. Such a device would then show the specific behaviour needed for mode-locking, namely, saturation (or bleaching) of the absorption transition at higher intensities, hence its name, saturable absorber. The choice of material as well as the exact design of the super-structure offer a tailored solution according to the demands of the laser system in question. In the years following the first demonstrations, innumerable lasers were mode-locked using this technology (a comprehensive overview can be found in, e.g. [26]), delivering pulse durations as

short as 13 fs [37], pulse energies exceeding 25 µJ [38], and fundamental repetition rates of up to 160 GHz [39]. Despite the increased potential for engineering, the initial saturable absorbers based on QWs were limited by the number of possible material systems for the growth of the multi-layer structures. More flexibility is offered by semiconductor quantum dots (QDs) [40], for which the absorption wavelength can be tuned by the physical size of the QDs. The peculiar properties offered by QD-based saturable absorbers (QDSAs) especially facilitate mode-locking of low energy lasers, such as semiconductor lasers [20, 41], but also DPSSLs operated at high repetition rates or with picosecond pulse durations.

Following the semiconductor technologies, carbon nanotubes (CNTs) emerged as a promising technology for fabrication of saturable absorbers [42]. After fabrication of CNTs had been improved and the amount of remaining impurities had been reduced, mode-locking of a DPSSL with a saturable absorber based on CNTs (CNTSA) was demonstrated in 2005 [43]. CNTSAs have since been used with similar success as the above mentioned semiconductor absorbers for mode-locking of solid-state lasers (see, e.g. [21, 22] for a comprehensive list). One principal advantage of CNTs is the versatility in depositing them for use as a saturable absorber. For example, CNTs can be incorporated into a plastic host matrix and spin-coated or spray-coated onto almost any optical component in a laser cavity, transmissive or reflective, thereby enabling a wide range of different absorber designs.

In general, however, it can be observed, that the trend towards engineered solutions is not limited to mode-locking techniques, but it also appears in, e.g. nonlinear optics (periodically-poled, quasi-phase matched materials), optical fibres (photonic crystal fibres), and simple mirrors (multi-layer, dielectric mirrors, dispersion compensating mirrors, volume Bragg gratings). This is the result of a desire for a single technology being applicable to as many applications as possible in order to reduce costs and efforts of development. The aim of this thesis, then, is to explore novel and more versatile technologies for mode-locking of lasers, based on engineered materials and devices, in order to extend the operational range of current and future mode-locked lasers.

1.2 Subject of the thesis

In this thesis, I will present novel concepts for mode-locking of solid-state lasers. I show, that self-assembled InGaAs QDs exhibit fast relaxation times and low saturation fluences, by characterising a set of QDSAs with respect to their transient behaviour and nonlinear response. I conclude, that two defining parameters, saturation fluence and modulation depth, are only weakly coupled in QDSAs, thus offering a certain degree of freedom in their design. I then demonstrate that the properties of QDSAs are suitable for mode-locking of Yb:KYW lasers, emitting picosecond pulses at various repetition rates. In particular, I present the first Yb:KYW laser mode-locked with QDs at a repetition rate of 1 GHz. Subsequently, I show that CNTs can be used for simple fabrication of low-loss, saturable ab-

sorbers. I then demonstrate the feasibility of this technology for mode-locking of a low-gain laser, by presenting the first optically-pumped semiconductor disc-laser being mode-locked with a CNTSA. As an alternative to saturable absorbers as used in the aforementioned demonstrations, I further demonstrate KLM-like mode-locking by exploiting an effective third-order nonlinearity created by cascading of two second-order nonlinearities. Before, this has only been shown in small-gain bandwidth laser media. I then demonstrate that cascaded mode-locking can be extended to wide-gain bandwidth media by employing a volume Bragg grating (VBG) for spectral control, and present the first Yb:KYW laser mode-locked by cascaded second-order nonlinearities.

1.3 Outline

This thesis is based on the original publications labelled I to V, which are reproduced in Part II of the printed version. Regarding Publication I, only that part of the chapter which I contributed is reproduced. The rest of the chapter is omitted due to copyright restrictions and the extent of the material. Part I of this thesis contains eight chapters, providing an introduction to the theoretical background of these publications and summarising their results.

The concepts of mode-locking, and especially saturable-absorber mode-locking, are outlined in Chapters 2 and 3, where Chapter 2 focuses on mode-locking in general and Chapter 3 treats QDSAs for mode-locking of lasers.

Chapters 4–7 contain experimental results from the characterisation of a number of QDSAs (Chapter 4) and results from mode-locking of lasers using various QDSAs (Chapter 5), a CNTSA (Chapter 6), and cascaded second-order nonlinearities (Chapter 7). Each chapter features an introductory overview of the respective technology and ends with a summary of the main findings. Finally, all conclusions are summarised in Chapter 8.

Chapter 2

Mode-Locking of Lasers

In this chapter, an overview of the development of mode-locking of solid-state lasers and the accompanying theory is presented. These topics have been extensively covered by the literature (e.g. [4, 24, 25, 44, 45]) and, thus, the information given here is necessarily limited and has been chosen to facilitate an understanding of the experimental work described in this thesis. A very general introduction to mode-locking is provided in the beginning and the various physical mechanisms at work in a mode-locked laser are discussed. Following this, two techniques for passive mode-locking are described, namely, saturable-absorber mode-locking and mode-locking with a Kerr nonlinearity.

2.1 Overview

A mode-locked laser differs from a continuous (CW) laser by containing an additional element that is responsible for providing a periodic modulation of the signal circulating in the cavity. The formation of a pulse is easily understood in the time domain as the result of an amplitude modulation at the cavity round-trip frequency. A periodic loss created by the modulator, in combination with the gain from the laser medium, creates a periodic variation of the total gain for the circulating signal. Ideally, only a short time-window of net gain exists while a net loss prevails for the rest of the time. This window will then promote the formation of a pulse circulating in the cavity.

The amplitude modulation will also give rise to side-bands in the laser's optical spectrum, i.e. in the frequency domain. If the modulation frequency is the same as the cavity mode spacing, then the side-bands will be resonant and experience gain. Thus, the modulation frequency is a crucial parameter for successful mode-locking. It is also important to note, that all modes in the spectrum created in this way are equidistant and have a fixed phase relationship to each other as opposed to the case of a multi-mode CW laser. Therefore, the modulator's role can also be understood

from a frequency-domain picture such as to fix and maintain the relations between the modes of a multi-mode spectrum. The modulator also acts like a clocking signal, providing the reference frequency for the mode-spacing. Superposition of these modes then leads to a periodic time-domain signal. A maximum possible amplitude is achieved at those points in time at which all relative phases equal zero and, consequently, constructive interference of all modes occurs. The technique of using a device or mechanism for periodic modulation and locking of the relative phases of the laser's mode spectrum, is called *mode-locking*.

The numerous devices and mechanisms, that have been employed since the first demonstration of a mode-locked laser, can be divided into two principal classes for mode-locking concerning the type of modulator used: active and passive. Active mode-locking involves a modulator that is driven by external electronics, e.g. an accousto-optic modulator (AOM). For passive mode-locking, on the other hand, the interaction of the circulating signal with a nonlinearly responding element inside the cavity is exploited. Since the modulator's nonlinear response usually involves saturation of an absorption transition in order to decrease the loss for high-intensity signals, the modulator is often called a *saturable absorber*. Passively mode-locked lasers perform significantly better in terms of timing jitter and other noise figures, since they do not suffer from a mismatch of the modulation and the round-trip frequency. They also avoid the need for additional electronics equipment. Although passively mode-locked lasers thus appear more elegant with respect to their operation, their design and construction turn out to be more demanding.

Development

A first analysis of the coupling of longitudinal modes in an actively modulated laser was presented in [46–48]. However, by using saturable dyes, pulses could be obtained without active modulation, using instead passive modulation by a saturable absorber mechanism [1]. CW mode-locking was not achieved at first, instead, the mode-locked pulses would form the substructure of a longer Q-switched pulse. The complicated dynamics of this experiment prevented a simple analytical description. Nevertheless, a CW mode-locked laser was soon demonstrated and comprised of a dye laser with Rhodamine 6G as the gain medium and another dye[1] as the saturable absorber [3]. The system delivered laser pulses with a duration of 1.5 ps, although it was at that time not understood why the pulses were that short while the life-times of the dyes were orders of magnitude longer. This was later explained by the suitable combination of absorber and gain saturation [49]. These observations, and the interest in a general understanding of mode-locking, triggered a thorough theoretical examination of the issue, which separated the problem into the two cases of an absorber exhibiting either a slow or a fast relaxation time (as compared to the pulse width) [50, 51].

[1] The used dye was DODCI (3,3'-diethyl oxadicarbocyanine iodide).

The case of a fast absorber was at first not applicable to the lasers existing at that time, but that changed with the demonstration of additive-pulse mode-locking (APM) [52, 53]. In APM, a laser oscillator consists of two coupled cavities, of which one would contain a Kerr-medium and, thus, introduce a significant nonlinear phase shift. This would then lead to pulse shortening upon interference with the pulse from the second cavity (which contains the gain medium) [54]. As a Kerr-medium, a piece of optical fibre had been used. This was motivated by the preceding work on the propagation of solitons in optical fibres [55–57] and the idea to employ this mechanism for pulse shaping. Hence, the demonstration in [52] was also called a *soliton laser*. Following these developments, a Ti:Sapphire laser with a pulse duration of 60 fs was demonstrated without the use of any external cavity or any additional saturable absorber [28]. The apparent *self mode-locking* became known as Kerr-lens mode-locking (KLM), as it was recognised, that the Kerr-effect in the gain medium led to focusing of high-intensity signals which would then be subject to reduced losses at an aperture (in the case of [28], formed by the overlap of the pump and the laser mode in the gain medium) [58]. This truly fast absorber mechanism facilitated the development of lasers delivering ultra-short pulses, down to a pulse duration of a few femtoseconds [59]. Today, Ti:Sapphire lasers with a pulse duration below 6 fs are commercially available.

However, KLM has two important drawbacks: first, the mode-locking is usually not self-starting, i.e. an initial loss modulation has to be provided and second, the strength of the nonlinear effect is tied to the material. In general, the strength of the nonlinear phase modulation has to be considered when targeting lasers with high repetition rates (>1 GHz) or with picosecond pulse durations, in which the peak intensity of the pulses is reduced. Hence, from a technological point of view it is highly desirable to switch to components which can be engineered and to mechanisms that do not fully rely on the gain medium's properties in order to access a wider range of wavelengths as well as to somewhat relax the constraints on the cavity design and the output characteristics.

A solution that permitted a considerable engineering of the saturable absorber was eventually provided with the development of semiconductor-saturable-absorber (SSA) mirrors [36]. This development is separately described in Chapter 3. The analytical treatment is based on the above mentioned treatment by Haus. The saturable absorber was understood as being a slow absorber, especially in the case of femtosecond lasers. Subsequent analytical treatments, together with experimental observations, clarified the role of the saturable absorber [60]. While a fast saturable absorber can be directly responsible for shaping of ultra-short pulses in a mode-locked laser, it was at first believed, that no short pulses could be obtained with slow absorbers. After it had been observed, however, that pulses which were significantly shorter than the absorber's relaxation time could be obtained [35, 61], it was pointed out that additional soliton dynamics can be utilised as the dominant pulse-shaping mechanism [62, 63]. This had already been observed for fast-absorber mode-locking, where additional soliton shaping further reduced the pulse duration [64, 65]. The absorber then stabilises the mode-locked operation by removing any

noise emerging between subsequent pulses. An important additional feature is that it also facilitates self-starting of a KLM laser [66]. SSAs soon proved to be an excellent technology for mode-locking of ion-doped, solid-state lasers, which was up until then difficult to achieve because of their small emission cross-sections and long upper laser-level lifetimes as compared to dye lasers [67]. The long life-times would lead to Q-switching instabilities, which, however, could be mediated by proper absorber design, once a theoretical analysis of the problem established a stability criterion [68–70]. The possibility to engineer saturable absorbers was further expanded by the progression from absorbers based on semiconductor quantum wells to such based on quantum dots, which also showed sub-picosecond relaxation behaviour, but exhibited the potential to realise small saturation fluences and small modulation depths at the same time [71, 72] (see also Chapter 3). This simplified mode-locking of low-pulse-energy systems, such as high-repetition rate solid-state and semiconductor lasers [20]. Further promising technologies emerged with the new materials carbon nanotubes and graphene [22, 42, 73], which can feature fast relaxation times below 100 fs [74], thus approaching the regime of a fast absorber (see also Chapter 6). These developments in saturable-absorber technology enabled the development of an ever growing number of mode-locked lasers.

Nevertheless, a certain degree of advanced engineering is also possible in the case of the original Kerr-lens-based fast absorber technique. The approach of Mollenauer and Stolen [52], e.g. already suggested the incorporation of an additional component to create a suitable nonlinear phase shift and thus removing the demand of a strong third-order nonlinearity in the gain medium. By noting that two cascaded second-order nonlinearities can constitute an effective third-order nonlinearity, a strong Kerr-effect can be obtained with nonlinear crystals used for second-harmonic generation (SHG) [75, 76]. The first demonstration of this employed a bulk KTP ($KTiOPO_4$, potassium titanyl phosphate) crystal [77]. However, engineering of the nonlinearity became first available with the fabrication of quasi-phase matched (QPM) crystals [78–80]. Cascading of engineered, second-order nonlinearities then offers the possibility to apply mode-locking by a Kerr-nonlinearity to a wider range of lasers. This approach is explored in Chapter 7.

The master equation of mode-locking

The following section is considered to be an introduction to a theoretical description of mode-locking, by elaborating on some of the aspects mentioned in the preceding section. It is further meant to provide a starting point for the understanding of saturable-absorber mode-locking and mode-locking with a Kerr nonlinearity, the mechanisms of which are exploited for mode-locking of lasers in Chapters 5–7.

A theoretical description of mode-locking is usually based on a circulating pulse model, i.e. imposing cyclic boundary conditions on a signal of amplitude $a(t)$ circulating in a laser cavity. This signal is then subject to amplitude and phase changes when passing the various cavity elements. Depending on the properties of these elements, the entire signal also evolves as a function of the number of round-trips or,

in general, as a function $a(t, T)$ of a time T on the time-scale of the round-trip time T_r. If the changes per round-trip are small, the system is commonly approximated by a differential equation for the amplitude function [81]:

$$\frac{1}{T_\mathrm{r}}\frac{\partial}{\partial T}a(t,T) = \left[g - \ell + \left(\mathrm{i}D + \frac{1}{{\Delta\omega_\mathrm{f}}^2}\right)\frac{\partial^2}{\partial t^2} - \mathrm{i}\gamma\left|a(t,T)\right|^2\right]a(t,T)\ . \tag{2.1}$$

This equation is known as the *master equation* (or the *generalised Ginzburg-Landau equation*). Gain and loss are expressed by the functions g and ℓ, respectively. The gain's frequency dependence is accounted for by a filtering term dependent on the filter bandwidth $\Delta\omega_\mathrm{f}$. The quantity D models the second-order dispersion, leading to a dissipation of the laser pulse energy over time, and γ is the self-phase modulation (SPM) coefficient (or Kerr-coefficient). The strength of the SPM mainly depends on the signal's intensity, $I = \left|a(t,T)\right|^2/A_\mathrm{eff}$, where A_eff is the effective mode area. Filtering and dispersion can each act to balance SPM. The imaginary components will directly act on the phase of the signal $a(t, T)$, while the real arguments act on its amplitude. Higher order terms can be added, which has been found to have important consequences, e.g. for a proper description of the APM mechanism [82] or to find stable solutions in all normal dispersion (ANDi) fibre lasers [83, 84]. Further improvements can be made by including higher-order dispersion and gain dispersion functions.

Equation (2.1) has several possible solutions [85], however, these usually have to be obtained numerically. Of particular interest is the case of an equilibrium situation, in which the gain and the loss cancel each other. If, in addition, the gain filtering effect is neglected, the master equation reduces to the nonlinear Schrödinger equation and a simple, analytical solution for the pulse shape a with pulse duration τ can be found:

$$a(t) = a_0\,\mathrm{sech}\left(\frac{t}{\tau}\right)\ . \tag{2.2}$$

Here, a_0 is the maximum amplitude and τ denotes the pulse duration[2]. This solution only exists, if the dispersive term and the SPM term have the correct signs and, thus, balance each other out. This so-called *soliton mode-locking* is achieved in the case of a perfect interplay between dispersion and SPM [37, 64, 86]. If this is not the case, e.g. if the influence of SPM is too weak, then additional action is necessary in order to achieve mode-locking. This action can be provided by a modulated loss in the form of a saturable absorber, which is of practical importance, since a saturable absorber can potentially be engineered to meet the requirements for successful mode-locking.

The loss-function ℓ is separated into a linear and a nonlinear component, namely:

$$\ell = q_\mathrm{lin} + q(t)\ . \tag{2.3}$$

[2]The pulse duration as used here is related to the FWHM (full width at half maximum) pulse duration τ_p via $\tau = 2\cdot\cosh^{-1}\sqrt{2}\cdot\tau_\mathrm{p} \approx 1.76\cdot\tau_\mathrm{p}$.

Without the effects of soliton mode-locking (i.e. with small γ), the absorber's transient behaviour becomes the defining mechanism for a laser's mode-locking dynamics. But, even if soliton mode-locking is dominant, a saturable absorber contributes to stabilisation of the mode-locking by removing noise arising outside the pulse, emphasising its twofold role.

2.2 Pulse shaping in mode-locked lasers

Several mechanisms contribute to the formation and maintenance of a pulse circulating inside a laser cavity, as can be seen from Equation (2.1). The various effects can be divided into either acting on the amplitude (real part) or acting on the phase (imaginary part). Gain and loss functions directly influence the pulse amplitude in the time domain; filtering effects from, e.g. a finite gain bandwidth affect the spectral amplitude. Dispersion and SPM then change the spectral phase. However, it is evident that all these effects are linked to each other. Dispersion, for example, will also change the pulse's temporal shape. In the following, some of these effects and their consequences shall be examined further.

Gain and loss

As was already mentioned in the beginning of this chapter, the explicit gain and loss dynamics are of major importance for successful mode-locking (see Figure 2.1). However, the exact size of the net-gain window is not necessarily the defining property for the resulting pulse duration. Intuitively, pulse formation can only occur inside the window of net gain, i.e. no pulses longer than this window are supported. Any energy that is shed into the net-loss region by, e.g. dispersive effects is per definition lost. As was mentioned in the beginning, it was observed early on, that the pulse duration can be substantially shorter than the gain window. This has im-

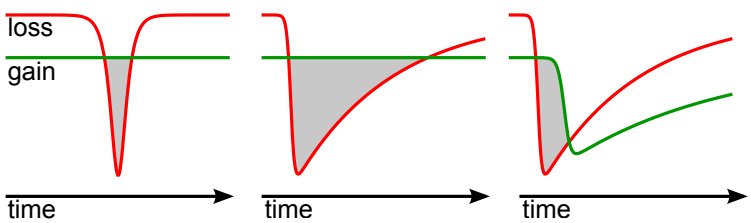

Figure 2.1: Loss (red line) and gain (green line) as a function of time. The gray area indicates the window of net gain for different combinations of the recovery time constants of the two functions: (a) fast absorber and no gain saturation, (b) slow absorber and no gain saturation, (c) slow absorber and saturable gain.

portant technological implications, since it is then possible to obtain short pulses from laser gain media with weak or no gain saturation in combination with a slow saturable absorber, such as in ion-doped, solid-state lasers, mode-locked with an SSA (as in Figure 2.1b). The reason is the formation of pulses that are periodically sustained by the interplay of dispersion and SPM, as was already briefly mentioned above [37, 62]. In this situation, a slow absorber will act stronger on a pulse's front part and the trailing part of the pulse will face the absorber in a different state than the pulse's front did. The pulse is pushed back in time, effectively merging with noise that has built up inside the remaining net-gain region in its wake. If the gain is too strong, any noise following the main pulse is amplified before merging with the pulse, and mode-locking operation becomes unstable [87]. The absorber's recovery time then defines the acceptable regime of operation and, thus, ultimately puts a constraint on the possible pulse duration.

If the soliton effect cannot be exploited, the absorber's recovery time becomes more important, as in the above mentioned dye lasers. In this case, the saturation behaviour is similar for the gain and the loss and a narrow net-gain window can be realised, despite long recovery times [2, 49, 88] (see Figure 2.1c). In media without gain saturation, picosecond pulses could be obtained by using dyes with fast relaxation dynamics, although their number is limited. Nd-doped gain media delivered pulses with durations of a few picoseconds, when using dyes with relaxation time constants on the order of 10 ps [89, 90].

As a conclusion, a fast absorber recovery time is generally beneficial. For very fast relaxation, the fast absorber description becomes valid, significantly simplifying the situation since the gain saturation dynamics now become less important.

Dispersion

The propagation of an electromagnetic wave through a medium is characterised by the medium's refractive index (among other parameters). The term *dispersion* refers to the observation, that the value of the refractive index depends on the wave's frequency. For a signal with a given optical spectrum, this leads to different velocities for the various spectral components. This effect has important consequences for the design and operation of mode-locked lasers. Since a mode-locked laser pulse corresponds to a relatively broad optical spectrum, dispersion will cause a phase difference between the various frequency components over time. Depending on the exact situation, the pulse might only broaden (i.e. disperse) or its shape being distorted.

Dispersion is quantified by a Taylor series of the frequency dependent phase ϕ (or, more general, the wave vector k).

$$\phi(\omega, z) = \phi_0 + kz = \phi(\omega_0) + (\omega - \omega_0) \left.\frac{\partial \phi}{\partial \omega}\right|_{\omega_0} + \sum_{n=2}^{\infty} \frac{(\omega - \omega_0)^n}{n!} \left.\frac{\partial^n \phi}{\partial \omega^n}\right|_{\omega_0} \tag{2.4}$$

The term $\frac{\partial^n \phi}{\partial \omega^n}$ denotes the n-th order dispersion, which has units of seconds to the power of n (s^n). The definition of the acquired phase presented here includes the propagation length z; however, an alternative formulation may treat this as a variable parameter separately and instead give the dispersion in units of s^n/m. This, as well as the expansion of the k-vector instead of the phase, is commonly used in problems dealing with propagation in fibres.

First-order dispersion is referred to as *group delay* (GD). It describes the observation that the carrier wave and the envelope function propagate with different velocities (phase and group velocity). First-order dispersion preserves the overall pulse shape, but is responsible for a temporal delay and the evolution of the carrier-envelope offset phase.

Second-order dispersion or *group delay dispersion* (GDD) creates a phase difference between the different parts of a signal's optical spectrum. The differing propagation velocities affect the temporal shape of the signal. For positive GDD, low-frequency components will be faster, thus leading to a redistribution of the frequency spectrum's components in time. This will usually lead to a longer pulse duration, as the various frequency components disperse. A dispersed (or *chirped*) pulse can be re-compressed by using GDD with the opposite sign. The effective power dispersion over time is a concern in mode-locked lasers in which the pulse has to be preserved over a number of round-trips.

Higher-order dispersion is often negligible, but its impact grows with spectral bandwidth, which makes it important when aiming for few-cycle pulse durations. However, third-order dispersion (TOD) can be observed to have an impact in femtosecond lasers. The effect of the quadratic frequency dependence is an asymmetric distortion of the pulse shape, as opposed to the symmetric change from GDD.

Control over a laser cavity's net dispersion can be realised in a number of ways. Since dispersion in mostly positive for the materials and wavelength ranges of interest, mechanisms and devices to introduce negative dispersion have to be provided[3]. Prism pairs were used early on and they still provide a reliable mechanism for controlling intra-cavity dispersion [91]. A more convenient solution are dielectric mirrors with a special layer structure showing the desired amount of dispersion in a specific wavelength interval [92, 93]. These mirrors are especially useful when facing constraints with respect to space, e.g. when constructing high-repetition rate lasers. If the design of a specific laser is fixed and a semiconductor-based absorber is used, dispersion compensation can also directly be integrated into the saturable absorber by optimisation of the absorber's layered structure.

Self-phase modulation

As the term already suggests, *self-phase modulation* (SPM) describes a modulation of an electro-magnetic signal's phase induced by the signal itself. The physical origin

[3]The situation can also be naturally advantageous, e.g. in fibre lasers around 1300 nm where regular fibres made from fused silica exhibit zero dispersion.

of this effect is due to a third-order nonlinear susceptibility $\chi^{(3)}$. As a consequence, the effect is present in every material, as opposed to second-order nonlinearities, which are absent in materials with a certain symmetric configuration. However, the effect strongly depends on the intensity of the input signal, which makes it very weak for CW signals but potentially influential for ultra-short laser pulses with high peak intensities. In transparent materials, i.e. if the signal's frequency is far from any resonance, the third-order nonlinearity has, in good approximation, a real value and can be expressed as an intensity dependent change of the materials refractive index (see e.g. [27]):

$$n(t) = n_0 + n_2 \cdot I(t) \ . \tag{2.5}$$

The strength of the intensity dependent contribution is quantified by the nonlinear refractive index n_2, which is related to the third-order nonlinear susceptibility by the expression $n_2 = 3/4 \cdot \mathrm{Re}(\chi^{(3)})/(\varepsilon_0 c n_0^2)$ and given in units of m^2/W. Since the phase acquired by a signal propagating through a medium directly depends on the medium's refractive index, the time-dependent refractive index (Equation (2.5)) leads to an additional time-dependent and nonlinear phase contribution:

$$\phi_{\mathrm{nl}}(t) = n_2 \frac{\omega_0 L}{c} I(t) = \gamma I(t) \ . \tag{2.6}$$

In this equation, ω_0 is the signal's centre frequency and L is the physical length of the nonlinear medium. Equation (2.6) also defines the SPM coefficient γ as used in the master equation (2.1)[4].

The phase modulation subsequently results in new frequency components and, thereby, broadens the optical spectrum. This effectively corresponds to an energy transfer from the carrier frequency into its side-bands and a change of the shape of the optical spectrum. The temporal shape, on the other hand, is preserved. However, the additional spectral components now permit shortening of the temporal shape according to Fourier-theory. This can either be realised by suitable dispersion in the frame of soliton shaping or by a spectrally limiting filter which, in the presence of SPM, consequently cuts off the edges of the pulse. A spectral filter is also naturally provided by the laser medium's gain bandwidth as well as the acceptance bandwidth of the cavity mirrors. However, the latter can also be specifically engineered. The influence of a bandwidth limiting cavity element was demonstrated in Publication V and is also described in Chapter 7.

SPM in dielectric gain media as discussed above is usually a non-resonant effect, since the involved wavelengths are far away from resonances. Saturable absorbers, however, are inherently operated close to resonance, so the $\chi^{(3)}$ nonlinearity should be much larger. The strength of the effect is further related to the carrier population inside the semiconducting material [94]. Especially in a slow absorber, the trailing part of a pulse will experience a larger carrier population than the leading part. The result is an additional temporal change of the refractive index which in

[4] In some descriptions, the definition of the SPM coefficient does not include the interaction length L.

turn gives rise to SPM. The effect is stronger towards the semiconductors bandgap, i.e. its resonance. The total refractive index change is mainly composed of individual contributions from band filling (Burstein-Moss effect) and bandgap shrinkage (bandgap renormalisation). Although both effects counteract each other, a considerable index change can be realised. Free carrier absorption also contributes, but its influence is relatively small close to the bandgap. SPM in an absorber creates an asymmetric spectrum with additional components on the short wavelength side [87]. In lasers based on dielectric gain media, the effect is usually small, since the absorber is comparatively short. For semiconductor lasers though, it has to be considered, because the gain medium is equally short and often made from the same material [95, 96].

2.3 Saturable-absorber mode-locking

Considering the importance of an absorber's influence, a more specific description of the loss function in Equation (2.1) is desirable. For this purpose, saturable absorbers have been divided into fast and slow absorbers, depending on their relaxation time constant being fast or slow when compared to the laser pulse duration (as mentioned in the beginning). For a fast absorber, the response is assumed to be instantaneous resulting in an intensity-dependent loss given by:

$$q_\mathrm{f} = \frac{q_0}{1 + \frac{I}{I_\mathrm{S}}} \ . \tag{2.7}$$

If the intensity I equals the absorber's saturation intensity I_S, the loss is one half of the total modulation depth q_0. For small modulation depths, Equation (2.7) can be approximated as follows:

$$q_\mathrm{f} \approx q_0 - q_0 \frac{I}{I_\mathrm{S}} = q_0 - \delta \left|a\right|^2 \ . \tag{2.8}$$

It has to be noted, that the parameters q_f and q_0 are dimensionless numbers and represent the round-trip loss as used in the master equation (2.1). The absorber's nonlinear contribution leads to self-amplitude modulation (SAM) with the corresponding SAM coefficient δ, similar to SPM, acting on the amplitude instead of the phase.

In case of a slow absorber, the loss is instead a function of the pulse fluence F_p relative to the absorber's saturation fluence F_sat:

$$q_\mathrm{s} = q_0 \exp\left[-\frac{F_\mathrm{p}}{F_\mathrm{sat}}\right] \ . \tag{2.9}$$

The above equation[5] is the result of solving the differential equation

$$\frac{\mathrm{d}q_\mathrm{s}}{\mathrm{d}t} = \frac{q_\mathrm{s} - q_0}{\tau_\mathrm{r}} - \frac{I}{F_\mathrm{sat}} q \ , \tag{2.10}$$

in which it is assumed that the recovery time τ_r is long compared to the pulse duration and that the absorber is fully relaxed before the next pulse arrives. It is clear from Equations (2.7) and (2.9) that the two types of absorbers act quite differently on a laser pulse. While a fast absorber acts over the whole pulse duration, a slow absorber will primarily affect a pulse's front part, whereas the rest of the pulse may pass being less affected. As was briefly mentioned above, this is of particular interest if the circulating pulse is subject to dispersion or SPM, since the absorber's action then appears frequency dependent, resulting in a spectral shift.

Q-switching instabilities

Instabilities introduced by relaxation oscillations are a major concern for mode-locked lasers, depending on the life-time in the gain medium. These can lead to so-called *Q-switched mode-locking* (QSML), where the mode-locked pulse train is additionally modulated by a slow amplitude variation as opposed to CW mode-locking, where all the pulses in the train have the same amplitude (see Figure 2.2). For solid-state lasers, the modulation frequency is typically on the order of several kilohertz to megahertz and manifests itself as sidebands in the radio-frequency (RF) spectrum of the laser (see Appendix A.1). It is possible to derive a stability criterion, that puts constraints on the absorber parameters, from a rate equation approach for the gain, the loss, and the intra-cavity power [62, 68, 97]. The main result for the stability against QSML is obtained from a linearisation of the differential equation set and with the assumption of a slow saturable absorber:

$$E_\mathrm{p} \left| \frac{\mathrm{d}q}{\mathrm{d}E_\mathrm{p}} \right|_{\bar{E_\mathrm{p}}} < \frac{T_\mathrm{r}}{\tau_\mathrm{l}} + \frac{E_\mathrm{p}}{E_\mathrm{sat,L}} \tag{2.11}$$

Here, $E_\mathrm{sat,L}$ is the saturation energy of the gain medium and $\bar{E_\mathrm{p}}$ denotes the steady-state pulse energy. It can be observed that the stability is increased, if the upper laser-level life-time τ_l is short compared to the cavity round-trip time T_r and if the gain medium's saturation energy $E_\mathrm{sat,L}$ is small. On the other hand, stability can also be improved by reducing the derivative of the modulation with respect to the pulse energy which is a direct measure of the saturable absorber's modulation depth q_0. By assuming that the modulation is small and that the absorber is operated above its saturation fluence, Equation (2.11) can be further simplified:

$$E_\mathrm{p}^2 > E_\mathrm{sat,L} \cdot E_\mathrm{sat,A} \cdot q_0 \ . \tag{2.12}$$

[5] The time dependent behaviour is given by: $q_\mathrm{s} = q_0 \exp\left[-\int_0^t \frac{|a(t)|^2}{E_\mathrm{sat}}\right]$. Equation (2.9) follows after integration over a whole pulse.

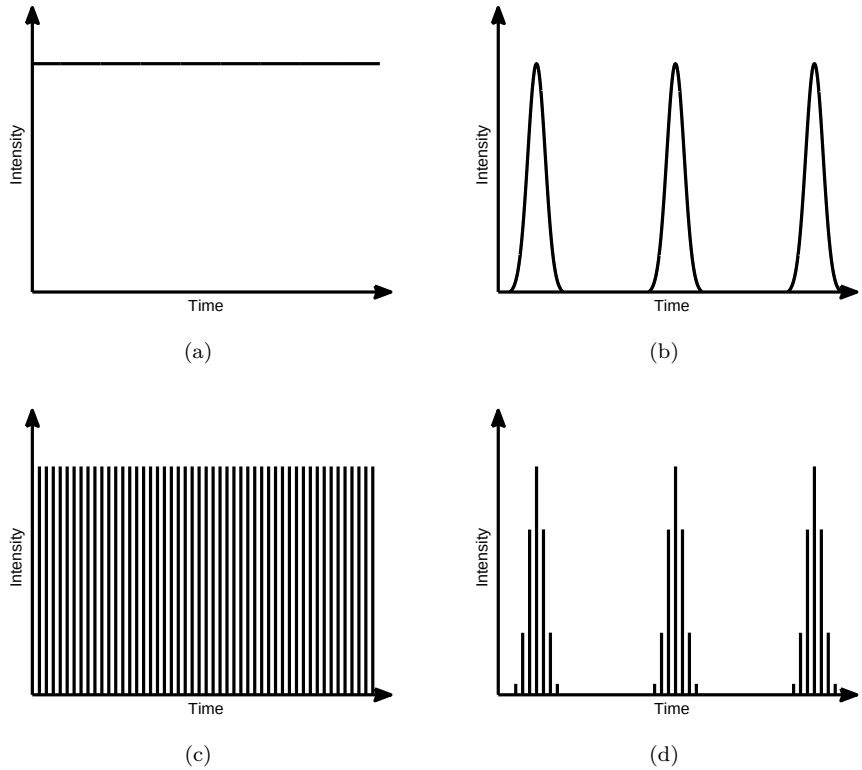

Figure 2.2: Transient regimes of a pulsed laser: (a) continuous wave (CW), (b) Q-switching (QS). Q-switching instabilities in mode-locked lasers lead to the behaviour as depicted in (d) instead of the usually desired CW mode-locking shown in (c).

Here, $E_{\mathrm{sat,A}}$ is the saturation energy of the absorber. It was also assumed that the first term on the right-hand side of Equation (2.11) is small compared to the second term, which is the case for pumping well above threshold, for which the second term becomes large, or for a small round-trip time (e.g. high repetition rate) compared to the upper laser-level life-time. Equation (2.12) provides guidelines when designing a saturable absorber and also points towards the challenges when aiming for specific laser parameters. Two main observations are of particular interest:

I High-repetition rate lasers will subsequently have relatively low pulse fluences and, thus, require small modulation depths as well as small saturation energies for the gain medium and the absorber.

II Both the absorber's saturation fluence, as well as the modulation depth, are ideally small, i.e. the absorber design aims for minimising both parameters.

The impact of these observations becomes clear when noting that an absorber's saturation fluence and modulation depth are not necessarily independent of each other. It has been shown, that their product is approximately constant when considering quantum-well based saturable absorbers [98] (see also Section 3.3).

An even simpler expression for the design rule given by Equation (2.12) can be obtained by defining the saturation parameters $S = E_{\mathrm{p}}/E_{\mathrm{sat}}$ for the gain medium and the absorber, respectively:

$$q_0 < S_{\mathrm{L}} \cdot S_{\mathrm{A}} \ . \tag{2.13}$$

If the upper-laser level life-time τ_{l} is not long, then an additional term $(S_{\mathrm{A}} T_{\mathrm{r}}/\tau_{\mathrm{l}})$ has to be added on the right-hand side. The general interpretation, however, is that the combined saturation of the gain and the loss has to exceed the modulation depth in order to avoid Q-switching. Gain saturation in solid-state lasers is usually low, which facilitates storing a large amount of energy in the gain medium and subsequently leads to Q-switching. Equation (2.13) can then be read as a requirement on the saturable absorber, that its modulation has to be small in order to suppress the large modulation that would lead to Q-switching. Driving the absorber in a regime where it is well saturated also helps, since the relative modulation depth then becomes smaller for a stronger saturation.

2.4 Mode-locking with a Kerr nonlinearity

The Kerr nonlinearity described above in the context of SPM is an important effect for mode-locking since it can lead to spectral broadening as opposed to the general spectral narrowing imposed by the bandwidth limits of the various laser components. However, the phase modulation not only has implications for a time-varying intensity, but also for a spatially varying intensity profile. While the temporal pulse profile leads to the time-dependent refractive index change as discussed above (see Equation (2.5)), the spatial intensity profile of the laser mode, at the same time, induces a spatial variation of the refractive index. Similarly to Equation (2.5) an analog formulation is found to be given by:

$$n(x, y) = n_0 + n_2 \cdot I(x, y) \ . \tag{2.14}$$

Here, x and y denote the coordinates transversely to the beam's direction of propagation. The result of a spatial variation in the refractive index (or equivalently, a spatially dependent phase) is the formation of a lens, the so-called *Kerr-lens*. This lensing effect leads to focusing (or defocusing, depending on the sign of n_2) of high-intensity signals such as ultra-short pulses. The variation in mode size, in combination with an aperture placed inside the cavity, can be used to create an intensity dependent loss. This effectively realises an artificial, fast saturable absorber according to Equation (2.7). This constitutes the mechanism behind *Kerr-lens mode-locking* (KLM) as mentioned in the beginning. A number of lasers were successfully mode-locked using this technique [28, 32, 58, 99, 100]. The most successful

gain medium is still Ti:Sapphire since it has a broad gain spectrum which supports few-femtosecond pulses and thus, very large peak intensities. Yb-doped gain media enjoy a similar success owing to a comparatively larger value of their nonlinear refractive index. However, the technique puts strong requirements on the cavity design, e.g. the intensity in the gain medium generally has to be large in order to exploit the usually low nonlinear refractive index. The drawback of an in general low third-order nonlinearity in common laser materials was already mentioned at the end of Section 2.1. The approach introduced in this thesis, namely de-coupling of the third-order nonlinearity (used for KLM) from the gain medium and, thus, acquiring a larger freedom of design, is described in detail in Chapter 7.

Chapter 3

Semiconductor Saturable Absorbers

The subject of the following chapter are quantum confined semiconductor materials for use as saturable absorbers. First, the history of semiconductor saturable absorbers is briefly presented. This overview is followed by a general description of quantum confinement in nano-structures after which quantum dots as a specific implementation of a confined system are discussed. The development of those quantum dots as saturable absorbers for mode-locking of lasers is portrayed. A similar overview for carbon nanotubes as saturable absorbers is deferred to Chapter 6 in order to provide a consistent transition to the following Chapter 4, in which specific quantum dot saturable absorbers are characterised in detail.

3.1 Overview

Mode-locking with a semiconductor saturable absorber was first demonstrated in a semiconductor laser diode [101] and later in a color centre laser [102]. The crucial issue at that point was to reduce the absorber's relaxation time so that the absorber would fully relax during a cavity round-trip. This has been achieved by proton bombardment which introduced additional recombination centres in the structure, thereby drastically reducing the recovery time [103]. Also, the growth temperature showed to have a pronounced effect on the carrier life-time and was henceforth used to control the relaxation behaviour [67]. With the advent of high-efficiency laser diodes for pumping of Nd- and Yb-doped gain media, diode-pumped solid-state lasers emerged as very efficient laser sources. Mode-locking these lasers with semiconductor absorbers, however, proved to be difficult, since the upper laser-level life-time was significantly longer than in previously used gain media. Also, the large gain saturation energy would not permit forming a suitable net-gain window, which was considered necessary according to mode-locking theory[1], while the

[1] Upon understanding of soliton mode-locking, it became clear, that the gain-window size is not necessarily the defining parameter.

semiconductor's saturation energy, in comparison, was too small.

A solution was to place the absorber inside an anti-resonant Fabry-Pérot cavity, thus artificially increasing the absorber's saturation energy by lowering the amplitude of the interacting electric field [35]. Still, Q-switching as a result of the long upper laser-level life-time remained a problem. Closer examination [62, 68, 69] concluded, that low modulation depth and, at the same time, low absorber saturation energy were desirable (see Section 2.3). A smaller spot-size on the absorber and in the gain medium would reduce saturation energies, but the laser mode size was typically limited by the cavity design. Using resonant absorber designs, it was possible to further lower the saturation fluence [104]. Nevertheless, it was pointed out, that a stronger field enhancement would also increase the modulation depth and thereby effectively couple the two parameters in an unfavourable way [98]. For the widely used quantum wells, changing neither saturation fluence nor modulation depth are directly affected by changing the well's thickness, since both parameters are in this case defined by the density of states, which has a peculiar dependence on the thickness. Different semiconductor materials were used to further tailor the absorption behaviour. However, this approach was ultimately limited by the need of low-loss absorbers, which implies good lattice matching, effectively reducing the freedom in the choice of material. Thus, it became apparent that different technologies were necessary to achieve mode-locking for a wider range of lasers, in particular lasers with low intra-cavity pulse fluence.

3.2 Quantum confinement

To realise saturable absorption, the absorption rate in the volume of the excited material has to decrease with increasing intensity, i.e. the material needs to ex-

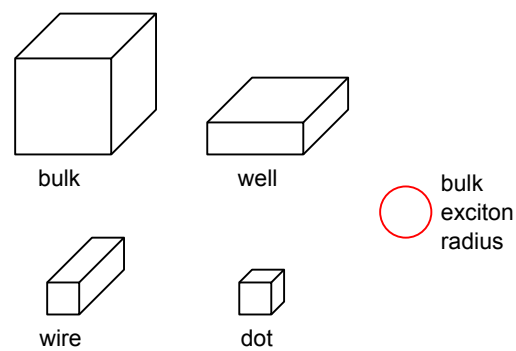

Figure 3.1: Visualisation of the condition for various kinds of quantum confinement: the physical width in at least one direction is smaller than the bulk exciton radius (red circle).

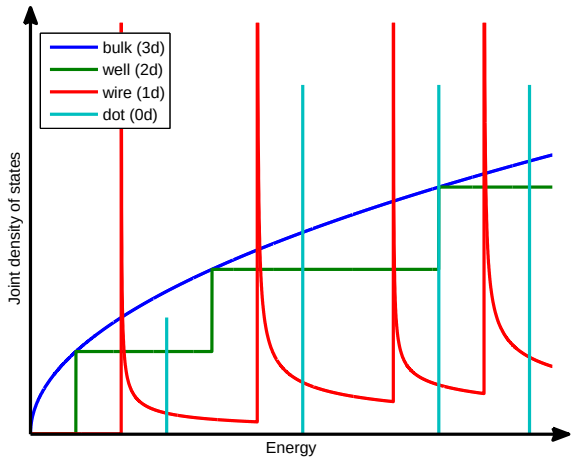

Figure 3.2: Joint density of states as a function of energy for bulk material (blue) and for quantum confined structures (well, green; wire, red; dot, cyan). The discrete nature of the energy levels in the case of quantum confinement is immediately visible. The different amplitude and shape of the peaks for the 1d and 0d cases reflects degeneracy.

hibit a nonlinear absorption behaviour. Classically, this has been achieved by using quantum dots (QDs, e.g. from PbS) and their discrete absorption spectrum in an otherwise transparent glass matrix. These doped glasses have successfully been employed as saturable absorbers for mode-locking [105–109]. The specific requirement for discretisation of a semiconductor's absorption spectrum is that its size should be smaller than or at least comparable to the exciton radius of the bulk material (see Figure 3.1 for a visualisation). Discretisation and, consequently, a drastic limitation of the total number of states are already achieved when confinement is provided in only one dimension, i.e. in a thin film, also called *quantum well* (QW). Subsequent confinement along additional dimensions leads to *quantum wires* (two-dimensional confinement) and to *quantum dots* (QDs, confinement in all three dimensions). The energy level structure and, correspondingly, the absorption spectrum change significantly with the number of dimensions which are subject to confinement. This is illustrated in Figure 3.2 showing the joint density of states (i.e. the total number of available states for a given transition energy) as a function of energy for the different types of confined structures. Starting from the square-root relation in a bulk semiconductor, the shape of the spectrum changes towards

an atom-like spectrum as exhibited by QDs[2]. The reduced number of states also leads to a larger overlap of the electron and hole wavefunctions, which, in turn, increases the oscillator strength for individual transitions. This directly affects the saturation behaviour [110]. A QD transition will thus show stronger absorption and, consequently, lower saturation energy than a quantum wire or well.

It also has to be noted, that Figure 3.2 shows the spectra for an individual well/wire/dot, respectively. In practice, the sharp spectral lines shown especially by wires and dots will broaden as a result of a variation in size among an ensemble of nano-structures (see, e.g. the transmission spectrum shown in Figure 6.3a for carbon nanotubes (CNTs) in Chapter 6). In fact, this (inhomogeneous) broadening turns out to be beneficial, because it increases the overall bandwidth of the device. Since the exact position of the transitions is directly related to the size of the nano-structure, the absorption spectrum can be tailored according to application needs.

The confined structures investigated in this thesis are of the 1d- and 0d-type, namely CNTs (wires) and self-assembled semiconductor QDs (dots). A stronger focus is put on the self-assembled QDs (Chapters 4 and 5), which here have a pyramidal shape as a result of the peculiar fabrication method as will be mentioned in Section 3.4 below [111]. The CNTs used for mode-locking as presented in Chapter 6 constitute quantum wires, since their tube-like shape results in quantum confinement in two dimensions. Although they are not made from a classical semiconductor material but entirely from elemental carbon, these nanotubes show semiconductor-like behaviour, depending on the peculiar pattern of the tube's mantle, as will also be further elaborated on in Section 6.2.

3.3 Quantum-dot saturable absorbers

QDs in general have been studied for a wide range of different applications, including modulation of lasers by using them as saturable absorbers. An early demonstration used a filter glass containing semiconductor QDs (typically other materials than III-V semiconductors) as saturable absorber to mode-lock various lasers, as was already mentioned above.

A growing semiconductor industry and increasing knowledge in fabrication technology facilitated the fabrication of high-quality semiconductor structures. Together with the discovery of self-assembled QDs, as a result from the large lattice mismatch during growth by molecular beam epitaxy, this led to extensive research efforts concerning QDs made from III-V semiconductor materials. Embedding those QDs into semiconductor hetero-structures promised further miniaturisation of lasers. In particular, the GaAs/AlAs semiconductor system is of interest, since the small lattice mismatch allows growth of low-loss Bragg reflectors for the NIR

[2]A main difference between an atom and a QD is that the atom's discrete spectrum is the result of the Coulomb potential, while in the case of the QDs, the potential well is defined by the extent of the cluster.

region, onto which QDs from InGaAs can easily be grown. This technology is extensively used to develop laser diodes and saturable absorbers as well as combined structures, integrating the gain medium and the absorber into a single chip. Early implementations of integrated devices are presented in [41, 112]. Semiconductor lasers have since been a driving force in the development of semiconductor-based absorbers. First demonstrations of all-semiconductor, quantum-dot saturable absorbers for mode-locking of bulk-material lasers are given in [71, 113, 114]. In Publication III, such an absorber was used for mode-locking of a high-repetition rate, bulk-material laser, thus showing that QDSAs indeed meet the requirements for this demanding application.

In general, QDs fulfil the performance needs required for mode-locking of low-gain, low-energy semiconductor lasers and also for any other low-energy laser systems. However, a more significant advantage becomes apparent when noting that the absorption characteristics of QDs can be tuned by changing the size of the dots and their density, while the absorption properties of quantum wells are primarily tuned by the choice of the semiconductor material. By using QDs, it is thus possible to fabricate semiconductor structures for a wide range of applications by employing the same technology. This is demonstrated in Chapter 5, presenting results from mode-locking different lasers using the same QDSA technology.

A widely used technique for fabrication of QDs is the so-called *Stranski-Krastanow growth*[3] of self-assembled QDs using molecular beam epitaxy (MBE). A typical material combination is InAs or InGaAs as dot material on a GaAs surface. The first one to two monolayers is deposited as a film (wetting layer, WL) without strain relaxation. Upon further growth, islands of In(Ga)As start to form and the strain from the lattice mismatch is gradually relaxed [116]. The islands' exact shape depends on the growth conditions [117–119]. A typical shape configuration, which is also attributed to the QDs in this thesis, is that of a pyramid with a square base. Nevertheless, their electronic states can be described with good accuracy[4], if a spherical shape is assumed [120]. Further deposition increases the size of the dots, but will neither affect their shape nor the dot density on the substrate. The density can instead be controlled by the growth rate, i.e. the number of monolayers deposited as a function of time [40]. If the growth continues further, the dot growth ceases in favour of a uniform, relaxed film [121].

3.4 Basic properties of semiconductor quantum dots

The main properties of QDs follow from the quantisation of the energy states as a result of quantum confinement, which is directly related to the size of the dots. As mentioned above, confinement refers to one or more spatial dimensions being smaller than the bulk exciton radius inside the material in question. The exciton

[3]The defining mechanism, namely the formation of nano-crystallites on a surface, has been described by Stranski and Krastanow in [115].

[4]The approximation is not as good for the hole states as it is for the electrons.

radius in bulk material can be calculated from the material's relative dielectric constant ε_r and the free-electron mass m_0 relative to the reduced mass[5] m_r of the electron-hole system:

$$r_\mathrm{X} = \frac{m_0}{m_\mathrm{r}} \varepsilon_\mathrm{r} \cdot a_\mathrm{B} \ . \tag{3.1}$$

The exciton radius is usually considerably larger than the Bohr radius a_B. Typical values are, e.g. 11 nm for intrinsic GaAs and 37 nm for InAs [122]. Considering that the lattice constant for these materials is less than 1 nm, it is evident, that confinement can be obtained in a conglomerate of atoms which still exhibits bulk properties in the sense that the atoms are organised in a regular lattice. This assumption is used when deriving the principal properties of confined semiconductor structures.

The density of states is obtained from an examination of the discretised k-vectors in a structure of finite dimensions. The principal result has already been shown in Figure 3.2 above. In the extreme case of confinement in all three dimensions (QD), the density of states as a function of energy resembles an atom-like spectrum. Finding the energy levels is achieved by solving the problem in the form of a Hamiltonian comprising the kinetic contributions from both the electron and the hole as well as a confinement potential V_conf and a Coulomb potential V_Coulomb:

$$H = -\frac{\hbar^2}{2m_e}\Delta_e - \frac{\hbar^2}{2m_h}\Delta_h + V_\mathrm{conf} + V_\mathrm{Coulomb} \ . \tag{3.2}$$

Here, Δ_e and Δ_h are the Laplace operators for the electron and hole, respectively. This equation represents a general description and is the starting point for the examination of any excitonic system. Stronger confinement in any direction reduces the influence of the Coulomb term as compared to the confinement term in that direction. The degree of confinement is quantified by comparing any of the nanostructure's three extents $L_{x,y,z}$ with regard to the bulk material's exciton Bohr radius. The case of $L_{x,y,z} < 2r_\mathrm{X}$ is referred to as *strong* confinement. In this situation, the Coulomb interaction between an exciton's electron and hole is negligible in the respective dimension and the confinement potential defines the energy spectrum. The energy spectrum in the direction of a non-confined dimension then corresponds to that of a freely moving particle.

Transition energies

For a spherical QD, the problem bears similarity to the case of a hydrogen atom and the same approach is used to find a solution. However, the hydrogen's Coulomb potential is exchanged by a constant potential with a finite extension in all three dimensions. For an infinitely deep potential with radius R, the absorption lines E_{nl}

[5] The reduced mass is defined by the electron mass m_e and the hole mass m_h in the following way: $\frac{1}{m_\mathrm{r}} = \frac{1}{m_e} + \frac{1}{m_h}$

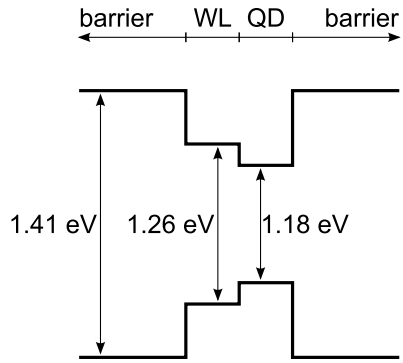

Figure 3.3: Energy diagram of self-assembled InGaAs QDs grown on the initial InGaAs wetting layer (WL) and surrounded by GaAs as a barrier material. The indicated energies denote the gaps between the ground states of electrons and holes in the respective region as determined from photoluminescence measurements (see Section 4.5 in Chapter 4).

are defined by the various zeros (numbered by n) of the spherical Bessel functions B_l:

$$E_{nl} = E_{\mathrm{gap}} + \frac{\hbar^2}{2m_{\mathrm{r}}} \left(\frac{B_{nl}}{R} \right)^2 . \tag{3.3}$$

As noted above, the reduced mass of the electron-hole pair is here denoted as m_{r}. In analogy to atoms, the indices n and l resemble the principal and orbital quantum number, respectively. When including the remaining Coulomb contribution, the energies according to Equation (3.3) are corrected downwards. However, the smallest energy is always larger than that of the bandgap E_{gap} of the bulk material. For an increasing dot size, the minimum transition energy approaches the bulk material's bandgap energy. Solving the Hamiltonian (3.2) for a finite potential leads to a transcendent equation for the energy levels of the system (see, e.g. [123] for details). One important observation from this approach is that a minimum potential is necessary for the existence of at least one energy level. This is distinctly different from the case of a QW, which can be made arbitrarily shallow while still containing at least one discrete state. In fact, in many cases, only one or a very few states exist[6] when considering typical QD dimensions of $\approx 10\,\mathrm{nm}$ and potential differences on the order of 100 meV [120, 124].

An energy diagram for InGaAs QDs grown on GaAs according to the procedure mentioned in Section 3.3 is shown in Figure 3.3. The numbers are chosen to resemble the specific materials used for the experiments presented in this thesis. The InGaAs

[6] While the number of electronic states is very small, the number of hole-states is larger, due to the larger effective mass.

was grown with a nominal thickness of 1.2 nm, i.e. about 2 monolayers, which is just above the critical thickness of ca. 1.7 monolayers at which dot growth starts. The gaps of the WL and the QD regions were determined by photoluminescence (PL) spectroscopy (see Section 4.5). Using the given QD transition energy in Equation (3.3) and assuming a reduced mass[7] of $0.023 \cdot m_0$, the diameter of the QDs can roughly be estimated as being $\approx 13\,\text{nm}$. This value has to be considered a very crude approximation since the value for the reduced mass m_r varies widely across the literature. A more detailed approach for the calculation of the energy levels in these types of QDs can be found in, e.g. [126]. Nevertheless, the obtained values are similar and give an impression of the nano-clusters' size in comparison to the size of an individual atom ($\approx 0.1\,\text{nm}$) and the corresponding lattice constant ($\approx 0.6\,\text{nm}$). Furthermore, the general observation that the lattice constant in this case is three orders of magnitude smaller than that of the bulk exciton radius emphasises the potential for tuning the values of the energy levels. Especially, since the shift in energy due to quantum confinement depends on the inverse radius squared (see Equation (3.3)). As a result, the transition energies can be varied by several 100 meV, corresponding to a change in wavelength of 100 nm or more [127]. An impressive example is the variety of absorption spectra of colloidal QDs made from CdSe, spanning the whole visible spectral range [128]. A crucial parameter, however, is the bulk material's bandgap E_gap, which eventually determines the accessible wavelength range. For mode-locking of lasers in the NIR region, the system of InGaAs is a very suitable candidate. Wide emission and absorption spectra can be accessed by varying the In/Ga ratio, theoretically starting from the bulk GaAs bandgap of 1.424 eV, corresponding to a wavelength of 870 nm, and into the mid-infrared region.

Relaxation

The relaxation dynamics in semiconductors can be rather complex, but often a two-step process is sufficient to describe the essential features. Following excitation, fast thermalisation leads to the accumulation of carriers at the band edges. This mechanism is also referred to as intra-band relaxation, since the carriers relax inside the band to which they were excited. Relaxation occurs via phonon scattering or electron-electron scattering and can be very fast, usually on a sub-picosecond timescale. Recombination, the second step, takes place on a longer time-scale, which can range from a few picoseconds to several nanoseconds. In confined structures, the fast thermalisation is affected by the reduced number of sub-levels inside a specific band. Nevertheless, ultra-fast thermalisation is the mechanism that facilitates fast relaxation times for mode-locking of lasers in QWs [36]. Indeed, in quantum wells as well as in quantum wires, the phonon-assisted thermalisation is the main contributor to ultra-fast recovery in excited semiconductors [129]. In the extreme

[7] Since no value for the given composition was available, the effective mass in pure InAs was used as an approximation [120, 124, 125].

case of QDs, however, the role of phonon scattering is drastically reduced by the complete discretisation of the energy level structure. Efficient phonon-scattering is not possible due to the large spacing between subsequent levels. Despite the expected phonon bottleneck effect, ultra-fast dynamics on the order of picoseconds or even sub-picoseconds have been observed [130, 131]. Auger processes have been pointed out to have a profound influence on the relaxation dynamics at strong intensities. This is due to the interaction with an electron-hole plasma, that is being formed in the higher-lying, quasi-continuum states of the QDs [129, 132]. More recently, a similar interaction with the well-like energy-level structure of the WL (adjacent to the QDs, see Figure 3.3) has been considered to facilitate fast thermalisation [131, 133, 134]. Another influence to consider is the mediation of relaxation by structural defects in the vicinity of a QD [135, 136]. The lattice mismatch of InAs grown on GaAs has been shown to create traps inside the region where the QDs are located [137] (the growth of the InAs WL is sufficient, i.e. the QDs are not necessary to create the traps). With these observations in mind, the apparent phonon bottleneck can be circumvented and the observed sub-picosecond relaxation times in QDs can be explained.

Chapter 4

Characteristics of Quantum-Dot Saturable Absorbers

This chapter describes the characterisation of quantum-dot saturable absorbers with respect to the parameters relevant for the mode-locking of lasers. Further given is an overview of these parameters and the general model that is used to describe an absorber's response. In addition, the experimental techniques for characterisation of quantum-dot saturable absorbers are presented and applied to examine a set of samples in order to draw conclusions on the connection between the design parameters and the absorber properties.

First, the examined structures are presented in detail. The multi-layered design gives rise to dispersion, which is characterised using a white-light interferometer. Following that, the absorbers' reflectivity as a function of incident pulse fluence (nonlinear reflectivity) is measured. Finally, the transient response is examined on a short-time scale by a pump-probe experiment and, on a long-time scale, by time-resolved photoluminescence spectroscopy. A summary of the main findings from all characterisation experiments is given at the end of the chapter.

4.1 Structure design

Since the first demonstration of semiconductor saturable absorbers (SSAs), their structural design has seen extensive development and numerous variations have been proposed. However, before considering the detailed design, some key questions have to be addressed. First: is the absorber integrated into a super-structure or is it a stand-alone device? Second: is the absorber operated in transmission or reflection? Third: does the absorber behave resonant or anti-resonant?

The first point addresses the context in which the absorber will be used. In the field of semiconductor lasers, the integration of a gain medium and an absorber has been very successful leading to very compact and simple devices [41, 112]. For

other gain media, the absorber is in turn designed as a separate cavity element. The present thesis focuses on bulk-material solid-state lasers, hence the absorber will be a separate cavity element.

The exact position in the cavity, then, presents an answer to the second question. Although many absorbers have been and are still used preferably in transmission (dyes, carbon nanotubes), semiconductor absorbers are usually operated in reflection, which avoids the removal of the substrate but, instead, requires an underlying, high-reflective multi-layer structure. This part can also be designed partially transmissive, thus offering to integrate the outcoupling into the absorber [138]. This approach has not been used extensively, since it fixes the cavity's linear loss and, thus, decreases the freedom of design for further optimisation. However, this alternative might be considered for compact lasers and if no further design change is necessary. The work conducted for this thesis focuses on high-reflective designs intended for use as cavity end-mirrors.

The third point, then, already relates to tailoring the electric-field distribution inside the structure. The interference of the incident and the reflected electric field creates a standing wave pattern. The absorbing regions are usually placed precisely at or close to the anti-nodes of this pattern in order to expose them to a maximum intensity. The interaction between the absorbing regions and this standing wave in the structure then determines the overall behaviour of the absorber and, thus, tailoring the electric field strength is a crucial design step. The degree of interaction or equivalently, the coupling of the input electric field to the electric field inside the structure, is quantified by the enhancement factor ξ, which is defined as the maximum of the squared, normalised electric-field distribution $\mathcal{E}_{\mathrm{n}}(z)$ inside the structure. This defines the intensity distribution $I(z)$, which also depends on the refractive index profile $n(z)$ and the incident intensity I_{in} [98]:

$$I(z) = I_{\mathrm{in}} n(z) \left|\mathcal{E}_{\mathrm{n}}(z)\right|^2 \ . \tag{4.1}$$

Since the normalised, incident electric field's amplitude is set to 1, the sum of the input and the output electric field then has a maximum amplitude of 2 (the interference is constructive since the electric field corresponds to a longitudinal mode of the laser cavity) and, thus, the maximum of $\left|\mathcal{E}_{\mathrm{n}}(z)\right|^2$ outside the structure is equal to 4. In this thesis, structures with $\xi < 1$ will be considered as anti-resonant, while structures with $\xi > 1$ will be referred to as resonant (see also Section 4.2).

The general structure of the SSAs examined in this thesis consists of two regions as depicted in Figure 4.1:

I A Gires-Tournois cavity, with an impedance matching front-section and containing a number of QD-layers.

II A high-reflective Bragg-stack, to enable use as a cavity end-mirror.

The Bragg-stack is made from several layers with alternating refractive index to achieve a high reflectivity for the desired wavelength region; in this case, between

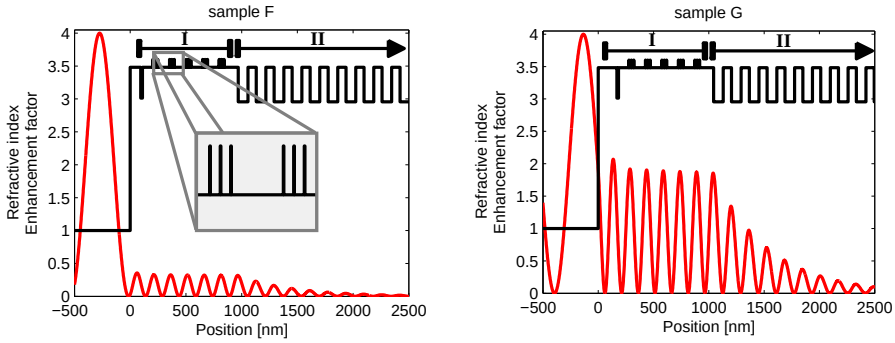

Figure 4.1: Refractive index profile (black) and standing wave pattern (red) for (a) the anti-resonant sample F and (b) the resonant sample G. The different functional sections as described in Section 4.2 are labeled with the corresponding Roman numerals. The two structures only differ in the thickness of the cap layer in front of each structure. I: Gires-Tournois cavity with QD-layers; II: Bragg-stack. The inset in (a) shows a magnification of the first two QD groups.

1.0–1.1 µm. In the NIR region, the combination of GaAs and AlAs offers an index difference of 0.56 while avoiding defects from a lattice mismatch due to the fact that the two materials exhibit nearly the same lattice constant (0.565 nm and 0.566 nm, respectively). For the mentioned target region, the thickness of an individual layer from the Bragg-stack is on the order of 70–90 nm (i.e. $\lambda/4$, see also Appendix A.2).

Differences between resonant and anti-resonant structures

While the power reflectivity of a structure as described above is more or less independent of whether its design is resonant or anti-resonant (at least for small nonlinear losses and with weak two-photon absorption), the phase change imprinted on the field and, hence, the dispersion characteristic is substantially different. In resonant structures, a phase change occurs around the design wavelength, while the phase is comparatively flat in the case of an anti-resonant structure. This has direct consequences for mode-locked laser design, since, on the one hand, unwanted dispersion has to be compensated for, but, on the other hand, this design feature can be used to compensate for already existing dispersion, e.g. from the gain medium. A detailed discussion of the actual samples can be found in Section 4.3 below.

The stronger wavelength dependence also applies to the enhancement factor ξ, which varies stronger in the case of resonant structures. The resonance condition is only given close to the design wavelength. The enhancement factor will conse-

quently be small if the structure is operated off from the resonance. This makes resonant designs less versatile in terms of bandwidth and the laser medium employed. More important though is the fact that growth errors will have a more pronounced effect for the resonant structures, since the resonance might shift away from the desired wavelength, thereby seriously compromising the intended performance. Nevertheless, resonant structures present a simple solution for the fabrication of absorbers based on bulk or quantum-well semiconductors with low saturation fluence [104]. Accordingly, an anti-resonant design might be chosen for high-power applications to avoid damaging the device [139].

4.2 Sample description

The absorbers under examination in this thesis are all based on self-assembled InGaAs quantum dots and with GaAs as a barrier material. The complete absorber structure consists of several sections, as mentioned above (compare with the example structure given in Figure 4.1b): An interface (GaAs and AlGaAs), several layers containing self-organised InGaAs QDs packed in groups, which are separated by GaAs spacer layers, and a high-reflective Bragg-stack made of AlAs/GaAs pairs. The principal fabrication of an individual QD layer and the Bragg-stack at the end of the device was kept the same but for one sample (sample H, see Table 4.1). Self-assembled QDs were grown by deposition of InGaAs layers with a nominal thickness of 1.2 nm, except for sample H, for which it was 2 nm. The interface at the front-end of the device and the number of the QD layers as well as the spacing between the layers were varied. The QD layers were organised in stacks of 3 or 5 individual layers per group and the groups were separated by bulk GaAs so that each group was located at an anti-node of the standing wave pattern inside the structure. The QD density of each individual QD layer was on the order of $3 \cdot 10^9\,\mathrm{cm}^{-2}$ to $5 \cdot 10^9\,\mathrm{cm}^{-2}$.

The interface of the structure was designed to create either a low field distribution inside the structure or to enhance the electric field (see also Section 4.1). For controlling the resonance condition, the cap layer's thickness was modified by a value of $\lambda/4$, where λ is the design wavelength. Figure 4.1 shows the calculated field distribution in two structures (F and G), the only difference being the thickness of the cap layer. In general, a more sophisticated numerical approach can be used for the cap-layer design. This was done for sample B, to create a compromise between resonant and anti-resonant design. The design parameters for the samples examined in this chapter are presented in Table 4.1. The design and the simulated electric-field distribution of all samples are provided in Appendix B.1.

Name	Groups	Sub-layers	Spacing	Rel. field	Comment
A	6	3	10 nm	1.59	Resonant
B	6	3	10 nm	1.97	Special AR coating
C	3	3	10 nm	2.35	Resonant
D	10	3	20 nm	0.30	Anti-resonant
E	10	3	20 nm	0.96	Resonant
F	5	3	20 nm	0.31	Anti-resonant
G	5	3	20 nm	1.78	Resonant
H	3	5	20 nm	0.58	Anti-resonant

Table 4.1: Structure design details of the QDSAs. Each group contains a number of individual sub-layers. The total number of QD layers then is the product of columns two and three. The field enhancement factor ξ (rel. field) was calculated for the wavelength of the characterisation laser used in the experiments presented in this chapter, i.e. at the wavelength of 1042 nm.

4.3 Dispersion

Any optical component that is based on a layered design in order to exploit interference effects, will show a certain dispersion, in particular the SSAs considered here. For this thesis, the dispersion characteristics of all of the absorber samples have been measured with a white-light interferometer. A typical example is shown in Figure 4.2. The measurements for all of the samples are presented in Appendix B.3. In general, it was observed that resonant designs show a strong modulation of the group delay dispersion (GDD) around the design wavelength, while the anti-resonant designs lead to smaller values of the GDD and, thus, less

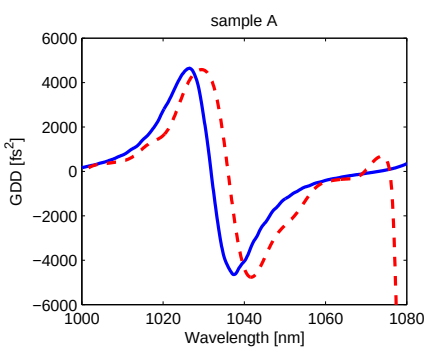

Figure 4.2: Calculated (blue, solid line) and measured (red, dashed line) group delay dispersion of sample A.

wavelength dependence. The general shape is well reproduced by the measurement and also the value of the measured and calculated GDD are in good agreement. Any remaining differences point towards either growth errors or wrong assumptions in the simulation. With respect to the latter, it has to be noted, that the QD layers were assumed to be thin films with a thickness of the nominal deposition thickness, which is most likely not reflecting the real situation inside the structure due to the formation of the QDs.

4.4 Nonlinear reflectivity

The nonlinear reflectivity describes an absorber's saturation behaviour which is crucial for mode-locking of lasers. This behaviour defines the variable loss ℓ in the master equation (2.1). For mode-locking, the characteristic role of the variable loss is to saturate for high-intensity pulses, so that the net gain is larger than for low intensity signals, such as noise or CW signals. This usually corresponds to the saturation of a transition at the lasing wavelength in the absorber. The starting point for a general model is thus a rate equation for the population difference ΔN in a two-level system; the equation being of the same form as the differential equation (2.10), describing the evolution of the loss [51].

General model

In practice, as well as in this thesis, saturable absorbers are often semiconductors used in reflection and Equation (2.9) can be reformulated by expressing the absorber's behaviour via experimentally accessible parameters. Instead of providing the loss as a function of pulse energy, the reflectivity of the device is given as a function of the incident pulse fluence F_p[140], namely:

$$R(F_\mathrm{p}) = R_\mathrm{ns} - \left(1 - \exp\left[-\frac{F_\mathrm{p}}{F_\mathrm{sat}}\right]\right)\frac{F_\mathrm{sat}}{F_\mathrm{p}}\Delta R - \frac{F_\mathrm{p}}{F_2}\ . \tag{4.2}$$

The original exponential term is still included. However, any non-saturable losses (e.g. scattering loss) have been taken into account by including the non-saturable reflectivity R_ns, i.e. the maximum reflectivity, from which the non-saturable loss follows as $\Delta R_\mathrm{ns} = 1 - R_\mathrm{ns}$. Also, an additional loss term F_p/F_2 takes into account two-photon absorption in the material. The characteristic parameters F_sat, ΔR, and F_2 are explained in more detailed in the following subsections. After measuring the reflectivity as a function of the excitation fluence, Equation (4.2) can readily be fitted to the data obtained from the corresponding reflectivity measurements to yield the characteristic parameters of a specific saturable absorber. An example is shown in Figure 4.3.

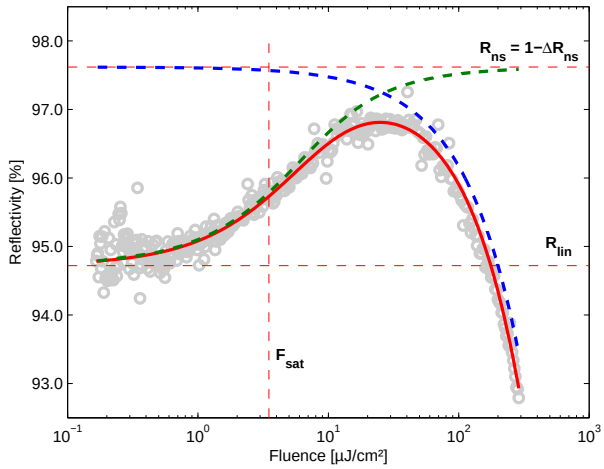

Figure 4.3: Example of a nonlinear reflectivity measurement with various fits. The measured data points (grey circles) are used to find a fit (red, solid) according to the model function given by Equation (4.2). Linear and non-saturable reflectivity are indicated by the dashed, red, horizontal lines, the saturation fluence is marked by a dashed, red vertical line. Also plotted are the individual contributions from saturable absorption (dashed, green) and two-photon absorption (dashed, blue).

Saturation fluence

Solving the differential equation (2.10) with the assumption of a relatively long relaxation time yields a characteristic parameter, the saturation fluence F_{sat}, that defines the strength of the response for a given input:

$$F_{\mathrm{sat}} = \frac{\hbar\omega}{2\sigma} \ . \tag{4.3}$$

Here, σ denotes the cross section and ω the frequency of the incident electric field. With this definition, the nonlinear absorption coefficient α is then given by the following expression [140]:

$$\alpha(F_{\mathrm{p}}) = \alpha_0 \exp\left[-\frac{F_{\mathrm{p}}}{F_{\mathrm{sat}}}\right] \ . \tag{4.4}$$

In the literature, the degree of saturation is often expressed by the saturation parameter $S \equiv F_{\mathrm{p}}/F_{\mathrm{sat}}$, i.e. the incident pulse fluence relative to the saturation fluence.

Modulation depth

The achievable change in reflectivity is expressed by the modulation depth ΔR, which is equal to the difference between the maximum reflectivity R_{ns} and the linear reflectivity R_{lin} at low excitation. It is connected to the absorber's modulation q_0 by the expression:

$$\Delta R = 1 - \exp(-q_0) \ . \tag{4.5}$$

Since the modulation depth in bulk solid-state lasers is typically less than a few percent, or, possibly, even below one percent, the above equation is well approximated by the linearised expression $\Delta R \approx q_0$ (this approximation is also included in Equation (4.2)).

Two-photon absorption

For high-intensity excitation, two-photon absorption (TPA) introduces a non-negligible loss. Although an absorber generally saturates for increased pulse fluence, saturation is per definition limited and the additional absorption loss by TPA will eventually dominate the response. The strength of the effect depends on the material's TPA coefficient β_{TPA} and also on the peak intensity of the excitation pulse, which, for a given excitation fluence, is directly related to the pulse width τ_{p}. These effects are usually summed up in a phenomenological parameter F_2 to describe the influence of TPA [140], namely:

$$F_2 \propto \frac{\tau_{\mathrm{p}}}{\beta_{\mathrm{TPA}}} \ . \tag{4.6}$$

Limitations

Although Equation (4.2) assumes a two-level system and neglects certain carrier dynamics in the semiconductor[1], it is a well-established model for describing an SSA's nonlinear response. It also makes different devices comparable in terms of their characteristic parameters. The two-level approximation is actually more justified in zero-dimensional QDs with their discrete energy levels as compared to QWs that have been used in the first place. Neglecting the carrier dynamics is at least justified as long as the intraband relaxation is fast and the trapping and recombination are slow compared to the laser pulse-length. For a detailed derivation and description of Equation (4.2) and its limitations see, e.g. [68, 141–143].

Nonlinear reflectivity characterisation setup

The basic method for measuring the nonlinear reflectivity of an absorber is by comparing the reflected pulse energy with the corresponding incident pulse energy. Although this approach is quite simple in theory, practical limitations arise from

[1] Intraband relaxation, recombination and trapping are explicitly mentioned in [140].

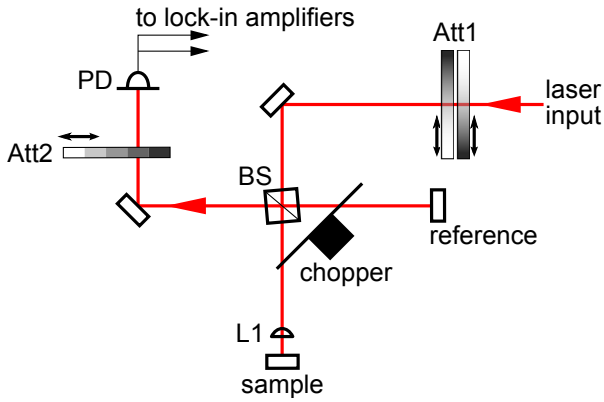

Figure 4.4: Schematic of the setup for measuring an absorber's nonlinear reflectivity at the *sample* position versus a *reference*. The input laser is attenuated by the gradient attenuator pair *Att1*. The Michelson interferometer contains a beam-splitter (BS) and a *chopper*. The sample beam is focused onto the absorber by an additional lens L1. The interferometer output is directed towards a photo-diode (PD). To avoid saturation of the photo-diode, an additional step-attenuator *Att2* is used. The measured signal is directed to two lock-in amplifiers. The reference frequencies are the inner and outer chopping frequencies of the chopper wheel.

various sources of noise, e.g. the used laser source, the photo-detector, and the attached electronic equipment. The change that has to be measured, can be very small, i.e. on the order of 0.1 % (absorbers with a large modulation depth, e.g. for mode-locking of fibre lasers, are significantly easier to characterise). A lock-in scheme based on a modulated input and with detection of the input and the output power using two photo-diodes has been demonstrated in [140]. An alternative setup using a chopper inside a Michelson-type interferometer and with only one photo-diode was presented in [144] and provided better accuracy. In this thesis, a third method with elements of both these approaches was used and was found to provide good accuracy and resolution for measuring modulation depths and non-saturable losses on the order of 0.1 % at fluences spanning an interval of four orders of magnitude.

A schematic of the setup is depicted in Figure 4.4. The excitation pulses pass a nonlinear density filter for attenuation (Att1) and are then launched into a Michelson-type interferometer. One arm contains a high-reflective mirror with a linear response as reference, the other arm focuses the beam onto the sample under examination. Both arms are chopped by the same chopper wheel but at two non-commensurate frequencies, as provided by the wheel's inner and outer sections. The output of the interferometer is imaged onto a photo-diode (PD). The resulting photo-voltage is processed by two lock-in amplifiers which extract the two signals

encoded by the two modulation frequencies. This approach has the advantage of using the same photo-diode to measure the reflected as well as the reference signal. An additional attenuator (Att2) is placed in front of the photo-diode and ensures that the operation remains inside the diode's range of linear response when varying the excitation energy. A high accuracy is provided by the use of the lock-in amplifiers. The ratio of the measured signals yields directly the nonlinear reflectivity.

The setup was calibrated with a high-reflective, linear mirror at the sample position in order to accommodate for any systematic errors, nonlinearities, and background signals. Correct positioning of the sample was achieved by focusing the interferometer's output onto a CCD camera and aligning the sample to match the spots from the two interferometer arms. Moving the sample out of focus also provides the possibility to examine the samples surface and select a clear and undamaged area.

While the modulation depth and the linear reflectivity can be measured with high accuracy, the saturation fluence is subject to a potentially large error. Since the excitation fluence on the sample is proportional to the beam waist squared, any error of this value has a strong influence on the resulting value for the saturation fluence. Careful measurement of the beam waist and diligent positioning of the sample are therefor of utmost importance.

Experimental results

The samples specified earlier in Table 4.1 were characterised with respect to the parameters describing the nonlinear reflectivity as mentioned in the preceding section, namely: modulation depth, non-saturable loss, and saturation fluence. The nonlinear reflectivity was measured as a function of incident fluence. The model function, as given by Equation (4.2), was fitted to the data to find the characteristic parameters for each sample. An example of a data set and its fit have already been presented above in Figure 4.3. The corresponding graphs for the other samples are provided in Appendix B.4. The results from the fitting are summarised in Table 4.2. The 95 % confidence intervals for the fitted modulation depth and non-saturable loss are on the order of 0.05 %. Fitting of the saturation fluence was found to be more robust for the resonant samples, where the roll-over caused by TPA is stronger. The 95 % confidence interval is about 10 % of the saturation fluence for resonant samples and on the order of the saturation fluence itself for anti-resonant samples. It has to be noted though, that the uncertainty stemming from imprecise knowledge of the spot size can easily be larger, as discussed above. Also, the confidence interval does not provide a measure for the actual error in the modulation depth and the non-saturable loss. However, these represent systematic errors that equally apply to all samples, i.e. the measured parameters are still comparable to each other inside the examined set of samples. Similarly, the values of the TPA parameter F_2 should be looked at with caution in case of the anti-resonant samples.

Name	# of QD layers	Rel. field	ΔR [%]	ΔR_{ns} [%]	F_{sat} [µJ/cm^2]	F_2 [µJ/cm^2]
A	18	1.59	2.90	1.38	3.5	$6.2 \cdot 10^3$
B	18	1.97	0.41	0.42	6.0	$9.9 \cdot 10^4$
C	9	2.35	2.79	1.06	3.1	$7.2 \cdot 10^3$
D	30	0.30	0.35	0.82	7.1	$3.3 \cdot 10^5$
E	30	0.96	1.19	1.06	3.8	$5.3 \cdot 10^3$
F	15	0.31	0.18	0.61	5.9	$1.9 \cdot 10^7$
G	15	1.78	1.08	0.63	3.8	$7.8 \cdot 10^3$
H	15	0.58	0.42	2.06	4.1	$4.5 \cdot 10^4$

Table 4.2: Results from fitting the model function (4.2) to the data acquired by the experiment described in Section 4.4. Fitted parameters: modulation depth ΔR, non-saturable loss ΔR_{ns}, saturation fluence F_{sat} and two-photon absorption parameter F_2.

Conclusions

In general, the saturation fluences are rather low and comparable to the low saturation fluence of quantum well absorbers as, e.g. presented in [104]. However, with the samples presented here, low saturation fluence can also be achieved with anti-resonant designs. Moreover, the saturation fluence appears to be essentially independent from the number of QD layers. The modulation depth, on the other hand, is controlled by the number of QD layers together with the field enhancement in the structure, i.e. whether a resonant or an anti-resonant design has been chosen. In the case of the anti-resonant samples, it may be noted that doubling the number of layers also doubles the modulation depth. The larger modulation depth of the anti-resonant sample H, which has a similar number of QD layers as sample F, is explained by the larger field enhancement factor. In the resonant structures, the modulation depth increases proportionally to the field enhancement factor, which becomes quite sensitive to the variation of the excitation wavelength. As opposed to this, the saturation fluence in QDSAs is substantially less dependent on the structure's specific design and the number of QD layers.

The dependence of the modulation depth and the saturation fluence on the design parameters is visualised in Figure 4.5. Both parameters are plotted versus the product of the number of QD layers and the enhancement factor, here called *figure of design* (FOD). It can be observed that a small figure leads to a small modulation depth, while the correlation with the saturation fluence appears to be weaker. Nevertheless, it should be noted that the enhancement factor included in the FOD is a theoretical value obtained from simulations based on the intended design.

The non-saturable loss is only slightly affected by the number of QD layers,

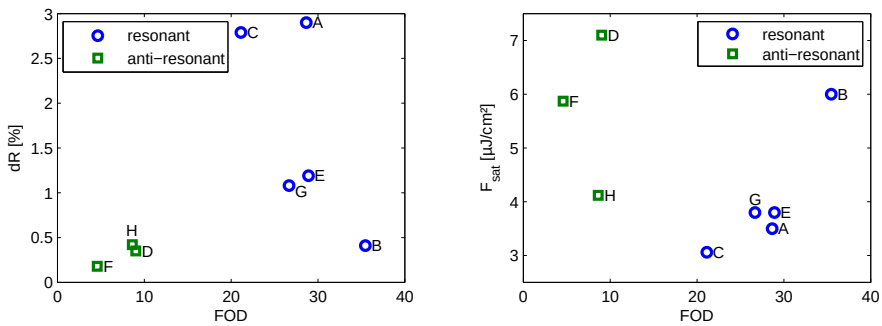

Figure 4.5: Dependence of (a) modulation depth and (b) saturation fluence on the figure of design (FOD, product of number of individual QD layers and enhancement factor, see text). Circles and squares indicate the FOD for a wavelength of 1042 nm.

as seen when comparing samples D and E to F and G, respectively. The spacing between individual layers inside a group, however, has a strong influence. This observation can be explained by a larger amount of defects obtained when growing closer-packed QD layers as a result of less strain relaxation. As sample H shows, an increased number of QD layers per group, as well as the increased nominal growth thickness of the QD layers, also contribute to increased losses from a supposedly increased number of defects.

4.5 Transient behaviour

A saturable absorber's relaxation behaviour is crucial for its capability to mode-lock a laser (in particular, in the absence of soliton-pulse shaping), as was argued in Section 2.2. The dynamics of a semiconductor absorber are usually simplified by a phenomenological bi-exponential behaviour, with one component accounting for the fast relaxation of the used transition and the other one accounting for the slow recombination and relaxation processes. The fast component, then, mainly determines the pulse shaping response while the slow component helps to asses an absorber's noise-removal and stabilisation capabilities.

Pump-probe setup

A non-collinear pump-probe setup was used to measure the temporal evolution of the absorbers' reflectivity after excitation. The laser source was the same as used in the characterisation of the nonlinear reflectivity (see Section 4.4). Also, the same attenuator mechanism was used to vary the excitation fluence. A schematic

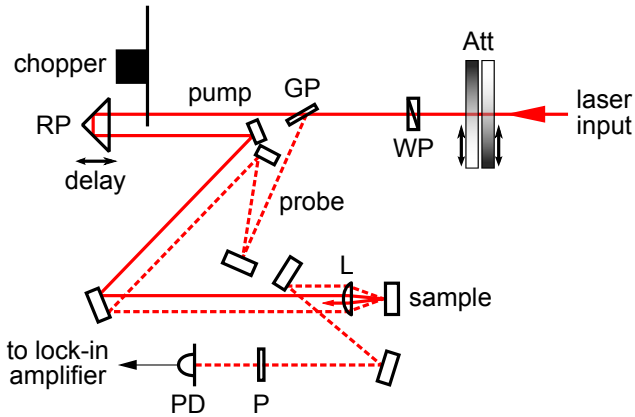

Figure 4.6: Schematic of the pump-probe setup. The input laser beam is attenuated by the graded attenuator pair *Att*. A half-wave plate (WP) is used to control the intensity of the *probe* beam (dashed path) which is split off by reflection from a wedged glass plate (GP). The pump beam passes a *chopper*. The pump-probe delay is controlled by the linear translation of the retro-reflector prism (RP). Both beams are focused by a lens (L) onto the *sample*. The reflected probe beam is picked up and directed towards a photo-diode (PD), which is connected to a lock-in amplifier. A polariser (P) is used to increase the contrast between pump and probe beam at the photo-diode.

of the setup is shown in Figure 4.6. The probe beam was generated by surface reflection from a glass plate (GP) at Brewster's angle. The intensity could then be controlled by a half-wave plate (WP) in front of it. It is important to keep the fluence of the probe beam in the absorber's linear regime, otherwise, saturation by the probe beam would distort the results. The probe beam's fluence was here at least two orders of magnitude lower than that of the excitation and, even for strong excitation, did not exceed the absorbers' saturation fluence.

The path length difference between the pump and the probe beam was controlled by a motorised delay line inside the path of the pump beam. A maximum delay of 25 ps was thus possible. The pump and the probe beams were focused onto a sample and the reflected portion of the probe beam was directed towards a photo-diode (PD). The pump beam was modulated by a chopper wheel and the chopping frequency was used as the reference signal for a lock-in amplifier, measuring the differential reflectivity, i.e. the measured signal would correspond to the change in the reflectivity relative to the linear reflectivity. Alignment of the sample was achieved by monitoring the spot size of the reflected beam. The position of the sample was then adjusted so that the reflected beam was collimated.

Name	# of QD layers	Rel. field	τ_f [ps]	τ_s [ps]	Amp. ratio
A	18	1.59	0.73	4.23	0.38
B	18	1.97	0.20	3.24	1.08
C	9	2.35	0.43	3.92	0.21
D	30	0.30	1.87	5.31	1.20
E	30	0.96	2.67	13.1	3.17
F	15	0.31	0.93	3.75	0.65
G	15	1.78	1.43	6.71	0.61
H	15	0.58	n.r.	n.r.	-

Table 4.3: Results from fitting a double exponential to the data acquired by the pump-probe experiment as described in Section 4.5. The last column contains the ratio of the fitted amplitudes of the two exponential terms (short/long). Excitation fluence was $3\,\mu J/cm^2$. The fit results obtained for sample H were below the experiment's resolution (i.e. not resolvable).

Results from pump-probe experiments

Table 4.3 summarises the results from all of the samples at an excitation fluence of $3\,\mu J/cm^2$. The results are also presented in Publication I. A double exponential model function was fitted to the experimental data to obtain fast and slow components. However, a constant offset was used as an additional fit parameter, in order to take into account the measured background signal. This background was the result of a very much slower component which was longer than the time window accessible by the experiment. This is the subject of a closer examination in the next section.

Apart from this observation, it can generally be noticed that a decreased spacing between the individual QD layers in a group for the samples A, B, and C decreases the relaxation times of both the slow and the fast components. This is probably due to a higher concentration of defects which work as a fast relaxation channel. However, increasing the number of QD layers per group, as in sample H, also facilitates a fast relaxation despite the intra-layer spacing being the same as in samples D-G.

Examples of the relaxation behaviour as a function of excitation fluence are given for samples A and G in Figure 4.7. The measured differential reflectivity is plotted as a function of the pump-probe delay and the excitation fluence. Each individual pump-probe data set has been offset so that the amplitude is zero before the pump pulse starts, for better visibility and to improve the data handling.

The response is distinctly different for strong excitation when compared to weak excitation, especially at larger delays. The complete data set is divided into three areas for closer examination (see Figure 4.7b): The relaxation after weak excitation

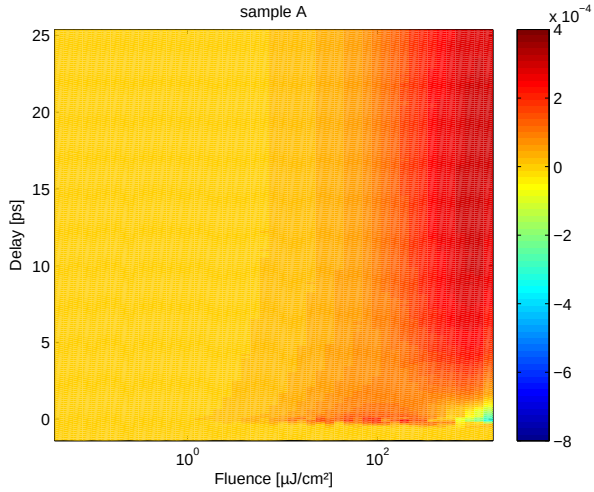

(a)

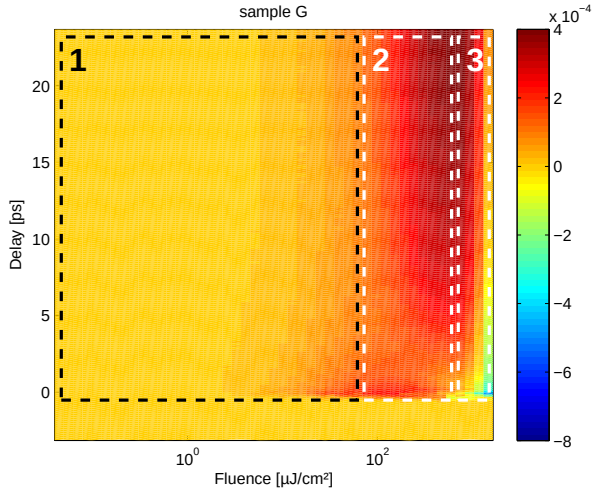

(b)

Figure 4.7: Differential reflectivity as a function of pump-probe delay and excitation fluence for samples (a) A and (b) G. The colour bar is in units of the lock-in amplifier output, i.e. volts. Figure 4.7b further shows regions 1–3 as explained in the text.

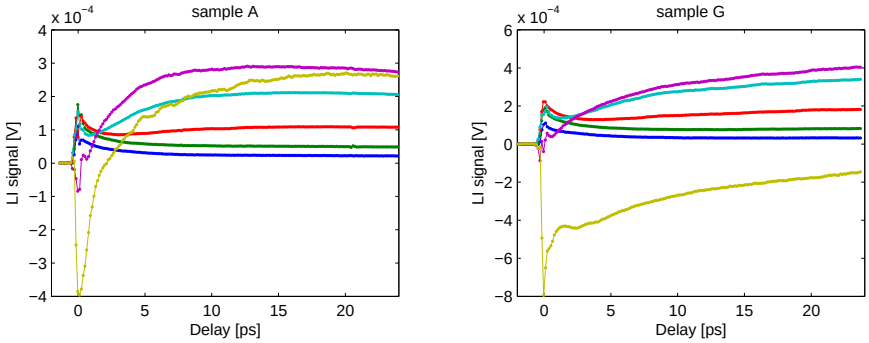

(a) (b)

Figure 4.8: Differential reflectivity as function of the pump-probe delay for samples (a) A and (b) G. The excitation fluences were 18, 44, 109, 170, 667, 1647 µJ/cm^2 (blue, green, red, cyan, magenta, yellow, respectively).

follows an exponential decay with an increased background signal for increasing fluence (Region 1). Close to the excitation pulse, the signal is well described by the model function for the nonlinear reflectivity (Equation (4.2)). Nevertheless, direct comparison, e.g. extraction of the absorber parameters, should be considered with caution since the pump-probe experiment is different from the nonlinear reflectivity experiment which was described in Section 4.4. For fluences above the roll-over of the reflectivity, i.e where TPA is strong, an additional rise is visible at a time delay on the order of 5 ps (Region 2). For even stronger excitation the response is dominated by absorption (Region 3). Since the delayed rise occurs for fluences larger than the roll-over fluence, it can be assumed not to be a direct result of TPA (as the roll-over itself), but instead related to the dynamics of TPA-generated carriers.

To further investigate these dynamics, the data from Figures 4.7 is plotted as pump probe traces in Figure 4.8. The initial fast relaxation is probably due to interaction with the wetting layer (WL), e.g. via Auger excitation, or capture by defect states (see Chapter 3, Section 3.4). This effect is used for mode-locking and the relaxation times should thus be as short as possible. Stronger excitation leads to saturation and filling of the QD ground state, which occurs very fast due to carrier-carrier scattering. The filled ground-state then prevents further relaxation and higher states remain populated. Even stronger excitation creates a large population of carriers in the continuum by TPA. The rising differential reflectivity for strong excitation at later times is then related to the capture of those free carriers by the QDs. The rise time is quantified by fitting an exponential to the rising signal. The result gives a time constant on the order of a few picoseconds. More importantly, the values obtained for sample A (closer spacing) are about a factor of two smaller than

for sample G (wider spacing), indicating that the carrier dynamics, i.e. diffusion and capture, are faster in sample A. This was also observed for samples B and C, which feature the same, closer packed configuration as in sample A. In the anti-resonant samples, the response is shifted towards stronger excitation. This is well explained by the lower field enhancement, which leads to weaker TPA. Additional information is provided in Publication II.

Photoluminescence experiments

Photoluminescence (PL) spectroscopy was performed on all of the samples to further investigate the long-time scale transient behaviour and the signal's persistent component. Instead of pumping the QD transitions directly, as in the pump-probe experiments mentioned above, the absorbers were now excited by a Ti:Sapphire laser centred at 782 nm and with a pulse duration of 200 fs; that means, the excitation of carriers occurred directly into the barrier material, thus simulating the effect of TPA. The PL spectra were then recorded with a streak camera as a function of wavelength and time after excitation. Figure 4.9 shows an example of such a recorded trace. The complete data set consists of three separate scans with centre wavelengths of 898 nm, 974 nm, and 1050 nm, respectively. The individual measurements were then combined by matching the signals in the overlapping wavelength regions. Different integration times for each different region also led to a varying noise level. The PL intensity is plotted on a logarithmic scale, in order to unveil the weak and persistent luminescence from the barrier at 875 nm($\hat{=}$1.417 eV). The signal between 950–1000 nm is identified as luminescence from the wetting layer (WL). The large peak around 1050 nm stems from the relaxation of the QDs.

It was found that the PL signal originating from the QDs appears at rather different positions in the optical spectrum. Comparison with the wavelength dependent enhancement factors (see Appendix B.2) suggests, that this is likely a result of cavity effects rather than serious growth errors. While the resonant samples show a PL peak close to the QD design wavelength of 1050 nm, the anti-resonant samples' PL spectra appear displaced. Figure 4.10a shows the integrated PL spectrum and the enhancement factor for sample A. Although both functions seemingly only differ by a constant offset (with respect to the wavelength), superimposing the main peaks does not match the signals for shorter wavelengths. Thus, it is concluded that a large enhancement factor keeps the PL photons from escaping the structure. The PL spectrum for two different excitation fluences is shown in Figure 4.10b. Both data sets are normalised to the peak value of the QDs' PL signal. It is observed that the PL signal at the long wavelength side of the QD luminescence peak does not change due to saturation.

Integration over the wavelength interval of the QD luminescence yields the relaxation behaviour as depicted in Figure 4.11 for samples A and F. The results for the other samples can be found in Appendix B.5. Comparing the absolute amplitudes of the PL signals at different excitation fluence for each sample reveals the saturation effect: while the amplitude scales with fluence for the red and green curves in

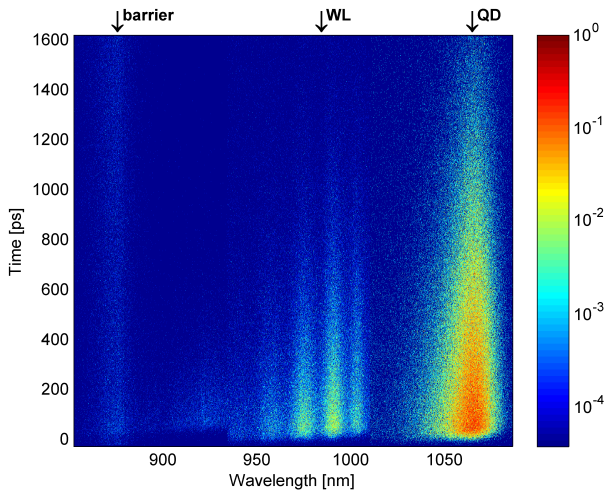

Figure 4.9: Time-resolved PL spectrum of sample A. The PL intensity is normalised and given in a logarithmic representation as a function of wavelength. The origin of the time axis is at the position of the PL signal's peak. Arrows indicate the PL signals from the barrier, wetting layer (WL), and quantum dots (QD), respectively.

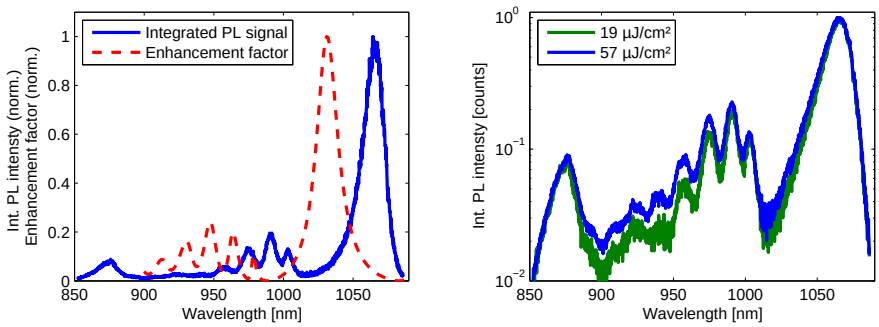

(a) (b)

Figure 4.10: (a) Integrated PL signal (blue, solid line) and normalised enhancement factor (red, dashed line) for sample A. Both data sets are normalised. (b) Normalised and integrated PL spectrum for sample A at two different excitation fluences.

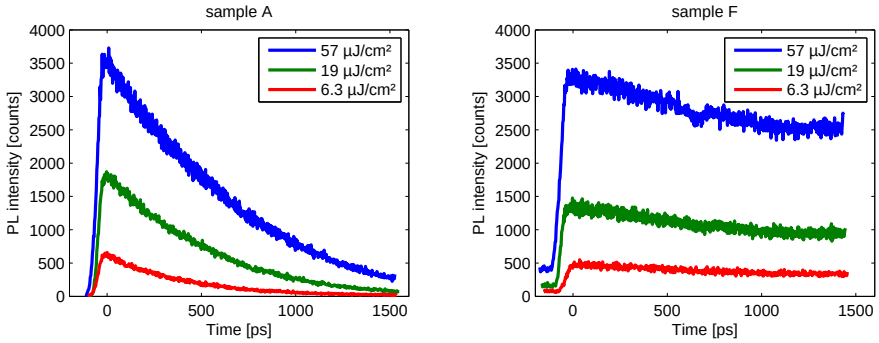

(a) (b)

Figure 4.11: Time-resolved PL measurement from samples (a) A and (b) F, at three different excitation fluences.

Figures 4.11, the relation becomes sub-linear for excitation at $57\,\mu J/cm^2$. Sample H seemed to additionally exhibit very efficient, non-radiative recombination since no PL signal comparable to those from the other samples could be observed, even at stronger excitation (see Figure 4.12). Furthermore, detailed study of sample H proved to be difficult due to the low signal level of the luminescence. For strong excitation ($550\,\mu J/cm^2$), integrating over the wavelength interval 1030–1086 nm yields the trace shown in Figure 4.12. The background signal is taken to be noise and a single exponential fit reveals a relaxation time of about 16 ps, which corresponds to the instrument's response limit. This observation indicates, that any excited QDs efficiently relax and that filling of the QD states from excess carriers in the barrier does not present an issue in this particular structure.

Table 4.4 presents the decay times of samples A–G for an excitation fluence of $19\,\mu J/cm^2$. For samples D–G, the order of magnitude of the PL time constant τ_{PL} can be estimated from the strength of the background signal just before excitation and the known excitation pulse separation of 13.6 ns. It is observed, that the PL time constant is especially long in the case of the wider spaced samples D–G, although not for sample H. The field enhancement, i.e. whether the structure is resonant or anti-resonant, seems to be less important.

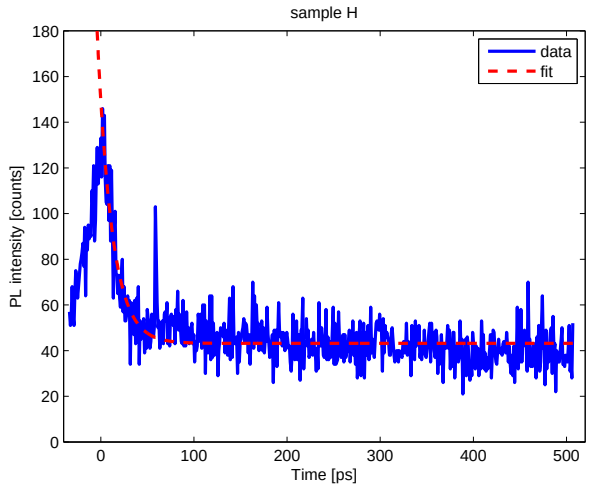

Figure 4.12: Time-resolved PL signal (blue line) for sample H, integrated over the wavelength interval of 1030 nm to 1086 nm. The excitation fluence was 550 µJ/cm^2 Also shown is a single exponential fit (red, dashed line) to the data.

Name	# of QD layers	Spacing [nm]	τ_{PL} [ns]
A	18	10	0.53
B	18	10	0.15
C	9	10	0.48
D	30	20	≈17
E	30	20	≈14
F	15	20	≈6.4
G	15	20	≈8.2
H	15	20	< 0.016

Table 4.4: QD-luminescence-time constants as obtained from a single exponential fit for samples A–C and H and estimated by the remaining background signal for samples D–G. The value for sample H is on the order of the instrument's response limit. The excitation fluence was 19 µJ/cm^2 for samples A–G and 550 µJ/cm^2 for sample H.

4.6 Summary

A set of eight QDSAs has been characterised with respect to dispersion, nonlinear reflectivity, and transient response. The number of individual QD layers as well as the spacing between them has been varied.

Resonant designs showed a strong modulation of the group delay dispersion (GDD) around the design wavelength, while anti-resonant designs generally led to smaller values of the GDD and less of a wavelength dependence. The general shapes of the theoretically obtained dispersion curves are well reproduced by the measurements and, also the absolute values of the calculated and measured GDD, are in good agreement.

Nonlinear reflectivity measurements revealed a low saturation fluence of a few microjoule per square centimeter for all samples. The saturation fluence did not show a strong dependence of the number of individual QD layers, but was affected by the structural design. The modulation depth, on the other hand, could be controlled by the number of layers as well as by the design. The measured values were in the range of 0.1–3 %. This demonstrated the decoupling of the saturation fluence and the modulation depth in these QD-based saturable absorbers. The non-saturable losses were found to be roughly on the order of the modulation depth in the respective sample, with the exception of sample H, where it was significantly larger as a result of an increased number of individual QD layers per group.

Pump-probe experiments confirmed an initial, ultra-fast relaxation for all samples. TPA and induced absorption were observed for strong excitation. A delayed rise of the reflectivity for strong excitation was explained with carrier capture from the barrier into the QDs. A long-living component on a nanosecond scale was identified and further examined by PL spectroscopy. Samples with a wider spacing between the individual QD layers of a group showed slower PL decay, pointing towards less defects because of improved strain relaxation. It also indicates a high-quality growth of the QDs, which might be desirable for light emitting devices (e.g. semiconductor lasers), but not for SSAs. Although sample H featured the wider spacing, its ultra-fast response was explained by additional defects induced by the larger QD group size. Its peculiar PL spectrum, as compared to those of the other samples, also pointed towards an efficient non-radiative recombination path.

Chapter 5

Quantum Dots for Mode-Locking

In this chapter, the results from mode-locking experiments with the quantum-dot saturable absorbers (QDSAs) that have been examined in the preceding chapter are presented. In all cases, Yb-doped, double tungstates were used as the gain medium and picosecond pulse durations were obtained. However, the general cavity design varied, leading to different regimes regarding the repetition rate and the output power. At first, a 1 GHz-repetition-rate laser is presented, demonstrating the suitability of quantum-dot-based absorbers for this type of low intra-cavity energy lasers. The second demonstration comprises a 200 MHz-cavity mode-locked with an absorber that exhibited a very long relaxation component on the order of nanoseconds. Nevertheless, stable pulses were obtained from this laser. The third system is an Yb-thin-disc laser, delivering picosecond pulses at an output power of several watts and, thus, demonstrating that the QDSAs can also be used in high-power applications. A summary of the main observations is given at the end of the chapter.

5.1 Gigahertz repetition-rate laser

An Yb:KYW[1] laser has been successfully mode-locked at a repetition rate of 1 GHz. The absorber used was sample H, with a measured saturation fluence of about $4\,\mu J/cm^2$, and with a fast relaxation time <200 fs due to a large concentration of defects arising from an increased number of individual QD layers per group.

The cavity design was an extended Z-type configuration (see Figure 5.1), where the gain medium was placed at the focal point between the two curved mirrors M1 and M2. The medium was pumped through mirror M1 by an InGaAs stack-diode laser at a wavelength of 980 nm (not wavelength stabilised). The mode-

[1] The exact formula is Yb:$KY(WO_4)_2$. The expression Yb:KYW will be used as an abbreviation throughout this thesis.

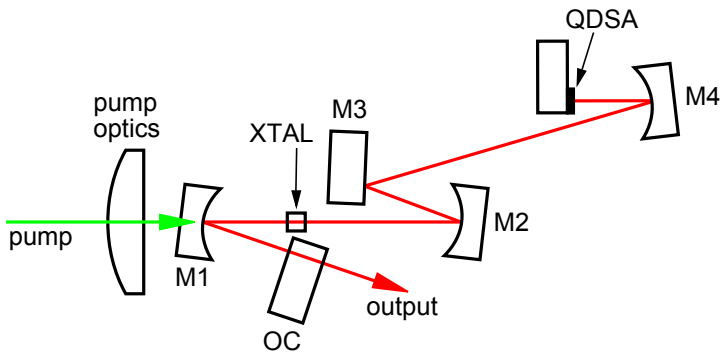

Figure 5.1: Cavity layout: pump optics: aspheric lens, focal length 30 mm. OC: outcoupling mirror, 1 % transmission. Mirrors M1 to M4 are HR-coated ($R > 99.9\,\%$) for the laser wavelength; M1 and M2 are also AR-coated ($R < 2\,\%$) for the pump wavelength (980 nm). Radii of curvature are 25 mm for M1 and M4 and 50 mm for M2; M3 is flat.

area ratio of the laser mode to the pump mode was 38 %. One arm contained an outcoupling mirror (OC) defining the one of the two cavity ends, the other arm contained an additional curved mirror (M4), focusing the laser mode onto the saturable absorber placed at the other end of the cavity. The total cavity length was 145 mm, corresponding to a repetition rate of 1.036 GHz.

Results

Lasing started at a threshold pump power of 130 mW. Upon an increase of the pump power, Q-switching instabilities were observed above an output power of 42 mW. Mode-locking started at an output power of 66 mW. The regime of CWML showed a slope efficiency of 10.8 %. A maximum output power of 339 mW was achieved, limited by the damaging of this particular QDSA at this power level. The laser output power versus the pump power is shown in Figure 5.2. The change in slope efficiency at around 1 W of pump power is related to the spectral shifting of the pump diode. For better comparison, linear fits for both configurations were calculated only at those pump powers where mode-locking was achieved with the absorber in position.

The output power at the threshold of CWML corresponds to a pulse fluence of $165\,\mu J/cm^2$ on the absorber, i.e. a saturation parameter of $S_A \approx 41$. At first, this appears to be rather large, considering that mode-locking with semiconductor saturable absorbers (SSAs) has generally been observed to be possible for smaller saturation parameters (on the order of $S \approx 3$–5). Using the stability criterion (Equation (2.13)), the product of the saturation parameters is approximately $0.78 \cdot$

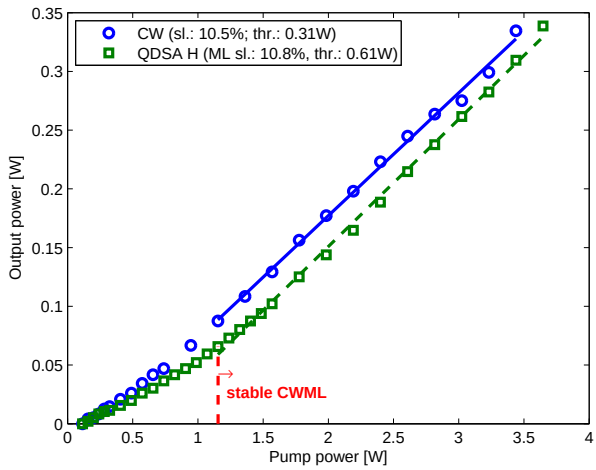

Figure 5.2: Slope efficiency of the 1 GHz laser mode-locked with QDSA sample H (green squares) in comparison to the cavity's CW performance (blue circles). The red, vertical line indicates the beginning of the CWML regime.

10^{-3} at CWML threshold (see Table 5.1 for the assumed parameters). The term that takes into account the upper laser-level life-time was included and accounts for about 8 % of the total value. This number is a few times smaller than the actually measured modulation depth. The observation that mode-locking in fact seems to start earlier than predicted by the criterion, has to be taken with caution, considering the assumptions made when deriving the criterion as well as noting the potential uncertainties for the various values which were used in the calculation.

The optical spectrum at threshold was located at a wavelength of 1035.7 nm and shifted towards shorter wavelengths when increasing the pump power. The CW and the mode-locked spectrum are shown in Figure 5.3a, the latter was recorded at a laser output power of 216 mW. The FWHM of the main spectral component is 1.48 nm (i.e. disregarding the peak on the flank at 1034 nm). The pulse width at about the same output power was measured with an intensity autocorrelator and was determined to be 2.08 ps (see Figure 5.3b). The time-bandwidth product is then 0.86, indicating chirped output pulses. This is reasonable, considering that the absorber's negative dispersion of about -1000 fs^2 overcompensated for the material dispersion from the laser gain medium ($\approx$ 800 fs^2). Furthermore, soliton shaping in this case is weak due to the low peak power and cannot contribute significantly to the pulse shaping. The absorber, thus, plays a main role in defining the pulse duration and also has a detrimental influence on the pulse shape, as revealed by the autocorrelation trace. The rising flanks at higher powers indicate an asymmetric

Parameter		Values	Values
Repetition rate	f_{rep}	1.036 GHz	222 MHz
Wavelength	λ	1032 nm	1038 nm
Intra-cavity pulse energy	E_{p}	6.35 nJ	16 nJ
Absorber saturation fluence	$F_{\mathrm{sat,A}}$	$4\,\mu\mathrm{J/cm^2}$	$7.1\,\mu\mathrm{J/cm^2}$
Gain saturation fluence	$F_{\mathrm{sat,L}}$	$4.8\,\mathrm{J/cm^2}$	$5.8\,\mathrm{J/cm^2}$
Emission cross section	σ_{e}	$2 \cdot 10^{-20}\,\mathrm{cm^2}$	$1.5 \cdot 10^{-20}\,\mathrm{cm^2}$
Absorption cross section	σ_{a}	$0.2 \cdot 10^{-20}\,\mathrm{cm^2}$	$0.15 \cdot 10^{-20}\,\mathrm{cm^2}$
Upper laser-level life-time	τ_{l}	0.6 ms	0.6 ms
Mode size on the absorber	w_{A}	35 µm	85 µm
Mode size in the gain medium	w_{L}	50 µm	100 µm
Absorber saturation parameter	S_{A}	41	10
Gain saturation parameter	S_{L}	$1.9 \cdot 10^{-5}$	$0.9 \cdot 10^{-5}$

Table 5.1: Parameters used for the calculation of the saturation parameters for the gain and the loss for the two different Yb:KYW lasers. The values for the life-times and the cross-sections were taken from [145].

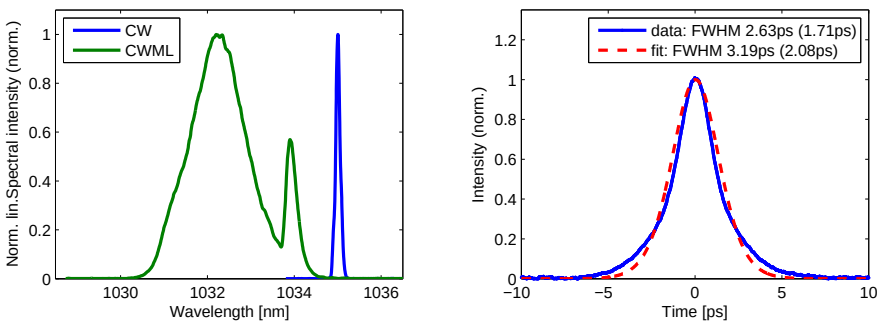

(a) (b)

Figure 5.3: (a) Optical spectra of the 1 GHz laser, mode-locked with sample H. The spectrum at threshold is plotted as a blue line, the mode-locked spectrum is shown as a green line. The spectra are single-shot measurements with a resolution bandwidth of 0.07 nm. (b) Intensity autocorrelation trace and fit at an output power of 77 mW (assuming a sech^2-shaped intensity profile). The FWHM pulse durations for the measured trace and fit are 1.17 ps and 2.08 ps, respectively.

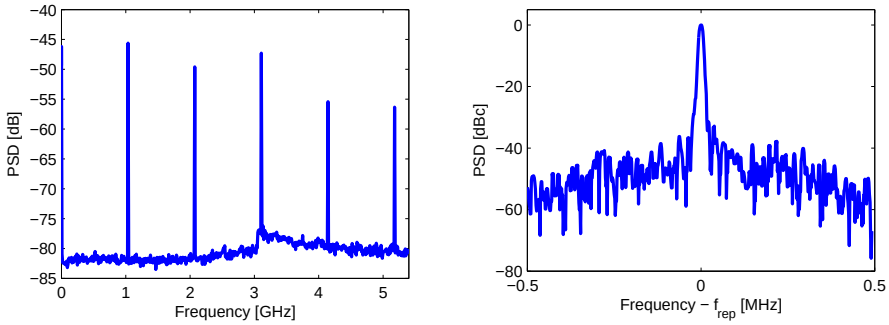

(a) (b)

Figure 5.4: RF spectra of the mode-locked 1 GHz laser. (a) Wide range scan, showing up to the 5th harmonic of the repetition rate. The measurement is an average of 100 single shots, the resolution bandwidth is 1 MHz (b) Single shot of the spectrum around the fundamental repetition rate f_{rep}. The spectrum is normalised to the amplitude at the repetition rate. The resolution bandwidth is 9.1 kHz.

pulse shape as a result of the absorber action.

CWML was further examined by measuring the RF (radio frequency) spectrum. Figures 5.4 show the frequency comb as well as a close shot of the spectrum around the fundamental frequency f_{rep}. The wide pedestal, which is visible in Figure 5.4b, indicates amplitude noise (the instrument's noise level for this measurement was at -60 dB relative to the maximum value). This noise is explained by the destabilisation of the laser pulses as a result of additional absorption loss due to carriers generated by two-photon absorption (TPA). The noise pedestal broadened upon the increase of the pump power due to an increased amount of TPA. Further details on this laser experiment are given in Publication III.

5.2 Megahertz repetition-rate laser

A longer cavity, with a repetition rate of 222 MHz, has been mode-locked by using sample D. This particular sample had a measured saturation fluence of 7 µJ/cm^2 and a modulation depth of 0.35 %. The transient response indicated a long recombination time for the QDs' ground state. This recombination time was on the order of 17 ns, as was estimated from the time-resolved PL measurements. The cavity round-trip time, on the other hand, was only 4.5 ns. It follows, then, that the absorber could not fully recover between two pulses, consequently, the effective modulation depth might have been reduced.

A schematic of the layout is shown in Figure 5.5. The cavity had a Z-type layout, i.e. comprised of two curved mirrors (M2 and M3) and two flat end mirrors

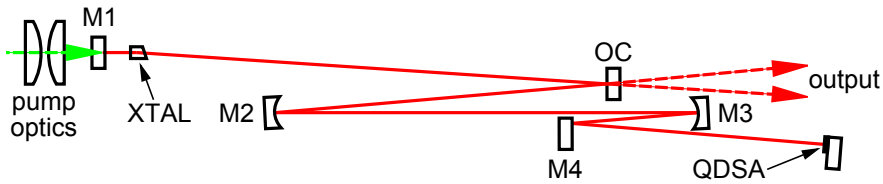

Figure 5.5: Layout of QDSA mode-locked 222 MHz cavity. OC: outcoupling mirror, 1 % transmission. Mirrors M1 to M4 are HR-coated ($R > 99.9\,\%$) for the laser wavelength; M1 is also AR-coated ($R < 2\,\%$) for the pump wavelength (980 nm). Radii of curvature are 150 mm for M1 and 100 mm for M2; M4 is flat.

(M1 and the QDSA). The cavity was end-pumped and the outcoupling mirror was placed in a folding position, thus yielding two output beams. An outcoupling mirror with 1 % transmission was used, i.e. the total outcoupling loss was 2 %. The overall cavity length in this experiment was 675 mm, corresponding to a repetition rate of 222 MHz.

For mode-locking, the saturable absorber (sample D) was used at the end of the cavity. This sample featured an anti-resonant design and 30 layers of QDs, organised in 10 groups. The second-order dispersion at the laser wavelength was slightly positive. Cavity mode simulations showed a laser spot size of 85 µm on the absorber.

Results

Lasing started at a threshold pump power of around 5 W and CWML set in at a pump power of 6 W, while delivering an average output power of 71 mW. The mode-locking became unstable at output powers exceeding 133 mW. The overall slope efficiency was 7.2 %. When replacing the QDSA by a high-reflective dielectric mirror, the lasing threshold and the slope efficiency changed to 3.7 W and 18.2 %, respectively. The significantly reduced performance, when using the QDSA, can be explained by the incomplete relaxation of the absorber and the subsequently induced absorption loss. The measured output power for both configurations is shown in Figure 5.6.

The saturation parameter S_A for the absorber was in the range of 10 to 20 for stable mode-locking. This is less than that of the 1 GHz system as described in Section 5.1. Also, the gain saturation was smaller, since the mode-size in the laser crystal was larger (about 100 µm). The gain saturation parameter S_L was on the order of $0.9 \cdot 10^{-5}$. These parameters are also given in Table 5.1. Using the stability criterion yields that the modulation depth would have to be more than one order of magnitude smaller than the actual measured value, i.e. around $0.16 \cdot 10^{-3}$ instead of $3.5 \cdot 10^{-3}$. As it was already argued above, this observation emphasises the limits of the criterion's applicability as a result of the many uncertainties that all of the

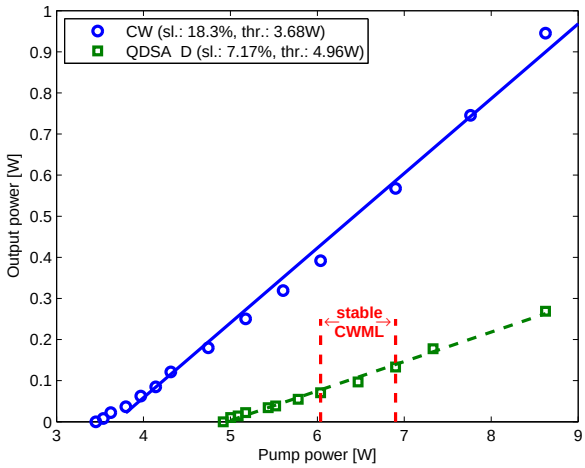

Figure 5.6: Slope efficiency of the 222 MHz laser, mode-locked with QDSA sample D (green squares) in comparison to the cavity's CW performance (blue circles). The red, vertical lines indicate the region of stable CWML.

involved parameters are subject to. In addition, the absorber's long relaxation time only allows for a partial recovery during the cavity round-trip time, thus, effectively reducing the modulation depth.

The laser at threshold operated at a wavelength of 1038.7 nm, shifting towards shorter wavelengths with increasing power, until mode-locking started with a centre wavelength of 1037.5 nm (see Figure 5.7a). Upon further increase of the pump power, the centre of the spectrum shifted back towards longer wavelengths. Also given in the figure are the Fourier-limits as calculated from the spectral bandwidth. While the theoretical pulse duration decreased with increasing power, the measured pulse duration actually increased. An example of an autocorrelation trace, showing an FWHM pulse duration of 6.3 ps at an output power of 97 mW, is shown in Figure 5.7b.

The measured RF spectra further verified stable mode-locking (see Figures 5.8). The two sidebands shown in Figure 5.8b indicate an instability due to relaxation oscillations, i.e. a Q-switching instability. The effect was more pronounced for lower powers, where the saturation of the absorber was weaker and Q-switching instabilities had a larger influence.

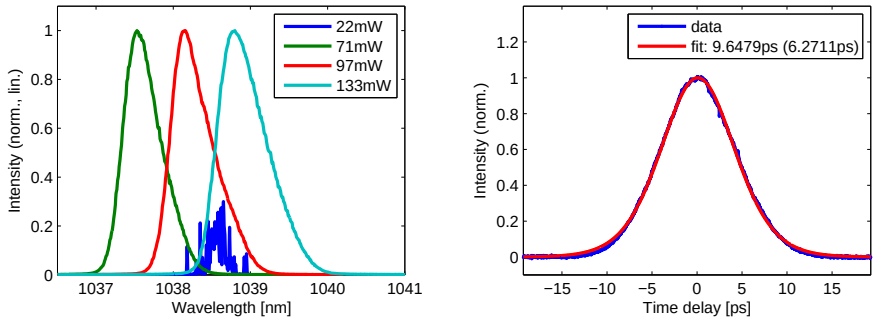

(a) (b)

Figure 5.7: (a) Optical spectrum of the 222 MHz laser, mode-locked with QDSA sample D. The spectrum at threshold (blue) is plotted with a reduced amplitude to increase the visibility of the mode-locked spectra. The calculated Fourier-limit for the mode-locked spectra is, from left to right, 2.1 ps, 1.9 ps and 1.6 ps, respectively. The mode-locked spectra are averages of 5 single-shot measurements, the CW spectrum is a single-shot measurement. The resolution bandwidth is 0.05 nm. (b) Intensity autocorrelation trace and fit (assuming a sech^2-shaped intensity profile) at an output power of 71 mW.

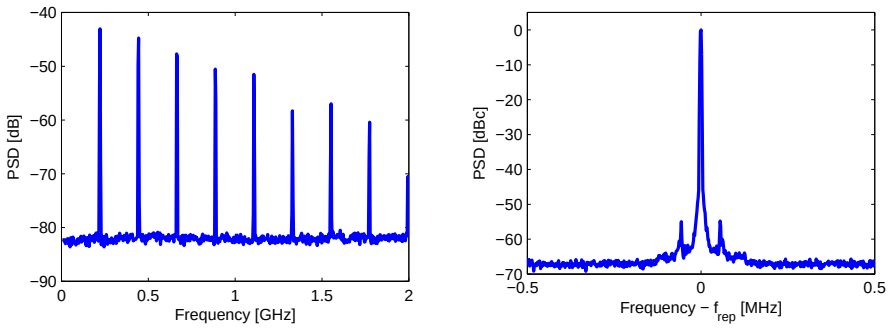

(a) (b)

Figure 5.8: RF spectra of the mode-locked 222 MHz laser. (a) Wide range scan, showing up to the ninth harmonic of the repetition rate. The resolution bandwidth is 3 MHz. (b) RF spectrum around the fundamental repetition rate f_{rep} and at an output power of 133 mW. The spectrum is normalised to the amplitude at the repetition rate. The resolution bandwidth is 9.1 kHz. Both graphs are averages of 100 single-shot measurements.

5.3 Thin-disc laser

As a proof of principle, the QDSAs were also used to mode-lock an Yb:KYW thin-disc laser. Thin-disc lasers feature a thin laser-gain-medium which can be efficiently connected to a heat sink, thereby offering excellent heat removal. The improved thermal characteristics allow strong pumping and, subsequently, high output powers from this type of laser [146]. The results presented here, thus, permit conclusions regarding the QDSAs' damage threshold.

Laser setup

A schematic of the cavity layout is given in Figure 5.9. The gain medium was an Yb:KYW disc with a doping concentration of 10 % and a thickness of 110 µm. The disc was pumped by a fibre-coupled pump diode with a maximum output power of 50 W at a wavelength of 980 nm. The complex design of the pumping scheme yielded 24 passes of the pump beam through the disc, at an effective pump mode-size of 600 µm. The laser mode was folded over the disc twice, i.e. the gain medium was passed four times per round-trip. The laser mode-size was about $450 \times 430\,\mu m^2$ and approximately the same for both folds. The total cavity length was 3.97 m, corresponding to a repetition rate of 37.8 MHz. An outcoupling mirror (OC) with a transmission of 5 % was placed at one cavity end, and the saturable absorber was placed at the other end, where the laser mode size was $200 \times 225\,\mu m^2$. The QDSAs were fixed to a copper mount with heat-sink paste; no active cooling was used. The optical spectrum could be controlled by a 1 mm thick birefringent plate inside the cavity. The intra-cavity dispersion could be changed by replacing some of the folding mirrors with suitable dispersive mirrors.

Results

The best performance was achieved with sample A and with an additional intra-cavity dispersion of -6000 fs^2 (the material dispersion from the gain medium included). CWML started at a pump power of 29 W and with an output power of about 4 W. Up to 13 W of output power could be achieved, limited by the available pump power. The slope efficiency of the mode-locked laser was 42 %. This was comparable to the CW performance of this cavity, which is shown, together with the mode-locked performance, in Figure 5.10.

Wavelength tuning could be achieved by rotating the birefringent plate around the axis normal to its surface. Figure 5.11a shows the optical spectra for different configurations of the birefringent plate and at an output power of about 6 W. For longer wavelengths, the laser tended to Q-switch or to Q-switch mode-lock instead of running in a clean CWML mode. The observed spectral bandwidth theoretically supports sub-picosecond pulse durations. However, an intensity autocorrelation trace is presented in Figure 5.11b, showing a measured pulse duration of 1.6 ps.

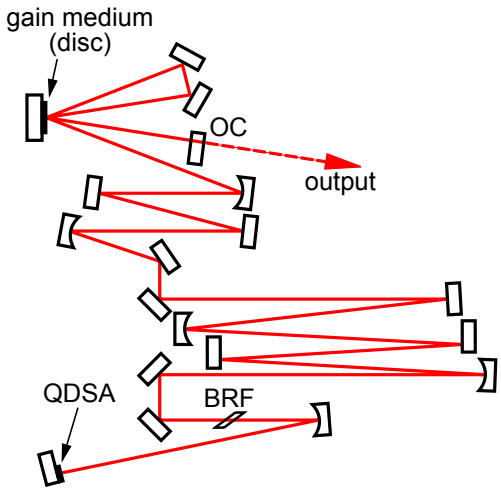

Figure 5.9: Cavity layout of the mode-locked thin-disc laser. The pump chamber and the pump beams are omitted for better visibility. OC: outcoupling mirror with a transmission of 5 %. All other mirrors are high-reflective mirrors. The mirrors with a small folding angle can be replaced by dispersion compensating mirrors. BRF: birefringent plate with a thickness of 1 mm. More information on the principle laser setup can be found in [147].

At the threshold of CWML, the pulse fluence incident on the absorber was 0.7 mJ/cm^2; whereas at the maximum output power of 13 W (pump limited), the pulse fluence on the absorber was 2.4 mJ/cm^2. With a pulse duration of 1.6 ps, this corresponds to a peak intensity of 1.5 GW/cm^2. CWML could also be achieved with samples B, E, F and G at slightly varying threshold. No damage was observed on samples A–G, even for operation at the maximum pump power. Although quantum-well absorbers have already been demonstrated to operate at energies and peak powers which are two orders of magnitude larger than those described here [139, 148], the obtained results for quantum dot absorbers indicate that the fabrication techniques at present are mature enough to keep non-saturable losses small and, thus, to enable high-power applications. In addition, it has to be noted that the QDSAs presented here did not feature any special top-coating and that the resonant samples provided strong field enhancement at the operational wavelength of 1030 nm (according to the simulation; see figures in Appendix B.2).

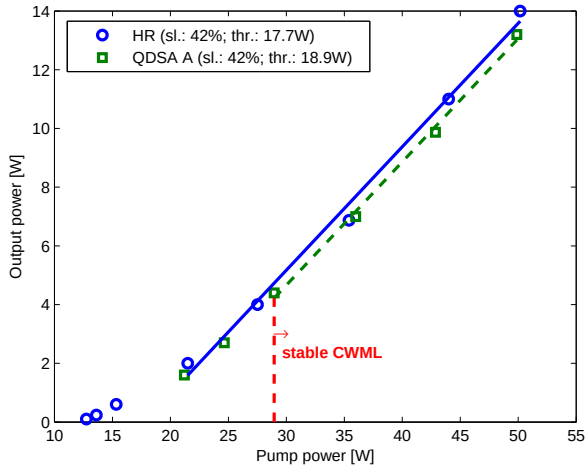

Figure 5.10: Performance of the Yb:KYW thin-disc laser in CW operation (blue circles) and CWML operation using sample A (green squares). The red, vertical line shows the beginning of the CWML regime. The lines are fits to the data points above a pump power of 20 W, to calculate the slope efficiency (given in the legend).

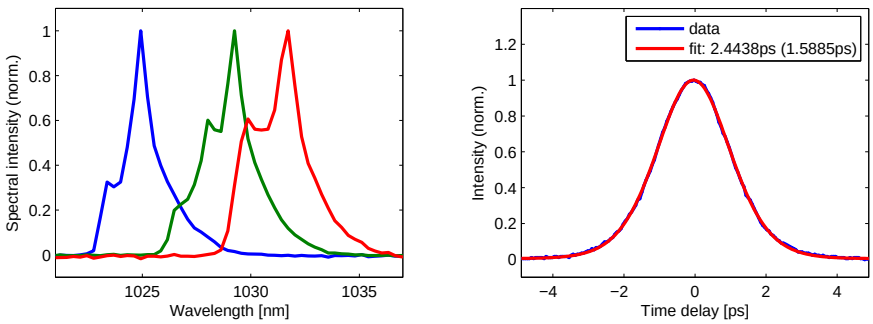

Figure 5.11: (a) Optical spectrum of the mode-locked Yb:KYW thin-disc laser at an output power of around 6 W for different configurations of the birefringent plate. The graphs are single-shot measurements, the resolution bandwidth is 1 nm. (b) Autocorrelation trace and a fit, assuming a sech^2-shaped intensity profile (red line), yielding a pulse duration of 1.6 ps.

5.4 Summary

In this chapter, three lasers mode-locked with quantum-dot saturable absorbers were demonstrated. All lasers were based on Yb:KYW as the gain medium and delivered picosecond pulses with optical spectra in the wavelength region of 1020–1040 nm. Output powers of a few hundred milliwatts were obtained at repetition rates of 1.036 GHz and 222 MHz. Output powers on the order of watts were obtained from an Yb-thin-disc system. All of the saturable absorbers were based on self-assembled InGaAs quantum dots, thereby proving that the same technology can be used for mode-locking of various cavity configurations. The quantum dots' versatility is further emphasised when considering reports of femtosecond pulses obtained with InGaAs quantum dots [113, 149] in addition to the picosecond pulse durations presented here.

A high tolerance for strong excitation was demonstrated for samples A–G, which endured pulse fluences of up to 2.4 $\mathrm{mJ/cm^2}$ without damage. The lower repetition rate allowed a more complete relaxation during a single round-trip, thus lowering the loss by free-carrier absorption. It is then concluded that free-carrier absorption has a major influence on the damage threshold of QDSAs. Furthermore, the performance of sample H indicated that a design-conflict exists between many defects for fast relaxation and few defects for high damage threshold. As the demonstration of mode-locking with sample D showed, a slow recombination of the QDs' ground state does not necessarily prohibit mode-locking, but affects the laser's efficiency.

Chapter 6

Carbon Nanotubes for Mode-Locking

This chapter describes the use of single-walled carbon nanotubes as saturable absorbers for mode-locking of lasers. First, an overview of the field is given, highlighting some important findings and developments in this area. Following that, the properties of carbon nanotubes are presented and a general description of the fabrication process for carbon-nanotube-based absorbers is given. Finally, the results from mode-locking an optically-pumped semiconductor-disc laser (OPSDL) employing a carbon nanotube saturable absorber are presented, including details on the fabrication and properties of the used absorber.

6.1 Overview

Carbon nanotubes (CNTs) have attracted attention as saturable absorbers by exhibiting ultra-fast relaxation and the possibility to operate over a wide range of wavelengths. In the beginning, the purity and the selection of CNTs have been issues. This is also the reason why successful mode-locking with CNT-based absorbers was first demonstrated in fibre lasers [42], which tolerate significantly higher insertion losses than bulk, solid-state lasers or semiconductor lasers.

The first demonstration of a bulk, solid-state laser mode-locked with CNTs featured pulses with a duration of 68 fs from Er/Yb:glass [43]. It is particularly interesting to note that this short pulse duration was obtained without exploitation of any KLM mechanism, but that the pulse shaping was solely governed by the absorber's fast relaxation. Indeed, the authors of [43] note that the pulse duration was, in fact, limited by the spectral bandwidth of the cavity mirrors. A wide range of bulk, solid-state laser materials followed and it was demonstrated that CNT saturable absorbers (CNTSAs) could mode-lock lasers spanning the wavelength region from 800–2000 nm [22].

CNTSAs have also been compared with the more established technology of semiconductor absorbers and found to be able to exhibit all of the appropriate prop-

erties for equally successfully mode-locking the same lasers [150]. Numerous other demonstrations underline the observation that good performance can be achieved with CNTSAs [151–153]. However, fabrication of CNTSAs is considered to be significantly simpler than that of semiconductor absorbers. CNTSA fabrication is usually based on the incorporation of the CNTs into a plastic host matrix, spin-coated onto any suitable element located inside a laser cavity. It has to be pointed out, that CNTSAs can equally well be fabricated for use in transmission as in reflection, as opposed to semiconductor absorbers (see Section 4.1). In addition, the semiconductor technology requires growth in an MBE (molecular beam epitaxy) machine or with a similar technology for the deposition of the semiconductor material, which usually involves a high investment cost. On the other hand, it offers a high precision and a good control over the fabrication of semiconductor absorbers. However, the fabrication parameters for CNTSAs and also the parameters describing the raw CNTs themselves, are of equal importance as the growth parameters during fabrication of semiconductor structures.

CNTs themselves can be fabricated in various ways. The methods most often used are arc-discharge (arc-made) [154, 155] and high-pressure carbon monoxide decomposition (HiPCO) [156] (more methods are described in [157]). The length and diameter distributions of the CNTs change slightly for the various methods, e.g. HiPCO CNTs have been observed to generally be shorter than arc-made CNTs, thus being less prone to curling and the subsequent formation of agglomerates. Also, CNTs can be either single-walled, i.e. resembling a simple tube made from a single layer, or multi-walled. For most applications, including mode-locking of lasers, single-walled CNTs are used. Multi-walled CNTs show a larger saturation intensity and, generally, display a metallic behaviour, due to the several layers they are composed of. The specific electronic structure of single-walled CNTs is not preserved in multi-walled CNTs. In this thesis, the term *CNT* exclusively refers to the single-walled type, which are sometimes abbreviated as *SWCNT* in the literature.

6.2 Properties of carbon nanotubes

CNTs derive their main properties from their tube-like structure (see Figure 6.1). A single nanotube features a cylindrical shape, with the surface made of carbon atoms arranged in a graphene-like pattern. In fact, CNTs resemble rolled-up graphene sheets. CNTs which are used for mode-locking of lasers are usually single-walled, i.e. they have the simplest possible tube structure. A number of possible combinations exists for rolling up a sheet of graphene and connecting its sides. The exact pattern is described by the *chirality*, which is quantified by the roll-up vector, which, in turn, defines the periodicity when following a CNT's circumference [158–160]. The numerous possible combinations are separable into two basic classes: metallic and semiconducting. Of primary interest for laser mode-locking are CNTs of the semiconducting variety, which exhibit a discrete energy level structure. Metallic

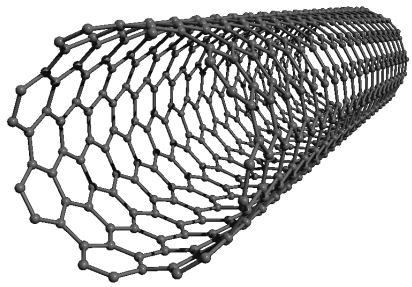

Figure 6.1: Schematic of a single CNT (single-walled) with chirality (8,7) and a diameter of about 1 nm. The length is reduced for better visibility.

CNTs, on the other hand, are efficient absorbers, jeopardising the otherwise high damage threshold of the semiconducting CNTs. The ratio of semiconducting and metallic CNTs in a random distribution is about 2:1 [161].

The length of the roll-up vector defines the circumference and, hence, the chirality defines the diameter. The diameter of CNTs, in turn, determines the absorption spectrum. Since CNTs are one-dimensional nano-structures[1], their energy spectrum is of a discrete nature and of the same type as for nano-wires [162] (see Figure 6.2 as well as Figure 3.2 in Chapter 3). The exact positions of the energy levels are then defined by the dimension in the direction of the confinement and, consequently, the radius of the CNT. The specific values depend on the chirality of the CNT in question [158]. In general, however, the energy gap grows with increased confinement, i.e. decreasing diameter (see also the discussion for QDs in Section 3.4). For a detailed derivation and discussion, see, e.g. [163].

The lowest-order transition energy is located in the NIR region for a CNT diameter on the order of 1–2 nm [160]. Only a slight variation of the diameter already leads to considerably different transition energies. As a consequence of the fabrication techniques, the diameter distribution is usually large enough to support broad-band operation, as was mentioned above.

Several CNTs in a suspension can form larger bundles made from curled-up CNTs, leading to increased scattering losses, which effectively presents a linear loss. It has been found that a proper dispersion, and particularly un-curling of the CNTs in a suspension, significantly improves an absorber's performance in terms of its suitability for mode-locking of lasers [22, 74]. Nevertheless, it has also been noted that a certain degree of bundling is beneficial for reducing the relaxation time, because of the then possible interaction between various CNTs. Dispersion and un-bundling of CNTs, then, represent crucial steps in the absorber fabrication (see also Section 6.3).

[1] Strictly, the label *nano* only applies to the confined dimensions. The length of CNTs used for laser mode-locking is usually on the order of micrometers.

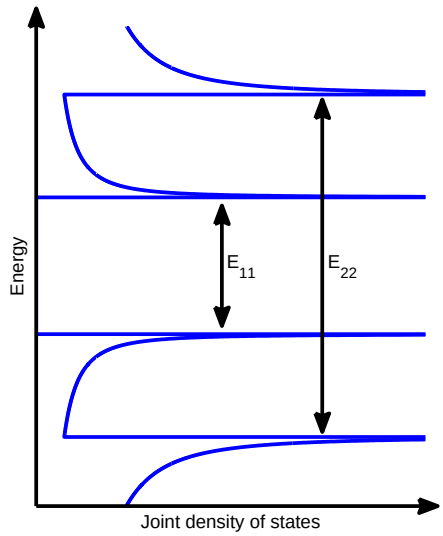

Figure 6.2: Schematic of a CNT's energy level structure. The transition energy between the ground states is labelled E_{11}, the energy between the first excited states is labelled E_{22}.

The relaxation dynamics in CNTs generally follow the model which is also used for semiconductors. Namely, the transient behaviour is composed of a fast intra-band and a slower inter-band component. Fast relaxation times of down to 70 fs have been reported and sub-picosecond values, as in QDs, are common [22].

6.3 Fabrication of carbon nanotube saturable absorbers

Several methods for the fabrication of CNTSAs exist [164–168]. However, the one described in this section has proved to be very reliable and is widely used nowadays. The main steps are:

- Pre-treatment of the CNTs.
- Mixing of the CNTs with a solution containing the host material.
- Spin coating the mixture onto a suitable substrate.

All three steps offer numerous parameters for controlling the resulting behaviour. They are described in detail in the following.

CNT pre-treatment

The very first step usually consist of dry-heating the raw CNTs to remove any water, which would otherwise lead to a disadvantageous chemical behaviour when preparing the CNT solution. The dried CNTs are then dispersed in a suspending medium. DCB (1,2-dichlorobenzene) is an excellent agent for suspending various kinds of carbon structures and is, consequently, often used. An additional surface surfactant may also be employed to further increase the dispersibility. A common choice is PmPV (poly[(m-phenylenevinylene)-co-(2,5-dioctoxy-p-phenylenevinylene)]) [169]. Alternatively, CNTs can also be suspended in water when using a proper surfactant (e.g. SDS (sodium dodecyl sulfate)) [170]. The above mentioned dry-heating is then not necessary. This provides a less toxic solution; however, the host material in the next step, then, also has to be soluble in water. Nevertheless, any surfactant potentially presents an additional absorption loss and a suitable compromise has to be found between the surfactant's favourable and unfavourable influences.

The CNT suspension is then subject to ultra-sonication, in order to un-bundle any existing CNT agglomerates. This treatment might also help to break down longer CNTs into shorter ones, which reduces the tendency for curling. In addition, the suspension can be centrifuged to remove larger bundles and impurities which are not CNTs.

Mixing with the host material

A solution containing the host matrix material is prepared in parallel to the CNT suspension, usually using the suspending agent as a solvent. It is important that the solution containing the host material mixes well with the CNT suspension. A common choice is PMMA (poly(methyl methacrylate)), dissolved in DCB, but also cellulose or gelatin, dissolved in water, are possible. PMMA shows good optical properties, namely a reasonably good damage threshold and a broad-band transparency. The length of the polymer chains, then, essentially determines the behaviour of the mixture during the spin-coating process. Finally, the host-material solution is mixed with the CNT suspension at the desired ratio and stirred, or even sonicated, to assist the mixing.

Spin coating

The CNT/host-material mixture is then spin-coated onto the chosen substrate. In principal, both transmission- and reflection-type absorbers are possible and have been successfully used. A thin glass plate is normally used for the fabrication of transmission-type absorbers; for reflection-type absorbers, however, the solution can be spin-coated directly onto a dielectric mirror. The typical thickness of the absorber film is well below 1 µm and typically on the order of a few 100 nm. Since the absorber thickness is well below the target wavelength, the position of the absorber inside the cavity should be carefully considered. Especially when using a

reflection-type absorber as a cavity end-mirror, it has to be noted that the electric field at the absorber position will be significantly reduced, compared to a position inside the cavity.

6.4 Mode-locking with carbon nanotubes

A CNTSA was successfully employed for mode-locking of an optically-pumped semiconductor disc-laser (OPSDL). This type of gain material suffers from a low gain and, thus, a low absorber loss is imperative. The laser was mode-locked at a relatively high repetition rate of 613 MHz, thus, demanding a low saturation fluence of the absorber. Both demands were well met by the CNTSA used in the mode-locking experiment. The absorber and the resulting mode-locking performance are briefly described in the following. Further information can be found in Publication IV.

Absorber

A transmission-type CNTSA was fabricated by spin-coating of a thin PMMA film, containing CNTs, onto a glass substrate. The CNTs had been produced by the arc-discharge method and had an average diameter of 1.4 nm. The CNTs were dispersed in DCB at a ratio of 0.1 mg of CNTs per 1 ml of DCB. PmPV was added as a surfactant at a ratio of 5 mg per 1 ml of DCB and the mixture was sonicated in order to assist dispersion of the CNTs in the suspension. The host material was prepared as a solution of PMMA in DCB at a ratio of 100 mg per 1 ml. This solution was then mixed with the CNT suspension at a volume ratio of 1:1 and, subsequently, stirred. The mixture was then centrifuged in order to remove residual impurities and larger agglomerates. The remaining mixture was again well stirred and, finally, spin-coated to the glass substrate. After coating, the excess solvent was removed by placing the sample on a heat-plate for several minutes. The thickness of the final absorber film was about 300 nm.

The linear transmission spectrum is shown in Figure 6.3a. The energy levels of the CNT ensemble are clearly identifiable as the valleys of stronger absorption. The valley around 1800 nm corresponds to the E_{11} transition and the valley around 1000 nm is related to the E_{22} transition (see also Figure 6.2). Below 800 nm, the absorption from metallic CNTs sets in. The broad absorption bandwidth is a result of the diameter distribution of the CNT ensemble, as discussed earlier. The linear absorption at the laser wavelength of 1074 nm was about 1 %. The nonlinear reflectivity was measured at a wavelength of 1088 nm, which was the shortest possible wavelength of the employed optical parametric oscillator (OPO). The duration of the pulses from the OPO source was about 200 fs. A modulation depth of 0.25 % and a saturation fluence of 11.4 µJ/cm^2 were obtained after fitting the model function (4.2) to the data (without the TPA term, see Figure 6.3b). The relaxation behaviour was determined in a pump-probe experiment similar to the

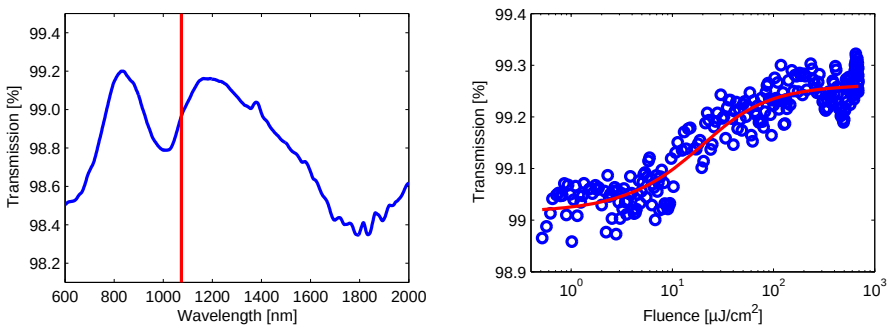

(a) (b)

Figure 6.3: (a) Linear and (b) nonlinear transmission of the CNTSA used for mode-locking the semiconductor disc laser. The red, vertical line in (a) indicates the wavelength of operation in the mode-locked laser experiment (i.e. 1074 nm), the nonlinear response was measured at a wavelength of 1088 nm.

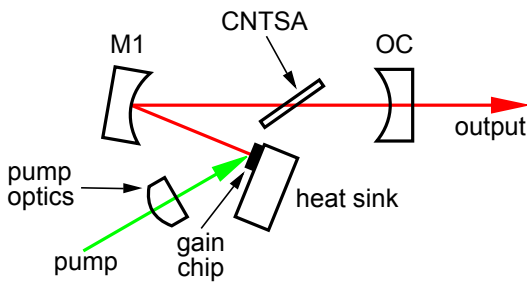

Figure 6.4: Cavity layout of the OPSDL. OC: outcoupling mirror with a radius of curvature of 50 mm and a transmission of 0.6 %. M1: high-reflective mirror ($R > 99.9$ %) with a radius of curvature of 100 mm. The gain chip was mounted on a water-cooled copper heat-sink. The saturable absorber (CNTSA) was placed at Brewster's angle at the waist between the two curved mirrors.

one described in Section 4.5. Fitting a bi-exponential function to the data revealed a fast relaxation component (intra-band) of 150 fs and a slower component (inter-band) of 1.1 ps.

Mode-locked OPSDL

The laser cavity in this experiment featured a simple V-type layout, with the gain chip at one end of the cavity and with an outcoupling mirror (OC) with a transmis-

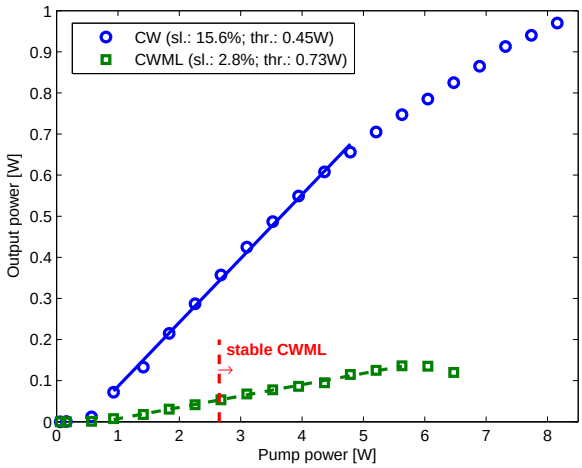

Figure 6.5: Efficiency of the OPSDL in CW operation (blue circles) and with the CNTSA in place (green squares). The slope efficiency and the threshold are obtained from linear fits and indicated by lines in the corresponding colour. The same outcoupling mirror ($T = 0.6\,\%$) was used for both measurements. The red, vertical line indicates the beginning of the region of stable CWML.

sion of 0.6 % at the other end. Both the folding mirror (M1) and the outcoupling mirror were curved, providing a focus in the cavity arm between them. The absorber was placed at Brewster's angle at this focal position. A schematic of the cavity layout is shown in Figure 6.4. The gain chip contained 3 InGaAs quantum wells and was optically pumped by a fibre-coupled laser diode, under an angle of $\approx 45\,^\circ$ and at a wavelength of 808 nm.

With the CNTSA in place, lasing started at a pump power of 730 mW and continued with a slope efficiency of 2.8 %. CWML started at an output power of about 50 mW (at a pump power of 2.6 W). Mode-locking was stable up to a maximum output power of 136 mW, at which point the output power would not increase any further, most likely due to the thermal limitations of the gain chip (see Figure 6.5). In any case, no damage was observed on the absorber. The laser mode size on the absorber was 75 µm, which resulted in a saturation parameter S_A of about 5 at the CWML threshold and around 18 at maximum output power. After removing the CNTSA from the cavity, the laser showed a threshold pump power of 450 mW and started with a slope efficiency of 15.6 %. Above a pump power of 5 W, the slope efficiency decreased, due to thermal effects in the gain chip. The considerable difference in the slope efficiencies of the CW and the CWML performance is explained by the fact that, although the loss in the absorber can be

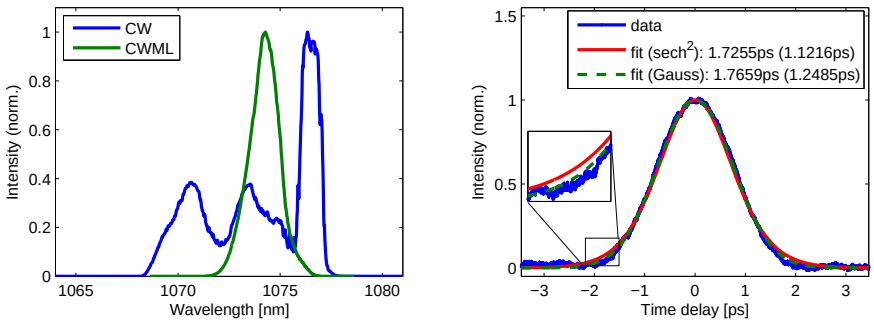

(a) (b)

Figure 6.6: (a) Optical spectra for CW and CWML operation. (b) Autocorrelation trace of the CNT mode-locked OPSDL and two fits, assuming sech^2-shaped (red, solid) and Gaussian-shaped (green, dashed) intensity profiles. The corresponding FWHM pulse durations are 1.12 ps and 1.24 ps, respectively. The inset shows a magnification of the trace's wing in order to emphasise the differences between the recorded signal and the two fit functions.

considered small, it was, nevertheless, larger than the outcoupling loss.

Optical spectra were recorded for the CW and the CWML operation and are presented in Figure 6.6a. The mode-locked operation was clearly visible by a profound change of the shape of the spectrum. The spectral bandwidth was 1.6 nm corresponding to a Fourier-limit of 760 fs. An intensity autocorrelation measurement revealed a real pulse duration of 1.12 ps (see Figure 6.6b). The longer pulse duration may be explained by the non-optimised, intra-cavity dispersion. Since the laser was passively mode-locked, a sech^2-shaped intensity profile was assumed. However, the agreement between the data and the corresponding fit is not optimal in the wings. Noting that the autocorrelation represents an average over many pulses, the measured shape also depends on the statistical distribution of the pulse durations resulting from any fluctuations [171, 172]. Fluctuations, then, are possibly the result of the limited noise-removal capabilities of the absorber, which is due to its small modulation depth of $\approx 0.25\,\%$.

Further verification of the mode-locked operation was obtained by measuring the RF spectrum with a fast photo-diode (bandwidth 3 GHz). A wide range scan, showing the frequency comb up to the fourth harmonic, as well as a closer view of the signal at the fundamental frequency are given in Figure 6.7. The noise background is located at about -50 dB relative to the peak of the signal at the fundamental repetition rate (see Figure 6.7b).

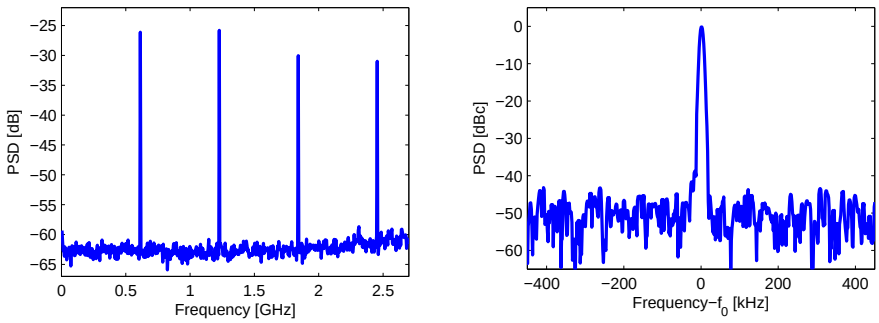

(a) (b)

Figure 6.7: RF spectra of the OPSDL mode-locked with a CNTSA. (a) Wide range spectrum showing higher harmonics. The resolution bandwidth is 3 MHz, the graph is an average of 100 single-shot measurements. (b) RF spectrum around the fundamental frequency, normalised to the carrier power. The resolution bandwidth is 3 kHz

External second-harmonic generation

Although the autocorrelation trace as well as the optical and RF spectra are strong indicators for mode-locking, caution should be exercised when assessing a new mode-locking technique. Strong mode-coupling in a CW laser might also yield a similar autocorrelation trace, although the signal level would then be very low, due to a drastically reduced conversion efficiency. In addition, the mode-beating among the laser modes would also result in an RF spectrum similar to that of the mode-locked case, albeit, in this case, the signal strength is expected to drop faster for the higher harmonics. These effects have been the subject of recent discussion, in particular in the case of OPSDLs, which seem to exhibit strong mode-coupling between neighbouring modes (see the results in [173] and the discussions in [174, 175]). A narrow bandwidth of the optical spectrum, in combination with a high repetition rate, then requires a particularly thorough examination.

To undoubtedly evaluate the quality of the mode-locking, external second-harmonic generation (SHG), using the laser's output, constitutes a simple, yet a rather convincing method[2]. Since the strength of the generated second-harmonic signal depends on the intensity of the fundamental input signal squared, the efficiency of the SHG process provides a strong response to any amplitude modulation of the input signal. Moreover, knowing the SHG crystals parameters, the conversion process can be simulated[3], using the measured average fundamental power as

[2] Any other nonlinear process might naturally serve the same purpose.

[3] In the analysis presented here, the free software package *SNLO* from AS-Photonics is used.

well as the assumed pulse width in order to obtain a prediction for the conversion efficiency.

The nonlinear medium, employed in the SHG experiment performed here, was a 5 mm long lithium triborate (LBO) crystal used in a type-I phase-matching arrangement. The output of the laser was focused to a spot size of 8.5 µm by a lens with a focal length of 25 mm. Assuming a pulse duration of 1.12 ps, a conversion efficiency of 11.3 % is predicted. The average input power was 136 mW, the obtained average SH power was measured to be 10.56 mW. Taking into account around 10 % loss for the second-harmonic signal due to the IR filter in front of the power meter, yields a measured conversion efficiency of 8.6 %. The result being close to the theoretical prediction, then, supports the notion that the laser emitted mode-locked pulses. For comparison, the CNTSA was replaced by a blank quartz plate, to obtain CW operation of the same laser. The conversion efficiency for CW radiation was, in this case, only ≈ 0.05 %, further emphasising that high peak-power pulses were obtained when using the CNTSA.

6.5 Summary

Saturable-absorber devices based on CNTs have been presented as a useful technology for mode-locking of lasers. The properties of CNTs and the fabrication of CNTSAs have been outlined. Mode-locking with a saturable absorber based on CNTs was demonstrated in an OPSDL, leading to pulses with a duration of 1.12 ps, at a repetition rate of 613 MHz, and with an average output power of 136 mW. In addition to measuring the autocorrelation and the RF spectrum of the laser output, the mode-locking was verified by an external SHG experiment. The properties of the CNTSA used in this experiment, namely low modulation depth and low saturation fluence, have been described. The absorber's low loss was a crucial factor for mode-locking the low-gain OPSDL, although further reduction of the non-saturable loss is desirable in order to improve the efficiency of the laser.

Chapter 7

Cascaded Mode-Locking

In this chapter, the concept of cascaded mode-locking is explored. First, an overview over the development of this method is presented. Following this, the underlying theoretical concepts are introduced, noting the similarities to Kerr-lens mode-locking, which has already been covered in Chapter 2. Subsequently, the technique is applied to a laser based on Yb:KYW as the gain medium, periodically-poled KTP (PPKTP) as the medium for the cascaded nonlinear interaction, and a volume Bragg grating for spectral control. The results are presented and then used to calculate the nonlinear phase as well as the effective nonlinear refractive index for this particular case. A summary is given at the end of the chapter.

7.1 Overview

The nonlinear phase shift imprinted on the fundamental wave during second-harmonic generation (SHG) was recognised early on [176]. However, the potential of this phenomenon was only emphasised later, when it became apparent that cascaded, second-order nonlinearities could be exploited to create third-order nonlinearities, larger than those directly obtained from available materials [76, 177]. The experimental demonstrations of large phase shifts imprinted on the fundamental wave during SHG, underlined this notion [75, 178]. A large third-order nonlinearity offers the benefit of a more relaxed demand on the spot-size in the nonlinear medium, which is of interest with regard to the material's damage threshold, but also with regard to the design of the laser cavity. Especially for mode-locking of low peak-power systems, i.e. picosecond or high-repetition rate sources, a stronger or even an engineered third-order nonlinearity would be beneficial. In general, this technique also offers to extend the principles of Kerr-lens mode-locking (KLM) to a wider range of lasers, as was mentioned in Chapter 2.

Cascading two second-order nonlinearities for mode-locking of a laser, so called *cascaded mode-locking* (CML), was first addressed by Stankov, with the introduc-

tion of the nonlinear mirror (NLM) technique [77]. To achieve an amplitude modulation of the fundamental wave, this technique combined a phase-matched second-order nonlinear medium with a dielectric mirror, that was partly reflective at the fundamental wavelength and highly reflective at the second harmonic (SH). The reflectivity of such a device is higher for higher intensities, because the energy that is stored as second-harmonic radiation experiences a smaller loss at the dielectric mirror than the fundamental radiation. In combination with subsequent back-conversion, this effectively constitutes a nonlinear response at the fundamental wavelength. The modulation strength of the NLM, thereby, depends on the conversion efficiency of the nonlinear medium, thus, emphasising that phase matching is crucial. On the other hand, the requirement for efficient phase matching, at the same time, limits the bandwidth and, subsequently, the achievable pulse duration[1]. In fact, the main focus so far has been on Nd-doped gain media, where also the gain bandwidth limits the pulse duration to a few picoseconds [179–182].

Some of these limitations can be circumvented by exploiting the real part of the cascaded nonlinearity. Instead of a direct amplitude modulation, a nonlinear phase modulation is used. Regular, third-order KLM can then be emulated by converting the nonlinear phase-shift into a loss modulation at an aperture, e.g. a pinhole, which is placed at a suitable position inside the laser cavity (so-called *hard* aperture). This has first been demonstrated in an Nd:YAG laser, which delivered pulses with a duration of 14 ps at an average output power of 500 mW [179]. A soft-aperture implementation has also been presented [180]. In this case, the aperture was realised by the interaction of the de-focusing Kerr-lens created by the cascaded, second-order nonlinearities and the thermal lens in the laser gain medium. Since the cavity had to be operated close to its stability limit, only a narrow window existed for mode-locked operation. Additional lasers, mode-locked with the CML technique, have been developed, with pulse durations on the order of 10 ps and with output powers of up to 15 W [181–184]. Especially in [182], it was argued that CML, as opposed to mode-locking with semiconductor saturable absorbers (SSAs), presents a promising solution for high-power lasers, since SSAs in this regime suffer from increased heat load and subsequent damage. A notable exception to the aforementioned demonstrations has been a KLM-operated Cr:Forsterite laser, delivering pulses with a duration of 60 fs, in a net-positive dispersive regime, assisted by a nonlinear phase shift, which was created in a nonlinear crystal [185].

An effective third-order nonlinearity has been achieved in a number of different nonlinear media. The above mentioned publications have used LBO (LiB_3O_5), KTP ($KTiOPO_4$), as well as PPKTP and PP-Mg:SLT (periodically-poled, Mg-doped stoichiometric $LiTaO_3$). Quasi-phase matched (QPM), periodically-poled materials, in particular, offer the advantage that they can be engineered for a specific application.

Because of the nonlinear loss from SHG in the nonlinear medium, a free-running

[1] While the conversion efficiency is proportional to the nonlinear medium's length, the acceptance bandwidth shows an inversely proportional dependence.

laser with sufficient bandwidth and with an intra-cavity SHG crystal will inevitably operate at wavelengths far away from the point of optimal phase-matching. Although a nonlinear phase-shift will be imprinted on the circulating signal in any case, control over the optimum phase mismatch, by tuning the nonlinearity, would remain difficult without any locking of the laser wavelength. While a small gain-bandwidth might provide a certain degree of control, this approach would limit the selection of the available gain media and, also, any possibility for a controlled wavelength tuning over a wider range. The solution for spectral control that is presented in this thesis is based on the use of a volume Bragg grating (VBG, see also Publication V). These devices have, mainly, been used for wavelength-stabilisation of CW and Q-switched lasers [186–188]. In the case of CML, however, the possibility of limiting the spectrum of a laser to a specific region enables the optimisation of the nonlinear phase-shift that is obtained from the effective third-order nonlinearity. The combination of engineered nonlinear materials and spectral control via a VBG, then, offers an increased flexibility for the development of lasers, mode-locked with a third-order nonlinearity.

7.2 Third-order nonlinearity from second-harmonic generation

In the following section, the theoretical basics of nonlinear phase modulation in an SHG process are briefly introduced. The presented concepts are later used in the analysis of the laser, which has been mode-locked by exploiting this effect, as was mentioned in the beginning of this chapter.

The evolution of the electric field during the SHG process can be described by a set of two coupled differential equations for the fundamental wave E_ω and the second-harmonic wave $E_{2\omega}$, both propagating through a nonlinear medium along the z-coordinate (see, e.g. [189]):

$$\frac{\partial E_\omega}{\partial z} = \mathrm{i}\frac{\omega d_{\mathrm{eff}}}{n_\omega c} E_{2\omega} E_\omega^* \exp\left(\mathrm{i}\Delta k z\right) , \tag{7.1a}$$

$$\frac{\partial E_{2\omega}}{\partial z} = \mathrm{i}\frac{\omega d_{\mathrm{eff}}}{n_{2\omega} c} E_\omega E_\omega \exp\left(-\mathrm{i}\Delta k z\right) . \tag{7.1b}$$

Here, the nonlinear medium's effective nonlinear coefficient is denoted as d_{eff}. The refractive indices n_ω and $n_{2\omega}$ and, consequently, also the wave-vector mismatch $\Delta k \equiv k_{2\omega} - 2k_\omega$ are temperature dependent [190–192]. In QPM materials, the wave-vector mismatch also includes a grating vector $k_{\mathrm{Q}} = 2\pi/\Lambda$, which is defined by the grating period Λ of the QPM crystal. The acquired nonlinear phase ϕ_{nl}, then, crucially depends on the total wave-vector mismatch. For a large mismatch, or at low intensities, the nonlinear phase follows approximately the relation $\phi_{\mathrm{nl}} \propto L/\Delta k$, where L is the length of the nonlinear crystal [75]. A more accurate solution, however, can be found by solving the coupled wave equations given above and extracting the phase of the fundamental wave from the result for E_ω.

The obtained value for the nonlinear phase can, in turn, be used to calculate an effective nonlinear refractive index n_2 according to Equation (2.6), which has been presented in the context of self-phase modulation (SPM) in Chapter 2. The equation is repeated here, although in a different arrangement:

$$n_2 I = \phi_{\mathrm{nl}} \frac{c}{\omega L} = \phi_{\mathrm{nl}} \frac{\lambda}{2\pi L} \ . \tag{7.2}$$

The nonlinear phase imprinted on the fundamental wave by two cascaded, second-order nonlinearities, then, indeed resembles a third-order nonlinearity.

Phase mismatched second-harmonic generation

Another useful expression that can be derived from the coupled wave equations (7.1), is the intensity $I_{2\omega}$ of the second-harmonic wave as a function of the wave-vector mismatch. Assuming a negligible depletion of the fundamental wave (i.e. $\partial E_\omega / \partial z \approx 0$), the integration of Equation (7.1b) yields (see, e.g. [193]):

$$I_{2\omega} \propto \mathrm{sinc}^2 \left(\frac{\Delta k L}{2} \right) \ . \tag{7.3}$$

By tuning the wave vector mismatch, e.g. by tuning the temperature of the QPM crystal, the intensity of the generated second-harmonic radiation follows a sinc^2 function. This relation reveals the existence of non-zero values for Δk, in which case the second-harmonic signal vanishes. For these cases of complete back-conversion, no amplitude modulation of the fundamental wave occurs, however, a nonlinear phase is, nevertheless, imprinted on the fundamental field, because of the fact that $\Delta k \neq 0$. This constitutes a pure phase modulation, as opposed to an amplitude modulation as in the case of the NLM technique.

7.3 Cascaded mode-locking of an Yb:KYW laser

In the following, the mode-locking of an Yb:KYW laser by cascaded, second-order nonlinearities in a PPKTP crystal is presented. The crystal was operated off from perfect phase-matching, in order to create a nonlinear phase shift at low conversion efficiency. The peak, on-axis, nonlinear phase of 0.16 rad resulted in an effective nonlinear refractive index of $2.33 \cdot 10^{-17}\,\mathrm{m^2/W}$, which, in combination with a hard aperture, provided the necessary modulation for mode-locking of the laser. The laser, then, emitted pulses with a duration of 16 ps, at a repetition rate of 210 MHz, and with an average output power of 690 mW. The experiment and its results are also presented in Publication V.

Laser setup

A schematic of the laser cavity is given in Figure 7.1. A 3 mm long, wedged Yb:KYW crystal was positioned close to one of the cavity ends. The gain medium

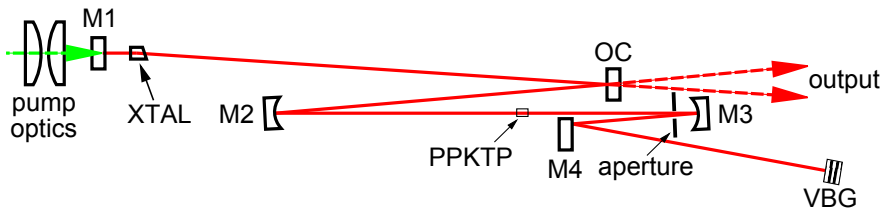

Figure 7.1: Cavity layout of the Yb:KYW laser, mode-locked by cascaded, second-order nonlinearities. M1: pump mirror, highly transmissive at the pump wavelength, highly reflective at the laser wavelength. OC: outcoupling mirror ($T = 5\,\%$). M2, M3: curved mirrors with radii of curvature of 150 mm and 100 mm, respectively. M4: high-reflective mirror. VBG: volume Bragg grating. PPTKP: periodically-poled KTP crystal. XTAL: Yb:KYW crystal with a 5 °-wedged end-facet.

was pumped by a fibre-coupled, wavelength-stabilised laser diode operating at a wavelength of 981 nm. The pump optics matched the pump mode-size to that of the laser (about 100 µm). An outcoupling mirror (OC) with a transmission of 5 % was placed in a folding position, which yielded two output beams (the total outcoupling loss was, thus, 10 %). The PPKTP crystal was 1.5 mm long and featured an aperture of $6 \times 1\,\mathrm{mm}^2$. It was anti-reflection coated for the fundamental as well as the second-harmonic wavelength. The QPM grating period was 7.99 µm and perfect phase-matching was achieved at a wavelength of 1029 nm and at a temperature of 80 °C. The nonlinear crystal was mounted on a copper block and the temperature could be controlled via a Peltier element. The temperature sensor was placed inside the heat-sink, between the Peltier element and the PPKTP crystal. The crystal itself was placed between the two curved mirrors, M2 and M3, which focused the laser mode in between them to a radius of 29 µm. Translation stages allowed moving the PPKTP crystal by 5 mm in all three dimensions, in particular, in and out of focus, and also allowed rotating the crystal. In this way, the spot-size inside the crystal could be adjusted between the minimum of 29 µm and up to about 55 µm. A 3 mm long VBG, with an aperture of $5 \times 5\,\mathrm{mm}^2$, was placed at the other cavity end for spectral control. Its peak reflectivity was measured in a separate experiment and determined to be 99.6 % at a wavelength of 1029.5 nm. The VBG's FWHM bandwidth was 0.32 nm. The VBG was anti-reflection coated at the laser wavelength. An iris aperture was placed close to one of the curved mirrors. It should be noted, though, that mode-locking could be achieved by placing the aperture in

front of either of the two curved mirrors. The whole laser cavity was built on a breadboard and enclosed by an aluminium housing with a polycarbonate lid for reducing disturbances caused by air flow.

Properties of the nonlinear crystal

The second-order nonlinearity of the PPKTP crystal was characterised by using the laser as shown in Figure 7.1, locked by the VBG, but without the aperture and the PPTKP crystal. The output of the CW laser was focused to a spot size of 33 µm and directed into the crystal, which was now placed outside the laser cavity. This resulted in 30 µW of second-harmonic power for an input power of 300 mW at the fundamental wavelength. The effective nonlinear coefficient d_{eff} was then calculated using the following relation (see, e.g. [193]):

$$P_{2\omega} = \frac{2\omega^2 d_{\text{eff}}^2 k_\omega}{\pi n_\omega^2 n_{2\omega} \varepsilon_0 c^3} P_\omega^2 L h \ . \tag{7.4}$$

In this equation, P_ω and $P_{2\omega}$ denote the fundamental and the second-harmonic power, respectively, the corresponding refractive indices are denoted by n_ω and $n_{2\omega}$, k_ω is the wave vector of the fundamental wave with frequency ω, and h is the Boyd-Kleinman factor, which takes into account the focusing conditions [194]. Using the above stated and measured values, the PPKTP's effective nonlinear coefficient d_{eff} was calculated to be about 9 pm/V, which is close to the typically reported values of about 10–12 pm/V [193].

The temperature tuning curve was measured in the same configuration as was used to perform the SHG experiment described above. The SH power was measured as a function of the signal voltage from the temperature sensor. The result is presented in Figure 7.2. The figure also includes a fit to a sinc^2 function, according to Equation (7.4). The FWHM temperature tuning bandwidth was then calculated to be 23.05 °C. The working point for CML was located at 54.5 °C, i.e. close to a minimum of the tuning curve.

Laser experiments

The slope efficiency and the lasing threshold were measured for various cavity configurations (see Figure 7.3). The cavity, with the wavelength locked at 1029 nm by the VBG, but without the PPKTP or aperture, had a threshold of 5.06 W of pump power and a slope efficiency of 47.5 % (blue circles). When replacing the VBG with a high-reflective mirror and inserting the PPKTP crystal (at a temperature of 54.5 °C) into the cavity, the lasing threshold remained approximately the same (green squares). However, the laser wavelength shifted to 1030 nm at threshold and towards 1035 nm upon increasing the pump power. For lasing at 1030 nm, and at 1035 nm, the phase-matching temperature of the PPKTP crystal would be 105 °C and 190 °C, respectively. By increasing the pump power, the gain was increased

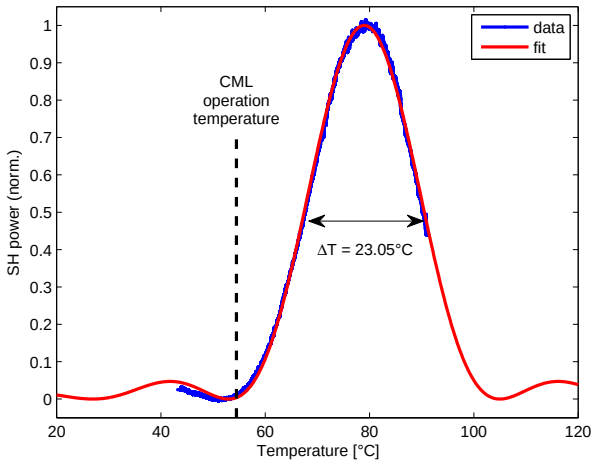

Figure 7.2: Temperature tuning curve of the PPKTP crystal. A sinc^2-function (red line) is fitted to the data (blue line). The FWHM tuning bandwidth is 23.05 °C. The temperature used for CML is indicated by the dashed, vertical line.

and the loss had to change accordingly. The wavelength, thus, shifted to a different point of the PPKTP's wavelength tuning curve, which, in turn, changed the loss from the SHG. The slope efficiency in this case was 31.8 %, i.e. smaller than in the previous configuration, due to the additional losses from the remaining SHG. The above mentioned observation highlights that CML in Yb:KYW would be difficult to achieve without preventing a shift of the wavelength by spectral locking. With the VBG in place to lock the wavelength and the PPKTP inside the cavity, operated at the correct temperature for CML, the threshold increased to 8.28 W and the slope efficiency reduced to 27.8 % (black triangles). The lower slope efficiency, as compared to the cavity with the high reflector instead of the VBG, is explained by the larger SH losses from an incomplete back-conversion. The narrow bandwidth of the VBG, now, prevented shifting of the wavelength for compensating this loss.

To achieve CML, an aperture was inserted in front of one of the curved mirrors, where the absolute change in mode-size was largest. The combination of a cascaded Kerr-lens and an aperture bears similarity to a z-scan setup [195]. In analogy to that, the modulation depth obtained from this arrangement can be controlled by the size of the aperture. In the configuration presented here, self-starting CML was accomplished at a pump power of 11.5 W, by introducing an aperture loss of 2–3 % and with careful alignment of the PPKTP's position. The threshold power of the laser, in this arrangement, was slightly higher (8.88 W) and the slope efficiency slightly lower (25.6 %, red triangles), as compared to the cavity with an open aper-

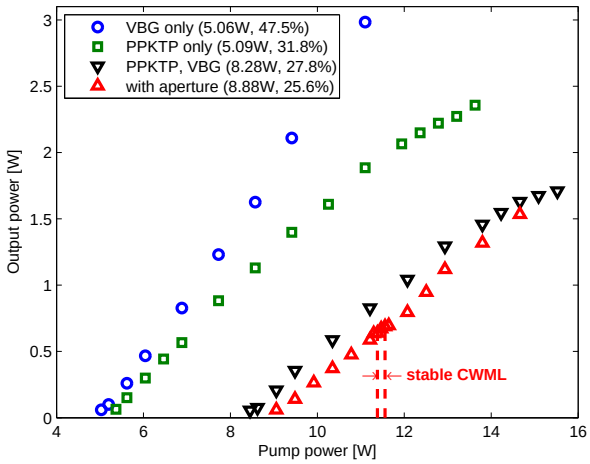

Figure 7.3: Output power as a function of incident pump power for various cavity configurations: with VBG, but without PPKTP (blue circles); with PPKTP and a high-reflective mirror instead of the VBG (green squares); with PPKTP and VBG, but without aperture (black triangles pointing down); with PPKTP, VBG and aligned aperture (red triangles pointing up). The red, vertical lines indicate the regime of stable mode-locking for the last configuration. Threshold and slope efficiencies for each configuration are listed in the legend.

ture. Stable CML could, in general, be achieved at different pump powers between 10.5 W and 14 W. However, the aperture size had to be realigned for every specific pump power, in order to compensate for the varying contribution of the thermal lensing in the laser crystal.

Optical spectra of the CML cavity were recorded at several pump powers and are shown in Figure 7.4a. When mode-locked, the spectrum was centred at a wavelength of 1029.1 nm and had an FWHM bandwidth of 85 pm (frequency bandwidth of 24 GHz), corresponding to a Fourier-limited pulse duration of 13 ps. An intensity autocorrelation trace is shown in Figure 7.4b. Assuming a sech^2-shaped intensity profile, the FWHM pulse duration is found to be around 16 ps. The intra-cavity peak power, in this case, was estimated at 1.98 kW and the pulse energy, emitted at each of the two outputs, was 1.6 nJ, i.e. a total output pulse energy of 3.2 nJ was thus obtained.

Far away from the mode-locking working point, at low pump power levels, the centre of the spectrum was located at a slightly lower wavelength of 1029.03 nm. Upon approaching the working point, instabilities in the optical spectra were observed. The spectrum started to shift to slightly longer wavelengths, eventually

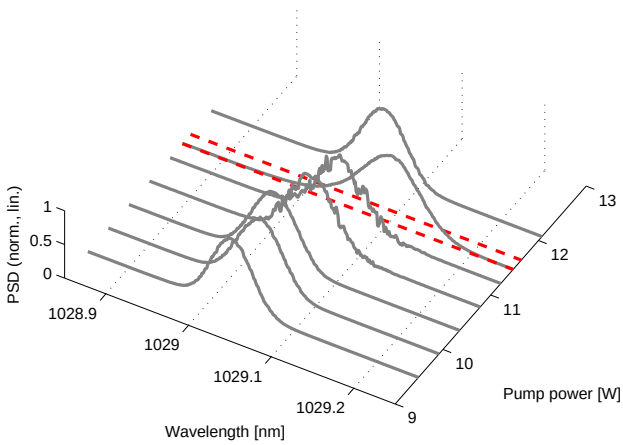

(a)

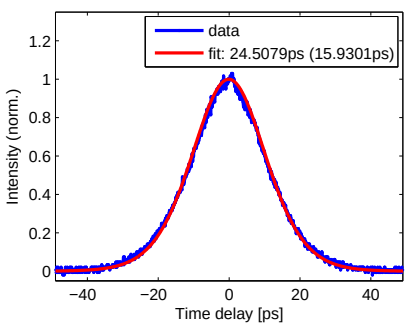

(b)

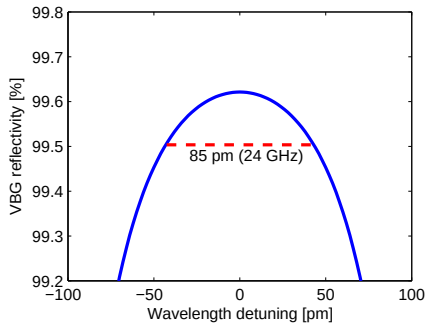

(c)

Figure 7.4: (a) Optical spectra of the CML laser at various pump powers. The region of stable mode-locking is indicated by the dashed, red lines. In this region, the centre wavelength was 1029.1 nm, whereas the wavelength was shifted to 1029.03 nm when the laser was not mode-locked. The resolution bandwidth is 0.06 nm. (b) Autocorrelation trace of the CML laser (blue line) and a fit assuming a sech^2-shaped (red line) intensity profile. (c) Simulation of the VBG's reflectivity as a function of the detuning from the centre wavelength. The FWHM bandwidth of the mode-locked optical spectrum is indicated by the dashed, horizontal line.

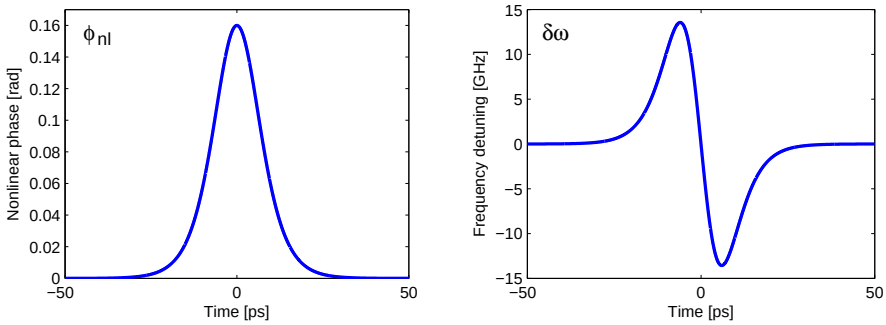

(a) (b)

Figure 7.5: (a) Simulated nonlinear phase and (b) frequency modulation at the CML working point, as a function of time.

reaching 1029.1 nm, when mode-locking started. When increasing the pump power even further, mode-locking ceased again and the optical spectrum shifted back to the initial value. The change in the optical spectrum is, likely, the result of an altered gain-loss dynamic in the case of mode-locking. For the given laser-crystal cut and output polarisation, the gain is slightly larger on the short wavelength side. When the laser is mode-locked, the loss at the aperture is reduced and, for a given population inversion, the wavelength shifts to longer values within the VBG's reflectivity curve. If the centre wavelength is assumed to be the peak reflectivity wavelength of the VBG, then the VBG's reflectivity is still above 99.5 % within this bandwidth. This is illustrated in Figure 7.4c, showing a simulation of the VBG's reflectivity curve, based on the measured peak reflectivity of 99.6 % and a grating length of 3 mm (see Appendix A.2).

Strength of the nonlinear interaction

Using the results presented above, the coupled wave-equations (7.1) can be used to calculate the nonlinear phase which is imprinted on the fundamental wave by the cascaded, second-order nonlinearities. For an input signal with a peak intensity of 1.98 kW, the peak, on-axis, nonlinear phase change is found to be $\hat{\phi}_{\mathrm{nl}} = 0.16\,\mathrm{rad}$. The corresponding total index change Δn for the given peak intensity is then calculated to be $\Delta n = n_2 I_{\mathrm{p}} = 1.75 \cdot 10^{-5}$ (see Equation (7.2)). This result, in turn, yields an effective nonlinear refractive index of $n_2 = 2.33 \cdot 10^{-17}\,\mathrm{m^2/W}$. Figure 7.5a shows the simulated nonlinear phase as a function of time, assuming a sech^2-shaped pulse with the pulse duration and the peak intensity as determined above. The frequency modulation $\delta\omega/2\pi$ (relative to the optical carrier frequency), created by the phase modulation, can thus be obtained from the nonlinear phase via the

expression $\partial\phi_{\mathrm{nl}}/\partial t$. The result is shown in Figure 7.5b and reveals a modulation bandwidth of 27 GHz, which is in good agreement with the measured FWHM of 24 GHz of the optical spectrum.

The knowledge of the nonlinear phase allows to estimate the modulation strength which is imposed onto the circulating signal by the aperture. The relation between the aperture transmission and the nonlinear action is known from the z-scan technique [196]. In a z-scan experiment, the relative transmission through an aperture is measured as a function of the position of the nonlinear medium relative to the focus of the input beam. The resulting curve shows a characteristic response, with a minimum and a maximum transmission. For small aperture losses and small phase deviations (i.e. $\phi_{\mathrm{nl}} < \pi$), the difference between the maximum and the minimum transmission, the peak-to-valley[2] transmission T_{pv}, can be estimated by the following equation (see [196]):

$$T_{\mathrm{pv}} \approx 0.406 \cdot (1 - T_{\mathrm{ap}})^{0.25} \, |\hat{\phi}_{\mathrm{nl}}| \; . \tag{7.5}$$

Here, the aperture is characterised by its linear transmission T_{ap}. Assuming an aperture loss of 2 %, as mentioned above, a peak-to-valley transmission of 2.4 % is calculated from Equation (7.5). Given the assumptions made for Equation (7.5), this result implies a transmission[3] of 1.2 %, in the case that the nonlinear crystal is placed at a distance of $0.86 \cdot z_0$ away from the focus (where z_0 denotes the Rayleigh range).

Mode-locking stability

A wide-range RF scan of the output signal, showing up to the ninth harmonic, is presented in Figure 7.6a and this result further verifies stable CWML. The single sideband spectrum of the fundamental repetition frequency is given in Figure 7.6b. The pedestal at -60 dB, relative to the carrier, is attributed to fluctuations from the convection of air, caused by the heat-sink, which was used for controlling the temperature of the PPKTP crystal. The cut-off frequency of about 80 kHz, then, corresponds to the relaxation oscillation resonance at this pumping rate. To assess the long-term stability, the fundamental repetition rate was logged over a period on the order of 30 min (see Figure 7.7). The recorded data reveals a frequency drift, which is attributed to thermal changes, namely the heating by the PPKTP's heat-sink, located inside the laser's housing. The mode-locking was occasionally interrupted, but resumed briefly afterwards and without further external action. The absolute drift of the repetition rate, in the given time window, was on the order of a few kilohertz, which corresponds to a refractive index change on the order of 10^{-5}, which, in turn, is equivalent to a change of the optical path length on the

[2] Depending on the sign of the nonlinearity, the order in which maximum and minimum occur during the scan might be reversed.

[3] Since the transmission curve is not necessarily symmetric, the half-value of the peak-to-valley transmission is only an approximation.

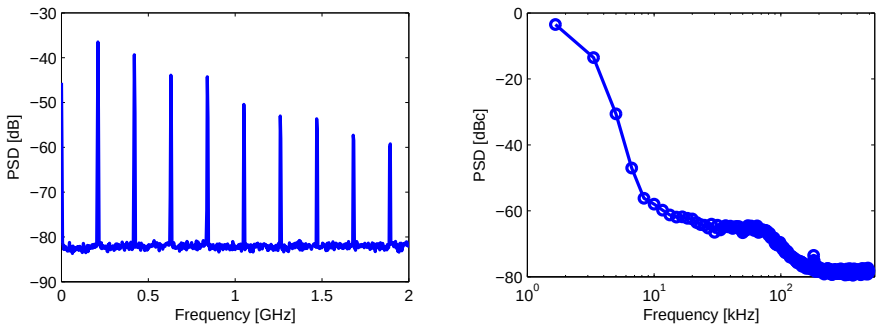

(a) (b)

Figure 7.6: RF spectra of the cascaded mode-locked laser. (a) Wide-range RF spectrum. The resolution bandwidth is 3 MHz. (b) Single-sideband spectrum of the fundamental frequency, normalised with respect to the carrier power. The resolution bandwidth is 3 kHz. Both traces are averages over 100 single-shot measurements.

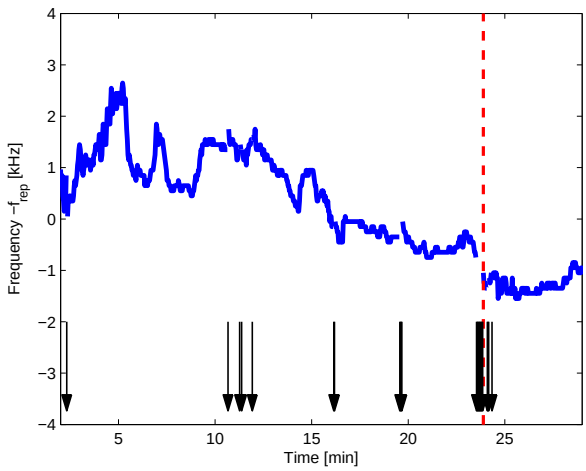

Figure 7.7: Drift of the repetition rate over time. The time axis is relative to switching on of the pump laser. The pump power was kept constant until $t = 24$ min (indicated by a dashed, red vertical line). At this point, mode-locking ceased, but could be re-initiated by increasing the pump power. Occasional interruptions in the mode-locking are indicated by black arrows at the bottom of the graph.

order of 10 µm. In addition to the repetition rate, also the output power decreased. Since the stability of CML depends on the modulation amplitude of the nonlinear index, stable mode-locking would become increasingly difficult, if the index change from, e.g. thermal effects, grew larger than that of the nonlinear index modulation. Considering the above calculated, total index change of $\Delta n = 1.75 \cdot 10^{-5}$, a variation of 1 °C in the PPKTP crystal would be sufficient to change the refractive index of the material by the same order of magnitude [192]. It is therefore concluded that, although stable mode-locking was achieved in a non-stabilised configuration, the overall performance and stability could be further improved by an optimised thermal management.

7.4 Summary

Cascaded mode-locking of a broad gain-bandwidth medium has been demonstrated. The nonlinear phase imprinted on the fundamental wave during SHG in a PPKTP crystal was translated into an amplitude modulation by using a hard aperture inside the laser cavity, as in regular KLM. It was observed that control of the laser's optical spectrum is crucial in order to adjust the nonlinear interaction for successful mode-locking. A mode-locked pulse train, with a repetition rate of 210 MHz and an average output power of 690 mW, was obtained. The pulse duration was measured to be about 16 ps, which was close to the Fourier-limit. A volume Bragg grating (VBG) enabled control over the optical spectrum in two ways: first, the wavelength was fixed; second, the bandwidth of the VBG limited the bandwidth of the nonlinear phase modulation, thereby determining the pulse duration. The effective, nonlinear refractive index has been calculated to be $2.33 \cdot 10^{-17}\,\mathrm{m}^2/\mathrm{W}$. It should be noted that this value is about two orders of magnitude larger than the value of the nonlinear refractive index of $1 \cdot 10^{-19}\,\mathrm{m}^2/\mathrm{W}$ in Yb:KYW [197]. This observation emphasises the potential of employing cascaded, second-order nonlinearities as a substitute for (or complement to) the weak, intrinsic third-order nonlinearity of the gain medium itself.

Although the nonlinear index modulation proved to be sufficient for self-starting and sustained CML under non-stabilised conditions, (e.g. convective cooling of the top of the PPKTP crystal) the stability could be improved further by, e.g. ensuring a more homogeneous temperature distribution inside the nonlinear crystal. While the working range for a specific configuration appeared to be limited, it was found that mode-locking at different output powers was possible by adjusting the position of the nonlinear crystal as well as the transmission of the aperture, thus controlling the modulation depth. To increase the operational range of the laser, an electrically controlled mechanism might be developed, in order to tune these parameters as a function of the pump power. To further improve the stability of the laser system, the output power might be subject to a stabilisation technique by similar means. Furthermore, the temperature control of the PPKTP crystal offers a potential for optimisation.

Chapter 8

Conclusion

In this thesis, I presented a number of solid-state lasers, which were mode-locked by employing several novel concepts, namely, semiconductor quantum dots, and carbon nanotubes as saturable absorbers, as well as nonlinear phase modulation from cascaded second-order nonlinearities.

I examined a set of eight QDSAs, with controlled variations in their structural design, and characterised all of the samples with respect to their nonlinear and transient response as well as their second-order dispersion (see Publications I and II, as well as Chapter 4). The nonlinear reflectivity measurements revealed modulation depths ranging from 0.18 % to 2.9 % and low saturation fluences on the order of 1–10 µJ/cm^2. I demonstrated that the saturation fluence and the modulation depth in QD-based, saturable absorbers are, to a certain degree, decoupled, since the saturation fluence is mainly determined by the structural design rather than by the number of QDs. I performed pump-probe experiments in order to confirm an initial, ultra-fast relaxation on a sub-picosecond time scale. In addition, I conducted time-resolved photoluminescence (PL) spectroscopy to examine the long-living component that had been observed in the pump-probe experiments. Given these findings, I concluded that the defect management and the interaction with the wetting layer play an important role in the relaxation dynamics of these QDSAs. The non-saturable losses were roughly on the order of the modulation depth for all of the samples but one, which, in turn, featured a relatively large non-saturable loss. However, it offered exceptionally fast relaxation times, which could not be resolved with the current experimental setup.

I successfully employed the characterised QDSA samples for mode-locking of three diode-pumped, solid-state lasers (see Chapter 5). All of these lasers were based on Yb:KYW crystals as the gain medium, delivered picosecond pulses, operated in the spectral region of 1020–1040 nm, and featured output powers between 100 mW and 13 W. In particular, by mode-locking one of the lasers at a repetition rate of 1.036 GHz, I showed that QDSAs present a suitable technology for

mode-locking of low pulse energy, solid-state lasers (see Publication III). I further demonstrated the versatility of QDSAs by mode-locking of an Yb-thin-disc laser with an output power of several watts. This experiment also allowed to assess the damage threshold of the QDSAs. All but one of the samples were shown to withstand fluences of up to $2.4\,\mathrm{mJ/cm^2}$, without damage. The damage threshold of the sample used for mode-locking of the 1 GHz laser was determined from the corresponding laser experiment and found to be about $860\,\mu\mathrm{J/cm^2}$. This was explained by additional defects in this particular structure, which also could explain the fast and efficient recombination that was observed in the pump-probe and PL experiments.

I demonstrated mode-locking of an optically-pumped semiconductor disc-laser (OPSDL) with a saturable absorber based on carbon nanotubes (CNTs, see Publication IV, as well as Chapter 6). The low gain in OPSDLs requires a low-loss absorber and it was shown that CNTs present a suitable solution. The laser delivered pulses with a duration of 1.12 ps, at a repetition rate of 613 MHz, and at an average output power of 136 mW. This was the first demonstration of an OPSDL mode-locked with CNTs.

Finally, I presented cascaded mode-locking (CML) of a laser based on a broad gain-bandwidth medium (see Publication V, as well as Chapter 7). The nonlinear phase, imprinted on the fundamental wave during SHG in a PPKTP crystal, was translated into an amplitude modulation by using a hard aperture inside the laser cavity, as in regular Kerr-lens mode-locking (KLM). It was observed that control of the optical spectrum of the laser is crucial, in order to adjust the nonlinear interaction for successful mode-locking. A mode-locked pulse train with a repetition rate of 210 MHz, at an average output power of 690 mW was thus obtained. The pulse duration was measured to be 16 ps, which was close to the Fourier-limit. A volume Bragg grating (VBG) enabled control over the laser's optical spectrum in two ways: first, the wavelength was fixed; second, the bandwidth of the VBG limited the bandwidth of the nonlinear phase modulation, thereby determining the pulse duration. The effective, nonlinear refractive index has been calculated to be $2.33 \cdot 10^{-17}\,\mathrm{m^2/W}$. This value is two orders of magnitude larger than that of the intrinsic, nonlinear refractive index of the material Yb:KYW.

8.1 Outlook

Applying the demonstrated mode-locking techniques to other wavelength regions would be interesting. In particular, the demonstrated CML technique could be used for mode-locking of lasers in the 2 µm region, where VBGs still show low absorption and where quasi-phase matched (QPM) nonlinear crystals are readily available. Also, CNTs present a viable solution for mode-locked lasers in this region, as has been recently demonstrated [198, 199].

QDSAs deserve a further examination; in particular, the influence of defects should be investigated in a systematic way, in order to optimise the trade-off be-

tween the non-saturable loss and the fast relaxation.

Regarding CNTSAs, optimisation should continue in order to reach watt-level output powers from DPSSLs and to evaluate the high-power performance of these absorbers. Semiconductor SAs have been shown to mode-lock high-power disc lasers [139], and the CNTSAs' potential in this respect should be further investigated as well. Finally, the direct incorporation of CNTs into glass [200, 201] appears to be a promising technology for mode-locking of monolithic lasers at very high repetition rates.

Although spectral control of lasers with a VBG is a well studied area [188], controlling the optical spectrum of a mode-locked laser in this way has only been explored with fibre Bragg-gratings in fibre lasers (e.g. in [202]), but not in DPSSLs. This is not restricted to CML lasers, as presented in this thesis, but might also be applied to saturable absorber mode-locked lasers in general. With respect to wide gain-bandwidth lasers, wavelength tuning might be explored, either by temperature tuning the VBG or by using a transversely chirped VBG. Longitudinally chirped VBGs might then be used to realise a larger bandwidth, thereby targeting sub-picosecond pulse durations.

Considering applications, it would be interesting to amplify the presented lasers in a simple Yb-fibre amplifier setup, in order to obtain high average-power picosecond pulses for nonlinear optics experiments, such as coherent anti-Stokes Raman spectroscopy or various other frequency conversion schemes. The limited bandwidth of such picosecond pulses, as compared to femtosecond pulses, meets the usual bandwidth limitations of these processes.

Appendix A

Basic Concepts

A.1 Experimental verification of CW mode-locking

This section describes how CW mode-locking (CWML) can be verified. Four basic experimental methods are described, two in the time domain and two in the frequency domain. These methods have been used in the experiments described in Chapters 5, 6 and 7.

Oscilloscope

The most straightforward way of monitoring a laser's output is by detecting it with a photo-diode and displaying the resulting photo-voltage on an oscilloscope. This procedure, however, has serious limitations as a result of the characteristics of mode-locked laser pulses: first, the pulse duration is usually considerably shorter than the response time, i.e. the dynamics of the signal usually exceed the bandwidth of the photo-diode. Available photo-diodes have rise-times on the order of 10 ps and bandwidths of several 10 GHz, which is already insufficient considering few-picosecond pulse durations, or even femtosecond pulses. Second, the large peak-power might saturate the diode, further distorting the measured signal. Nevertheless, the bandwidth is usually sufficient to determine the repetition rate. Furthermore, an oscilloscope trace suffices for a qualitative examination. A mode-locked laser will produce a periodic photo-diode signal and, if the round-trip time is large compared to the diode's relaxation time, the signal will be fully modulated. Thus, a constant (DC) background on the oscilloscope trace points towards a CW background from the laser and towards a non-optimal mode-locking. In addition, Q-switching instabilities are clearly visible as modulations on a much longer time scale than that of the pulse duration and are easily identified. Signals with equal amplitude and a spacing corresponding to the round-trip time, on the other hand, indicate clean CWML.

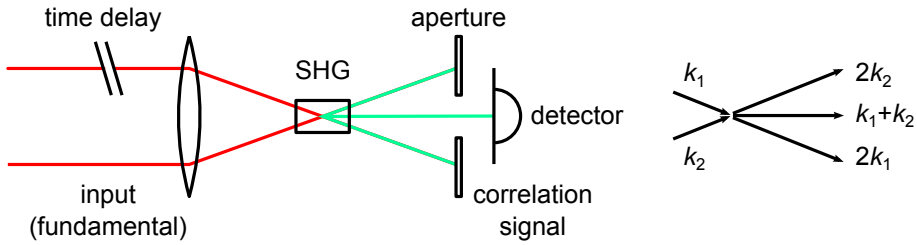

Figure A.1: Principle of an intensity autocorrelation. The input signal is split in two parts (not shown) of which one part is subject to a time delay. The two beams are combined in a nonlinear crystal for SHG. Three possible combinations of the wavevectors from the two input beams result in three output beams, as shown in the k-vector diagram on the right. The central beam contains the relevant information.

Care has to be taken, though, when interpreting slow modulations since these can also be the result of sampling (aliasing) effects in the digital oscilloscope.

Autocorrelation

Since pulses from mode-locked lasers are among the shortest signals that exist today, they are themselves used to accurately measure events occurring on short timescales. Also, a laser pulse can be used to measure itself by correlating it with a copy of itself. This technique is know as autocorrelation and is widely used in various implementations as a method for quantitatively measuring the pulse duration of mode-locked lasers and also to gain information on the pulse shape. The procedure consists in splitting a laser pulse-train into two beams, whereof one experiences a variable delay before both beams are re-combined for second-harmonic generation (SHG) in a nonlinear crystal. Since the intensity of the created second-harmonic signal depends on the input intensity, the generated signal will be a function of the delay between the two beams and will also be dependent on the pulse shape. The simplest implementation of this is the *intensity autocorrelation*, in which the two separated beams are re-combined in a non-collinear geometry, yielding second-harmonic radiation in the direction of the respective beams but also in the direction in between the two beams as a result of SHG involving a photon from each of the beams (compare with Figure A.1). The obtained autocorrelation signal $\mathcal{A}_{\mathrm{ac}}$ then follows as a function of the pulse shape $I(t)$ and the delay $\Delta\tau$:

$$\mathcal{A}_{\mathrm{ac}}(\Delta\tau) \propto \int_{-\infty}^{\infty} I(t)I(t-\Delta\tau)\,\mathrm{d}t\ . \tag{A.1}$$

The background terms are omitted in this equation since these contributions are usually removed by a spatial filter to yield a so-called *background-free* intensity autocorrelation. The variation of this signal only depends on the variation of the delay

which can be set to occur on time scales easily accessible by regular photo diodes. Notably, the autocorrelation signal is necessarily symmetric even if the input signal is asymmetric and, thus, an asymmetric autocorrelation trace points towards a misaligned measurement setup. Also, care has to be taken when selecting the nonlinear crystal since it has to support the laser's spectral bandwidth, otherwise pulses will appear longer than they really are.

To calculate the actual pulse duration from the measured signal, the original pulse shape has to be known. In the case of passively mode-locked lasers, the pulse shape in terms of intensity usually follows a sech^2-function[1]. The autocorrelation signal according to Equation (A.1) of a sech^2-shaped signal is given by [203]:

$$\mathcal{A}_{\mathrm{ac}}^{\mathrm{sech}^2} \propto \frac{3\Delta\tau\cosh(\Delta\tau) - \sinh(\Delta\tau)}{\sinh^3(\Delta\tau)} \ . \tag{A.2}$$

This function can then be fitted to the measured data in order to validate the assumption regarding the pulse shape and also to obtain the pulse duration. The pulses' FWHM (full width at half maximum) τ_{p} can also be easily calculated from the FWHM of the autocorrelation τ_{ac} via the following relation:

$$\frac{\tau_{\mathrm{p}}}{\tau_{\mathrm{ac}}} \approx 0.648 \ . \tag{A.3}$$

As is evident from Equation (A.1), all phase information is lost when measuring the intensity autocorrelation. However, more elaborate techniques, such as FROG and SPIDER, allow partial or even full reconstruction of the phase of the input signal [27, 204]. Nevertheless, the intensity autocorrelation trace provides valuable information about the mode-locking of a laser in terms of its pulse duration and pulse shape. Regarding the quality of the mode-locking, this measurement can also identify a CW component. Since the signal from the pulses is expected to be background free, any measured background indicates that the laser is running in a continuous mode. If the laser runs completely CW, the autocorrelation trace will show a large background with a small peak at zero delay and with a width corresponding to the laser's coherence length. Any Q-switching will appear as a modulation of the autocorrelation trace due to the averaging effect from the slow detection.

Optical spectrum

The transition between CW and mode-locked operation of a laser is usually clearly visible in the optical spectrum. Because the modes in a CW laser compete for the available gain, only a small number of them will ultimately prevail in equilibrium and, hence, the CW spectrum will be relatively narrow. In a mode-locked laser, on

[1] This follows from the analytic solution of the master equation (2.1) and is in most cases a very good assumption. Exceptions are multiple pulses and pulses that have been subject to strong higher-order dispersion.

the other hand, the modulation mechanism re-distributes energy between the modes by creating side-bands so that the optical spectrum can be substantially wider. The transition between the two modes of operation can thus lead to a dramatic increase in bandwidth, clearly visible on an optical spectrometer.

Also, the shape of the optical spectrum offers information. Since the optical spectrum is the Fourier-transform of the time-domain signal, the spectrum assumes a specific shape depending on the pulse shape. In particular, the optical spectrum of an unchirped sech^2-shaped pulse will also be sech^2-shaped [205].

Radio-frequency spectrum

A wealth of information about the quality of the mode-locking in a laser can be obtained by directing the laser output onto a photo-diode and measuring the RF spectrum. The carrier frequency (for optical signals on the order of 100 THz) is removed and the frequency spectrum is obtained around 0 Hz, i.e. in the radio frequency range. The bandwidth of the RF spectrum is, in principle, the same as that of the spectrum obtained with an optical spectrum analyser and, therefor, also given by the pulse duration. However, this bandwidth is on the order of terahertz, which is considerably more than the bandwidth of a typical photo-diode. Nevertheless, the diode's bandwidth is typically sufficient to measure a part of the frequency comb formed by the signal at the repetition rate (also the longitudinal mode-spacing) and its higher harmonics. Any additional modulation will now manifest itself as side-bands of this comb's peaks[2].

In this representation, Q-switching is easily distinguished from CWML as it creates strong sidebands. Q-switching can then also be interpreted as a very regular amplitude noise. CWML is characterised by the frequency comb being made of single peaks (at least in passively mode-locked systems). The width of the peaks is a measure of the timing jitter; however, care has to be taken as to select a suitable resolution bandwidth. Additional signals in the flanks of the peaks point towards further instabilities and can have various reasons, most often relaxation oscillations, which are especially prominent in gain-media with long life-times.

For a highly coherent CW laser, an RF spectrum similar to that of a CW mode-locked laser is measured; however, the amplitudes of the harmonics drop faster than in the case of the mode-locked frequency comb as a result of not having fixed the phase relation between the modes in the optical spectrum. A stable frequency comb with the fundamental and the harmonics being of comparable amplitude is a strong indicator for successful mode-locking. Side-bands of this comb in the range of kilohertz to megahertz, then, indicate additional amplitude modulation instabilities.

[2]The comb itself is also the sum of side-bands created by the amplitude modulation as defined by the pulse train.

A.2 Optical components with periodic refractive-index modulation

Optical materials with a periodically-modulated refractive index behave rather differently compared to bulk materials. This is a result of interference effects between the various reflected and transmitted electric-field components created by the multitude of interfaces. The magnitude of the reflected and the transmitted fields as well as their phases can be tailored by engineering the index modulation. Two approaches are generally available: one comprises starting out from the bulk material and locally changing the refractive index by suitable means. This is done, e.g. when fabricating volume Bragg gratings by illuminating photosensitive glass with an optical standing-wave pattern. The other approach consists of combining layers of two materials with different refractive indices into a sandwiched structure. This approach is used to obtain multi-layer dielectric coatings, typically on glass substrates in order to fabricate mirrors for optics applications. The same applies to varying the material or the material composition during the deposition of semiconductors. To obtain a structure that is highly reflective at a wavelength λ, the optical length of a single layer with a specific refractive index has to be $\lambda/4$. Constructive interference of the reflections from all of the resulting interfaces then yields a high reflectivity. The stack's resulting reflectivity R is mainly dependant on the refractive index contrast, i.e. $n_{\mathrm{lo}}/n_{\mathrm{hi}}$, of the alternating layer materials and the number of layer pairs N [206]:

$$R \approx 1 - 4n_0 n_{\mathrm{subs}} \frac{n_{\mathrm{lo}}^{2N}}{n_{\mathrm{hi}}^{2(N+1)}} \ . \tag{A.4}$$

Here, n_0 and n_{subs} denote the refractive index of the interface medium and of the substrate, respectively. The approximation holds for commonly used configurations with more than 10 layers and a suitably large index ratio.

Volume Bragg gratings

Volume Bragg gratings (VBGs) are optical components comprising a bulk material (typically glass), in which the optical properties are periodically altered so as to engineer its reflective and transmissive behaviour. This results in a periodic modulation with a magnitude δn around the base index n_0 in the direction of propagation (here z):

$$n(z) = n_0 + \delta n \cdot f(z) \ . \tag{A.5}$$

Since the modulation is usually created by exposing the material to an interference pattern, the modulation function $f(z)$ is a sinusoidal function. The modulation of the refractive index can be on the order of up to $\delta n = 10^{-3}$, but is typically less than that. The principal behaviour is characterised by the overall length d of the

material and the modulation period Λ [188]:

$$R_{\mathrm{VBG}}(\lambda) = \frac{\sinh^2\left(\frac{\pi d}{\lambda}\sqrt{\delta n^2 - (\frac{\lambda}{\Lambda} - 2n_0)^2}\right)}{\cosh^2\left(\frac{\pi d}{\lambda}\sqrt{\delta n^2 - (\frac{\lambda}{\Lambda} - 2n_0)^2}\right) - \delta n^2(\frac{\lambda}{\Lambda} - 2n_0)^2} \ . \tag{A.6}$$

In particular, the maximum reflectivity $\hat{R}_{\mathrm{VBG}}$ is obtained for $\lambda/\Lambda = 2n_0$, i.e. when the incident wavelength matches the design wavelength:

$$\hat{R}_{\mathrm{VBG}} = \tanh^2\left(\frac{\pi d}{\lambda} \cdot \delta n\right) \ . \tag{A.7}$$

It follows, then, that by measuring the peak reflectivity and the length of the VBG, the index modulation can be calculated. In addition, the reflectivity for any wavelength can be found, if the modulation period is known. Consequently, the bandwidth is then given by the following expression:

$$\Delta\lambda = 2n_0\Lambda\sqrt{\frac{\delta n^2}{n_0^2} + \frac{4\Lambda^2}{d^2}} \ . \tag{A.8}$$

This equation determines the wavelength interval between the first zeros of Equation (A.6), which is also a very good approximation for the FWHM bandwidth in case of high-reflectivity gratings.

Appendix B

Additional Data

B.1 Structure and standing wave pattern

The graphs show the refractive index profiles of the structures (black) and the calculated standing wave patterns (red) in each of the eight quantum-dot saturable absorbers.

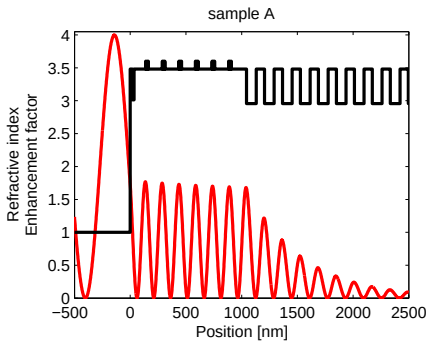

(a)

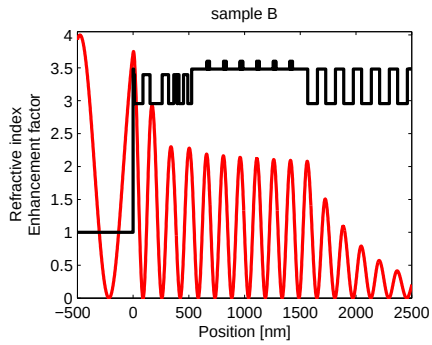

(b)

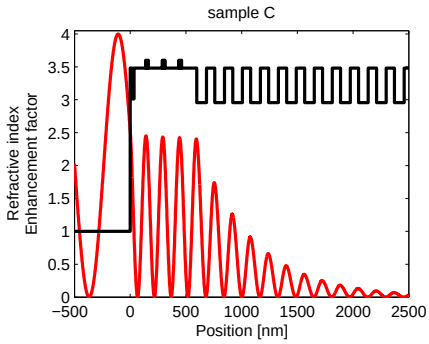
sample C
Refractive index
Enhancement factor
Position [nm]

(c)

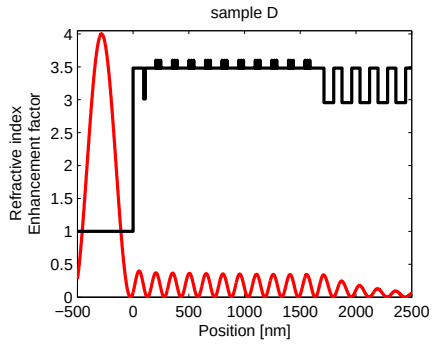
sample D
Refractive index
Enhancement factor
Position [nm]

(d)

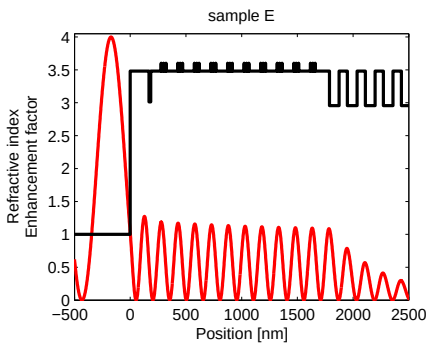
sample E
Refractive index
Enhancement factor
Position [nm]

(e)

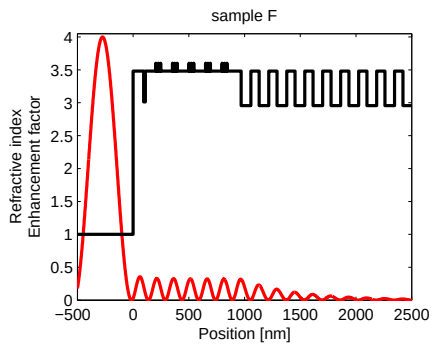
sample F
Refractive index
Enhancement factor
Position [nm]

(f)

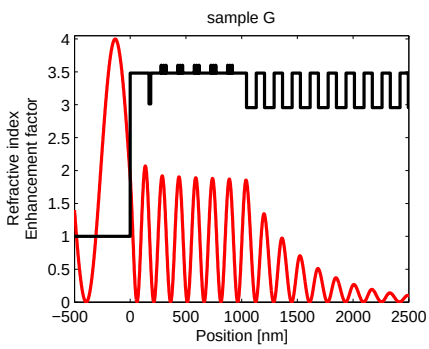
sample G
Refractive index
Enhancement factor
Position [nm]

(g)

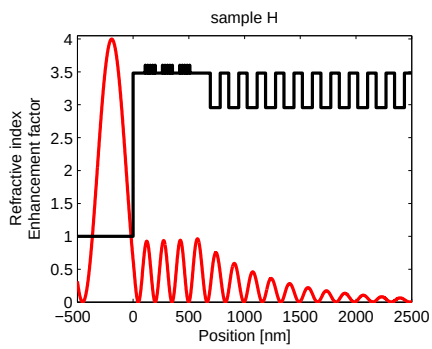
sample H
Refractive index
Enhancement factor
Position [nm]

(h)

B.2 Wavelength-dependent enhancement factor

The graphs show the field enhancement at the centre of the first QD group as a function of wavelength.

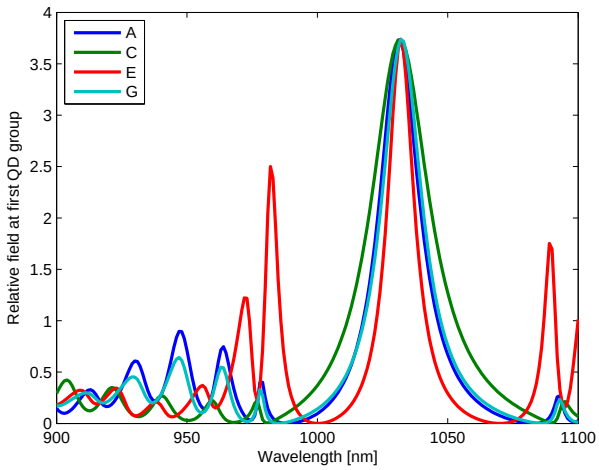

(a)

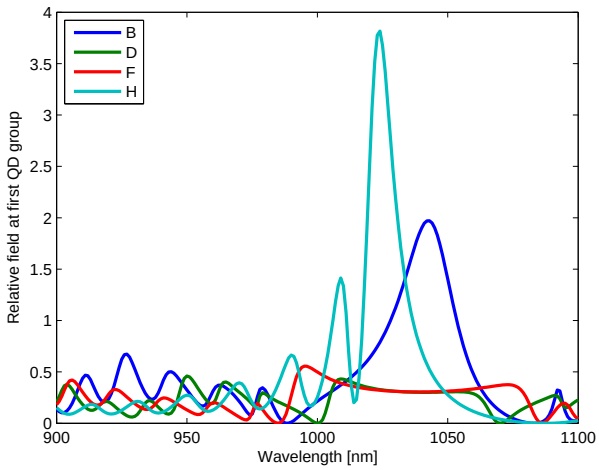

(b)

B.3 Group delay dispersion

The graphs show the calculated (blue, solid line) and measured (red, dashed line) group delay dispersion (GDD) for each sample.

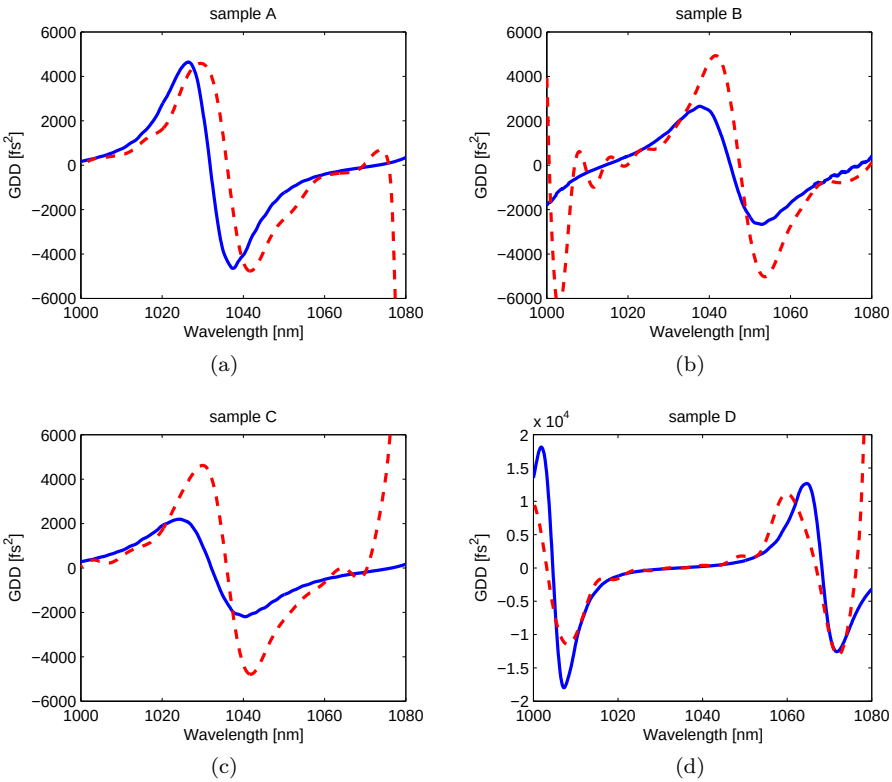

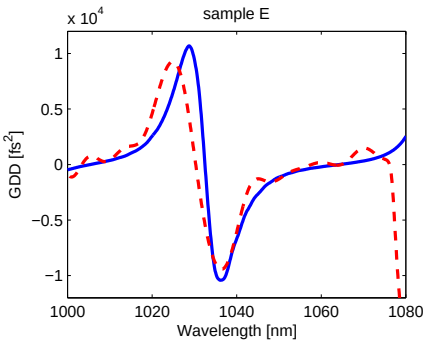
x 10^4
sample E
GDD [fs^2]
Wavelength [nm]
1
0.5
0
−0.5
−1
1000
1020
1040
1060
1080

(e)

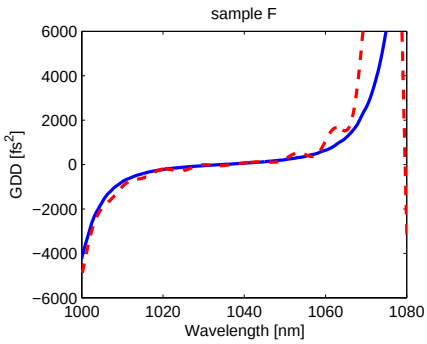
sample F
GDD [fs^2]
Wavelength [nm]
6000
4000
2000
0
−2000
−4000
−6000
1000
1020
1040
1060
1080

(f)

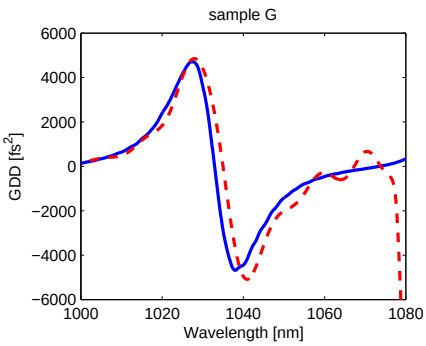
sample G
GDD [fs^2]
Wavelength [nm]
6000
4000
2000
0
−2000
−4000
−6000
1000
1020
1040
1060
1080

(g)

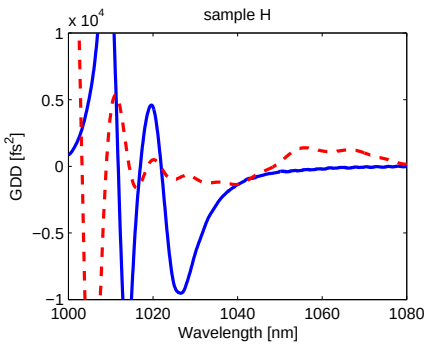
x 10^4
sample H
GDD [fs^2]
Wavelength [nm]
1
0.5
0
−0.5
−1
1000
1020
1040
1060
1080

(h)

B.4 Nonlinear reflectivity

The graphs show the measured nonlinearity (blue dots) and a fit (red line) to the data according to the model function described by Equation (4.2).

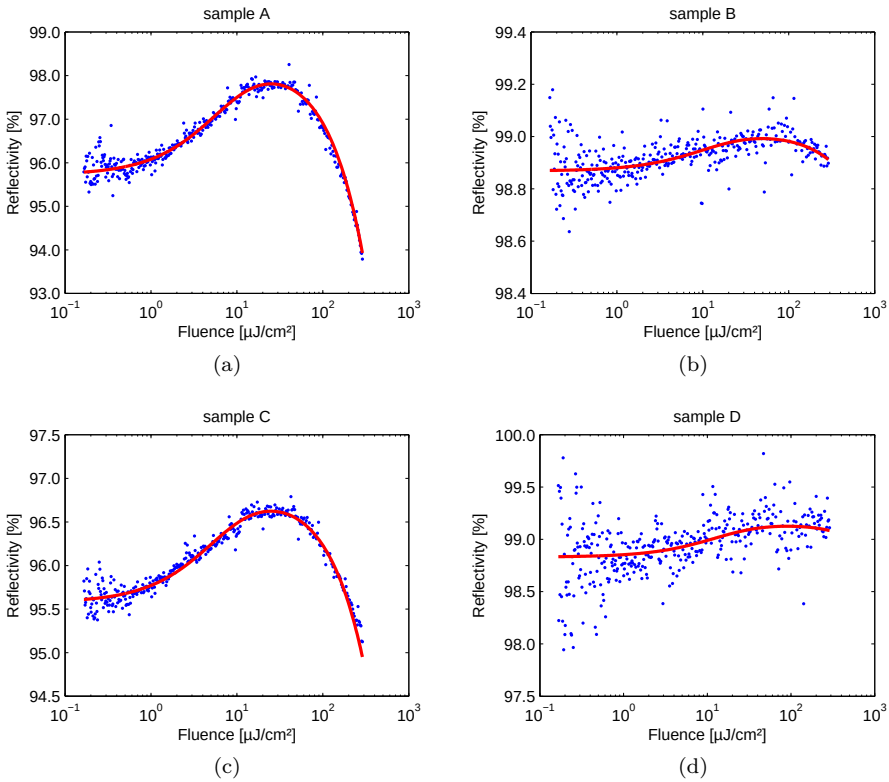

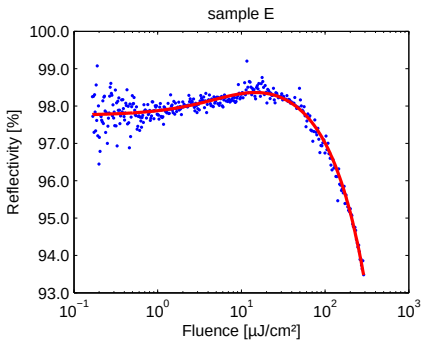
sample E
Reflectivity [%]
Fluence [μJ/cm²]

(e)

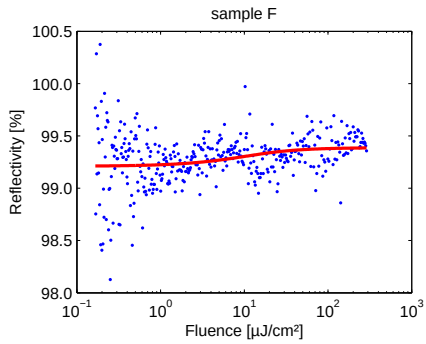
sample F
Reflectivity [%]
Fluence [μJ/cm²]

(f)

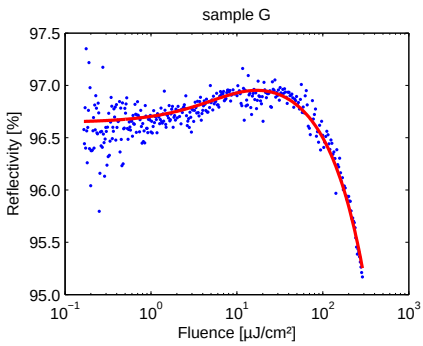
sample G
Reflectivity [%]
Fluence [μJ/cm²]

(g)

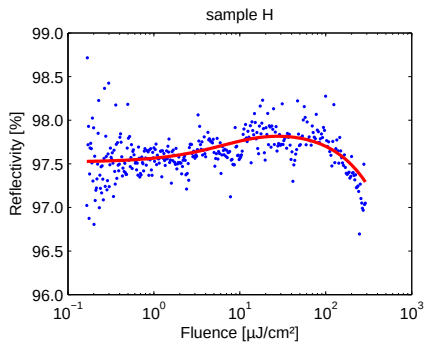
sample H
Reflectivity [%]
Fluence [μJ/cm²]

(h)

B.5 Time resolved PL spectra

The excitation fluence in these experiments was $19\,\mu J/cm^2$ for all of the samples except for sample H, where the data from a stronger excitation with a fluence of $550\,\mu J/cm^2$ is presented in order to confirm, that no luminescence from the QDs could be detected. The first eight figures show the temporally as well as spectrally resolved PL signals. Each complete data set is the combination of three consecutive measurements at centre wavelengths of 898 nm, 974 nm and 1050 nm. This leads to different noise levels in the different wavelength intervals, since the sensitivity could be adapted to the present signal maximum in each interval. The remaining figures show the time-resolved PL spectra integrated over a wavelength interval containing the QDs' PL. Three different excitation fluences were used: $6.3\,\mu J/cm^2$ (red), $19\,\mu J/cm^2$ (green), and $57\,\mu J/cm^2$ (blue). For sample H, only the result from excitation at the above mentioned value of $550\,\mu J/cm^2$ is shown.

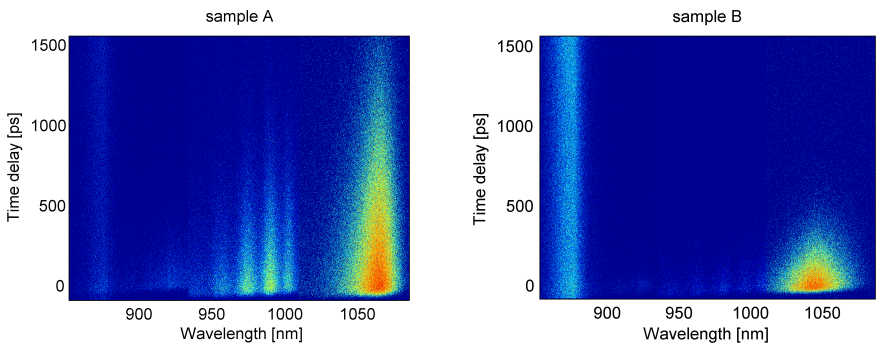

(a)

(b)

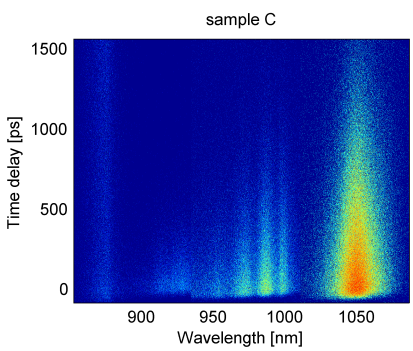

(c)

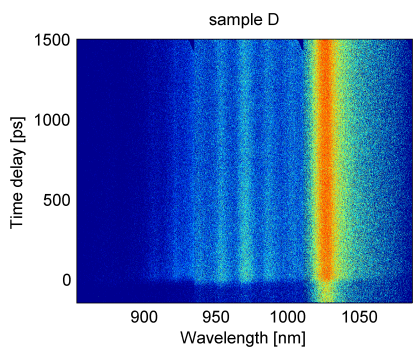

(d)

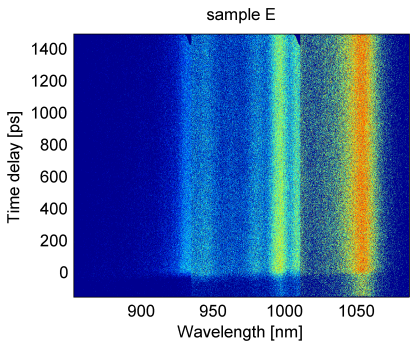
sample E
Time delay [ps]
1400
1200
1000
800
600
400
200
0
900
950
1000
1050
Wavelength [nm]

(e)

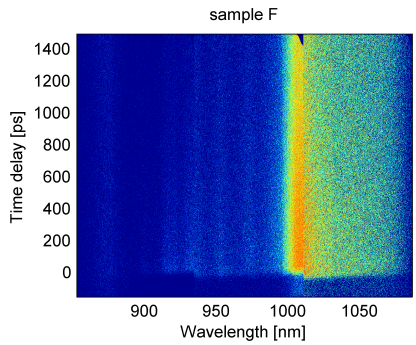
sample F
Time delay [ps]
1400
1200
1000
800
600
400
200
0
900
950
1000
1050
Wavelength [nm]

(f)

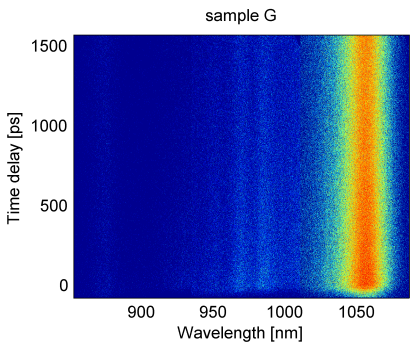
sample G
Time delay [ps]
1500
1000
500
0
900
950
1000
1050
Wavelength [nm]

(g)

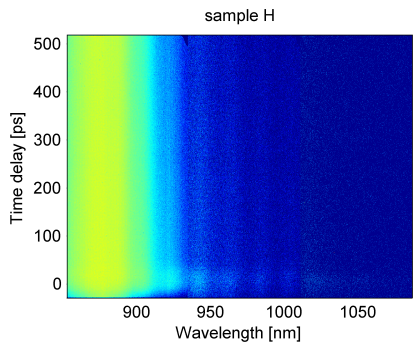
sample H
Time delay [ps]
500
400
300
200
100
0
900
950
1000
1050
Wavelength [nm]

(h)

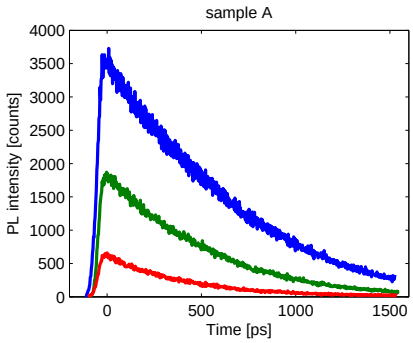
sample A
PL intensity [counts]
Time [ps]
0
500
1000
1500
2000
2500
3000
3500
4000

(i)

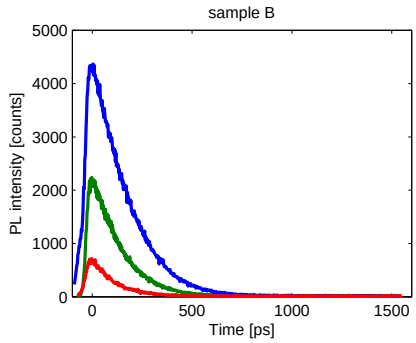
sample B
PL intensity [counts]
Time [ps]
0
500
1000
1500
2000
3000
4000
5000

(j)

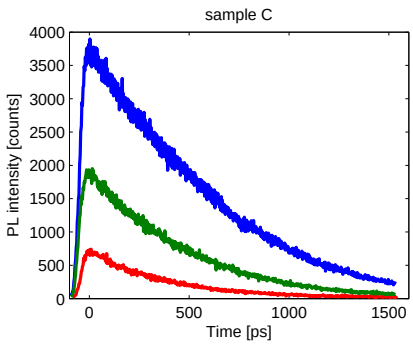
sample C
PL intensity [counts]
Time [ps]
0
500
1000
1500
2000
2500
3000
3500
4000

(k)

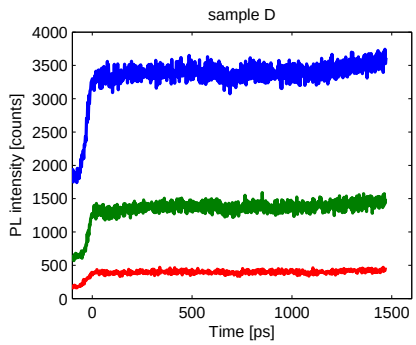
sample D
PL intensity [counts]
Time [ps]
0
500
1000
1500
2000
2500
3000
3500
4000

(l)

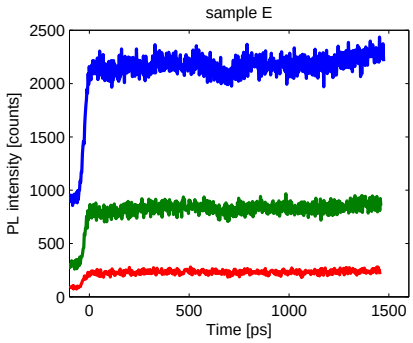
sample E
PL intensity [counts]
Time [ps]
0
500
1000
1500
2000
2500

(m)

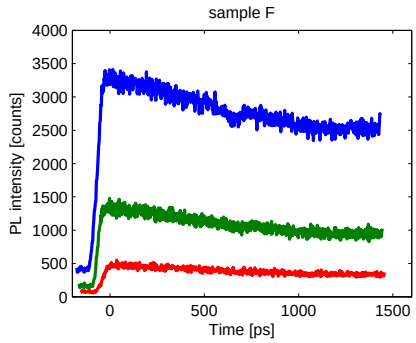
sample F
PL intensity [counts]
Time [ps]
0
500
1000
1500
2000
2500
3000
3500
4000

(n)

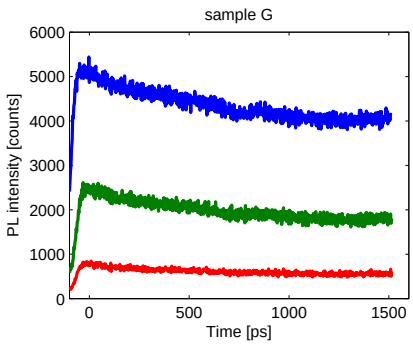
sample G
PL intensity [counts]
Time [ps]
0
1000
2000
3000
4000
5000
6000

(o)

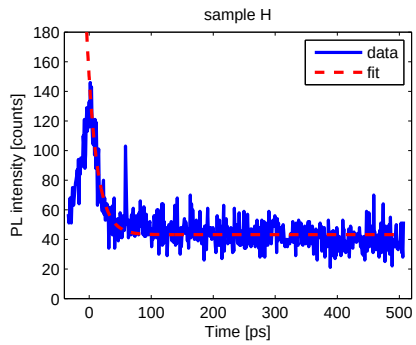
sample H
data
fit
PL intensity [counts]
Time [ps]
0
20
40
60
80
100
120
140
160
180

(p)

B.6 Integrated PL spectra

The figures below show the spectrally resolved PL signals presented in Section B.5, integrated over time. Here, however, the data sets have not been normalised.

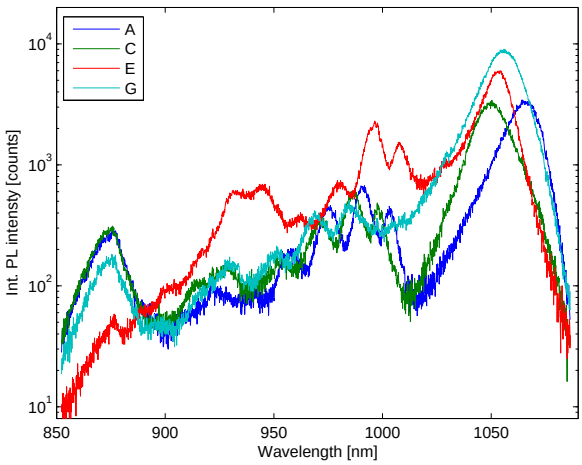

(a)

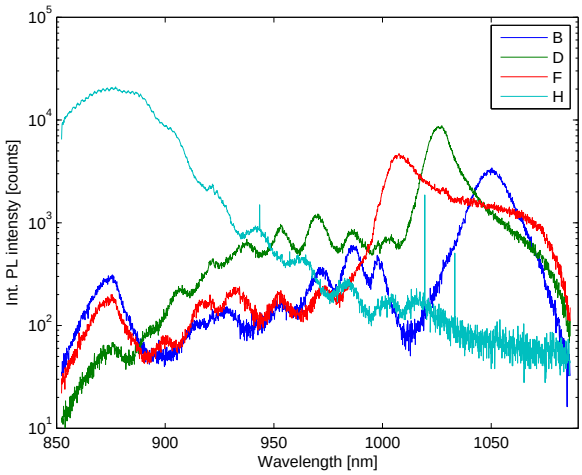

(b)

References

[1] H. W. Mocker and R. J. Collins, *Mode Competition and Self-Locking Effects in a Q-switched Ruby Laser*, Applied Physics Letters **7**, 270 (1965).

[2] W. Schmidt and F. Schäfer, *Self-mode-locking of dye-lasers with saturated absorbers*, Physics Letters A **26**, 558 (1968).

[3] E. P. Ippen, C. V. Shank and A. Dienes, *Passive mode locking of the cw dye laser*, Applied Physics Letters **21**, 348 (1972).

[4] W. Sibbett, A. A. Lagatsky and C. T. A. Brown, *The development and application of femtosecond laser systems*, Optics Express **20**, 6989 (2012).

[5] R. R. Gattass and E. Mazur, *Femtosecond laser micromachining in transparent materials*, Nature Photonics **2**, 219 (2008).

[6] R. Carriles, D. N. Schafer, K. E. Sheetz, J. J. Field, R. Cisek, V. Barzda, A. W. Sylvester and J. A. Squier, *Invited Review Article: Imaging techniques for harmonic and multiphoton absorption fluorescence microscopy*, Review of Scientific Instruments **80**, 081101 (2009).

[7] A. H. Zewail, *Femtochemistry: Atomic-Scale Dynamics of the Chemical Bond Using Ultrafast Lasers (Nobel Lecture)*, Angewandte Chemie International Edition **39**, 2586 (2000).

[8] W. Knox, *Ultrafast technology in telecommunications*, IEEE Journal of Selected Topics in Quantum Electronics **6**, 1273 (2000).

[9] T. Udem, R. Holzwarth and T. W. Hänsch, *Optical frequency metrology*, Nature **416**, 233 (2002).

[10] G. Cerullo, D. Polli, G. Lanzani, S. D. Silvestri, H. Hashimoto and R. J. Cogdell, *Photosynthetic Light Harvesting by Carotenoids: Detection of an Intermediate Excited State*, Science **298**, 2395 (2002).

[11] P. B. Corkum and F. Krausz, *Attosecond science*, Nature Physics **3**, 381 (2007).

[12] T. Brabec and F. Krausz, *Intense few-cycle laser fields: Frontiers of nonlinear optics*, Rev. Mod. Phys. **72**, 545–591 (2000).

[13] T. W. Hänsch, *Nobel Lecture: Passion for precision*, Reviews of Modern Physics **78**, 1297 (2006).

[14] H.-G. Weber, R. Ludwig, S. Ferber, C. Schmidt-Langhorst, M. Kroh, V. Marembert, C. Boerner and C. Schubert, *Ultrahigh-Speed OTDM-Transmission Technology*, Journal of Lightwave Technology **24**, 4616 (2006).

[15] B. N. Chichkov, C. Momma, S. Nolte, F. von Alvensleben and A. Tünnermann, *Femtosecond, picosecond and nanosecond laser ablation of solids*, Applied Physics A **63**, 109 (1996).

[16] W. Drexler, U. Morgner, F. X. Kärtner, C. Pitris, S. A. Boppart, X. D. Li, E. P. Ippen and J. G. Fujimoto, *In vivo ultrahigh-resolution optical coherence tomography*, Optics Letters **24**, 1221 (1999).

[17] J. Squier and M. Müller, *High resolution nonlinear microscopy: A review of sources and methods for achieving optimal imaging*, Review of Scientific Instruments **72**, 2855 (2001).

[18] U. Keller, *Ultrafast solid-state laser oscillators: a success story for the last 20 years with no end in sight*, Applied Physics B: Lasers and Optics **100**, 15 (2010).

[19] G. Huber, C. Kränkel and K. Petermann, *Solid-state lasers: status and future*, Journal of the Optical Society of America B **27**, B93 (2010).

[20] Z. Y. Zhang, A. E. H. Oehler, B. Resan, S. Kurmulis, K. J. Zhou, Q. Wang, M. Mangold, T. Südmeyer, U. Keller, K. J. Weingarten and R. A. Hogg, *1.55 μm InAs/GaAs Quantum Dots and High Repetition Rate Quantum Dot SESAM Mode-locked Laser*, Scientific Reports **2**, (2012).

[21] Z. Sun, T. Hasan and A. C. Ferrari, in *Ultrafast lasers mode-locked by nanotubes and graphene*, Physica. E, low-dimentional systems and nanostructures (Elsevier, 2012), Vol. 44, 1082–1091.

[22] F. Rotermund, W. B. Cho, S. Y. Choi, I. H. Baek, J. H. Yim, S. Lee, A. Schmidt, G. Steinmeyer, U. Griebner, D. I. Yeom, K. Kim and V. Petrov, *Mode-locking of solid-state lasers by single-walled carbon-nanotube based saturable absorbers*, Quantum Electronics **42**, 663 (2012).

[23] C. Rulliére, in *Femtosecond Laser Pulses*, edited by C. Rulliére (Springer, 2003).

[24] U. Keller, *Ultrafast solid-state lasers* (Elsevier, 2004), Vol. Volume 46, 1–115.

[25] F. X. Kärtner, *Few-cycle laser pulse generation and its applications* (Springer, 2004).

[26] U. Keller, *Ultrafast solid-state lasers*, Vol. 11 of *Landolt-Börnstein - Group VIII Advanced Materials and Technologies Numerical Data and Functional Relationships in Science and Technology* (2007).

[27] J.-C. Diels and W. Rudolph, in *Ultrashort Laser Pulse Phenomena*, 2nd ed., edited by J.-C. Diels and W. Rudolph (Academic Press, 2006).

[28] D. E. Spence, P. N. Kean and W. Sibbett, *60-fsec pulse generation from a self-mode-locked Ti:sapphire laser*, Optics Letters **16**, 42–44 (1991).

[29] T. Brabec, C. Spielmann, P. F. Curley and F. Krausz, *Kerr lens mode locking*, Opt. Lett. **17**, 1292–1294 (1992).

[30] Y. Pang, V. Yanovsky, F. Wise and B. I. Minkov, *Self-mode-locked Cr:forsterite laser*, Optics Letters **18**, 1168 (1993).

[31] M. Ramaswamy, A. S. Gouveia-Neto, D. K. Negus, J. A. Izatt and J. G. Fujimoto, *2.3 ps pulses from a Kerr-lens mode-locked lamp-pumped Nd:YLF laser with a microdot mirror*, Optics Letters **18**, 1825 (1993).

[32] H. Liu, J. Nees and G. Mourou, *Diode-pumped Kerr-lens mode-locked Yb:KY(WO4)2 laser*, Opt. Lett. **26**, 1723–1725 (2001).

[33] R. N. Hall, G. E. Fenner, J. D. Kingsley, T. J. Soltys and R. O. Carlson, *Coherent Light Emission From GaAs Junctions*, Physical Review Letters **9**, 366 (1962).

[34] N. V. Kuleshov, A. A. Lagatsky, A. V. Podlipensky, V. P. Mikhailov and G. Huber, *Pulsed laser operation of Yb-doped KY(WO4)2 and KGd(WO4)2*, Opt. Lett. **22**, 1317–1319 (1997).

[35] U. Keller, D. A. B. Miller, G. D. Boyd, T. H. Chiu, J. F. Ferguson and M. T. Asom, *Solid-state low-loss intracavity saturable absorber for Nd:YLF lasers: an antiresonant semiconductor Fabry-Perot saturable absorber*, Optics Letters **17**, 505 (1992).

[36] U. Keller, *Recent developments in compact ultrafast lasers*, Nature **424**, 831 (2003).

[37] F. X. Kärtner, I. D. Jung and U. Keller, *Soliton mode-locking with saturable absorbers*, IEEE Journal of Selected Topics in Quantum Electronics **2**, 540 (1996).

[38] J. Neuhaus, D. Bauer, J. Zhang, A. Killi, J. Kleinbauer, M. Kumkar, S. Weiler, M. Guina, D. H. Sutter and T. Dekorsy, *Subpicosecond thin-disk laser oscillator with pulse energies of up to 25.9 microjoules by use of an active multipass geometry*, Optics Express **16**, 20530 (2008).

[39] L. Krainer, R. Paschotta, S. Lecomte, M. Moser, K. J. Weingarten and U. Keller, *Compact Nd:YVO4 lasers with pulse repetition rates up to 160 GHz*, IEEE Journal of Quantum Electronics **38**, 1331 (2002).

[40] A. A. Lagatsky, F. Fusari, S. Calvez, J. A. Gupta, V. E. Kisel, N. V. Kuleshov, C. T. A. Brown, M. D. Dawson and W. Sibbett, *Passive mode locking of a Tm,Ho:KY(WO4)2 laser around 2 μm*, Opt. Lett. **34**, 2587–2589 (2009).

[41] A.-R. Bellancourt, Y. Barbarin, D. J. H. C. Mass, M. Shafiei, M. Hoffmann, M. Golling, T. Südmeyer and U. Keller, *Low saturation fluence antiresonant quantumdot SESAMs for MIXSEL integration*, Opt. Express **17**, 9704–9711 (2009).

[42] S. Y. Set, H. Yaguchi, Y. Tanaka and M. Jablonski, *Laser Mode Locking Using a Saturable Absorber Incorporating Carbon Nanotubes*, J. Lightwave Technol. **22**, 51 (2004).

[43] T. R. Schibli, K. Minoshima, H. Kataura, E. Itoga, N. Minami, S. Kazaoui, K. Miyashita, M. Tokumoto and Y. Sakakibara, *Ultrashort pulse-generation by saturable absorber mirrors based on polymer-embedded carbon nanotubes*, Opt. Express **13**, 8025 (2005).

[44] F. Krausz, M. E. Fermann, T. Brabec, P. F. Curley, M. Hofer, M. H. Ober, C. Spielmann, E. Wintner and A. J. Schmidt, *Femtosecond solid-state lasers*, IEEE Journal of Quantum Electronics **28**, 2097 (1992).

[45] H. A. Haus, M. Margalit and C. X. Yu, *Quantum noise of a mode-locked laser*, Journal of the Optical Society of America B **17**, 1240 (2000).

[46] M. DiDomenico, *Small-Signal Analysis of Internal (Coupling-Type) Modulation of Lasers*, Journal of Applied Physics **35**, 2870 (1964).

[47] L. E. Hargrove, R. L. Fork and M. A. Pollack, *Locking of He-Ne Laser Modes Induced by Synchronous Intracavity Modulation*, Applied Physics Letters **5**, 4 (1964).

[48] A. Yariv, *Internal Modulation in Multimode Laser Oscillators*, Journal of Applied Physics **36**, 388 (1965).

[49] G. New, *Pulse evolution in mode-locked quasi-continuous lasers*, Quantum Electronics, IEEE Journal of **10**, 115 (1974).

[50] H. A. Haus, *Theory of mode locking with a fast saturable absorber*, J. Appl. Phys. **46**, 3049 (1975).

[51] H. Haus, C. Shank and E. Ippen, *Shape of passively mode-locked laser pulses*, Optics Communications **15**, 29 (1975).

[52] L. F. Mollenauer and R. H. Stolen, *The soliton laser*, Optics Letters **9**, 13 (1984).

[53] P. N. Kean, X. Zhu, D. W. Crust, R. S. Grant, N. Langford and W. Sibbett, *Enhanced mode locking of color-center lasers*, Optics Letters **14**, 39 (1989).

[54] E. P. Ippen, H. A. Haus and L. Y. Liu, *Additive pulse mode locking*, Journal of the Optical Society of America B **6**, 1736 (1989).

[55] A. Hasegawa and F. Tappert, *Transmission of stationary nonlinear optical pulses in dispersive dielectric fibers. I. Anomalous dispersion*, Applied Physics Letters **23**, 142 (1973).

[56] A. Hasegawa and F. Tappert, *Transmission of stationary nonlinear optical pulses in dispersive dielectric fibers. II. Normal dispersion*, Applied Physics Letters **23**, 171 (1973).

[57] L. F. Mollenauer, R. H. Stolen and J. P. Gordon, *Experimental Observation of Picosecond Pulse Narrowing and Solitons in Optical Fibers*, Physical Review Letters **45**, 1095 (1980).

[58] M. Piche and F. Salin, *Self-mode locking of solid-state lasers without apertures*, Opt. Lett. **18**, 1041 (1993).

[59] U. Morgner, F. X. Kärtner, S. H. Cho, Y. Chen, H. A. Haus, J. G. Fujimoto, E. P. Ippen, V. Scheuer, G. Angelow and T. Tschudi, *Sub-two-cycle pulses from a Kerr-lens mode-locked Ti:sapphire laser*, Opt. Lett. **24**, 411–413 (1999).

[60] F. Kärtner, J. der Au and U. Keller, *Mode-locking with slow and fast saturable absorbers-what's the difference?*, IEEE Journal of Selected Topics in Quantum Electronics **4**, 159 (1998).

[61] U. Keller, K. J. Weingarten, F. X. Kärtner, D. Kopf, B. Braun, I. D. Jung, R. Fluck, C. Hönninger, N. Matuschek and J. Aus der Au, *Semiconductor saturable absorber mirrors (SESAM's) for femtosecond to nanosecond pulse generation in solid-state lasers*, IEEE Journal of Selected Topics in Quantum Electronics **2**, 435 (1996).

[62] F. X. Kärtner and U. Keller, *Stabilization of solitonlike pulses with a slow saturable absorber*, Optics Letters **20**, 16 (1995).

[63] I. D. Jung, F. X. Kärtner, L. R. Brovelli, M. Kamp and U. Keller, *Experimental verification of soliton mode locking using only a slow saturable absorber*, Optics Letters **20**, 1892 (1995).

[64] T. Brabec, C. Spielmann and E. Krausz, *Mode locking in solitary lasers*, Opt. Lett. **16**, 1961–1963 (1991).

[65] H. A. Haus, J. G. Fujimoto and E. P. Ippen, *Structures for additive pulse mode locking*, Journal of the Optical Society of America B **8**, 2068 (1991).

[66] U. Keller and G. W. 'tHooft, *Femtosecond pulses from a continuously self-starting passively mode-locked Ti:sapphire laser*, Opt. Lett **16**, 1022 (1991).

[67] U. Keller, *Ultrafast all-solid-state laser technology*, Applied Physics B **58**, 347 (1994).

[68] C. Hönninger, R. Paschotta, F. Morier-Genoud, M. Moser and U. Keller, *Q-switching stability limits of continuous-wave passive mode locking*, J. Opt. Soc. Am. B **16**, 46–56 (1999).

[69] T. Schibli, E. Thoen, F. Kärtner and E. Ippen, *Suppression of Q-switched mode locking and break-up into multiple pulses by inverse saturable absorption*, Applied Physics B: Lasers and Optics **70**, (2000).

[70] A. Schlatter, S. C. Zeller, R. Grange, R. Paschotta and U. Keller, *Pulse-energy dynamics of passively mode-locked solid-state lasers above the Q-switching threshold*, Journal of the Optical Society of America B **21**, 1469 (2004).

[71] E. Rafailov, S. White, A. Lagatsky, A. Miller, W. Sibbett, D. Livshits, A. Zhukov and V. Ustinov, *Fast quantum-dot saturable absorber for passive mode-locking of solid-State lasers*, IEEE Photonics Technology Letters **16**, 2439 (2004).

[72] L. W. Shi, Y. H. Chen, B. Xu, Z. C. Wang, Y. H. Jiao and Z. G. Wang, *Status and trends of short pulse generation using mode-locked lasers based on advanced quantum-dot active media*, Journal of Physics D: Applied Physics **40**, R307 (2007).

[73] Z. Sun, T. Hasan, F. Torrisi, D. Popa, G. Privitera, F. Wang, F. Bonaccorso, D. M. Basko and A. C. Ferrari, *Graphene Mode-Locked Ultrafast Laser*, ArXiv e-prints **-**, (2009).

[74] W. B. Cho, J. H. Yim, S. Y. Choi, S. Lee, A. Schmidt, G. Steinmeyer, U. Griebner, V. Petrov, D. I. Yeom, K. Kim et al., *Carbon Nanotubes: Boosting the Non Linear Optical Response of Carbon Nanotube Saturable Absorbers for Broadband Mode-Locking of Bulk Lasers*, Advanced Functional Materials **20**, (2010).

[75] R. DeSalvo, D. J. Hagan, M. Sheik-Bahae, G. Stegeman, E. W. Van Stryland and H. Vanherzeele, *Self-focusing and self-defocusing by cascaded second-order effects in KTP*, Optics Letters **17**, 28 (1992).

[76] G. I. Stegeman, D. J. Hagan and L. Torner, *$\chi(2)$ cascading phenomena and their applications to all-optical signal processing, mode-locking, pulse compression and solitons*, Optical and Quantum Electronics **28**, 1691 (1996).

[77] K. A. Stankov, *A mirror with an intensity-dependent reflection coefficient*, Applied Physics B **45**, 191 (1988).

[78] D. Feng, N. Ming, J. Hong, Y. Yang, J. Zhu, Z. Yang and Y. Wang, *Enhancement of second -harmonic generation in LiNbO3 crystals with periodic laminar ferroelectric domains*, Applied Physics Letters **37**, 607 (1980).

[79] M. Yamada, N. Nada, M. Saitoh and K. Watanabe, *First-order quasi-phase matched LiNbO3 waveguide periodically poled by applying an external field for efficient blue second-harmonic generation*, Applied Physics Letters **62**, 435 (1993).

[80] H. Karlsson and F. Laurell, *Electric field poling of flux grown $KTiOPO_4$*, Applied Physics Letters **71**, 3474 (1997).

[81] H. A. Haus, *Mode-locking of lasers*, IEEE Journal of Selected Topics in Quantum Electronics **6**, 1173 (2000).

[82] J. D. Moores, *On the Ginzburg-Landau laser mode-locking model with fifth-order saturable absorber term*, Optics Communications **96**, 65 (1993).

[83] J. M. Soto-Crespo, N. N. Akhmediev and V. V. Afanasjev, *Stability of the pulselike solutions of the quintic complex Ginzburg-Landau equation*, Journal of the Optical Society of America B **13**, 1439 (1996).

[84] A. Chong, J. Buckley, W. Renninger and F. Wise, *All-normal-dispersion femtosecond fiber laser*, Optics Express **14**, 10095 (2006).

[85] N. Akhmediev, J. M. Soto-Crespo and G. Town, *Pulsating solitons, chaotic solitons, period doubling, and pulse coexistence in mode-locked lasers: Complex Ginzburg-Landau equation approach*, Physical Review E **63**, 056602 (2001).

[86] H. A. Haus and M. N. Islam, *Theory of the soliton laser*, IEEE J. Quantum. Electron. **21**, 1172 (1985).

[87] R. Paschotta and U. Keller, *Passive mode locking with slow saturable absorbers*, Applied Physics B: Lasers and Optics **73**, 653 (2001).

[88] G. New, *Mode-locking of quasi-continuous lasers*, Optics Communications **6**, 188 (1972).

[89] S. Shapiro and M. Duguay, *Observation of subpicosecond components in the mode-locked Nd:glass laser*, Physics Letters A **28**, 698 (1969).

[90] A. Laubereau and W. Kaiser, *Generation and applications of passively mode-locked picosecond light pulses*, Opto-electronics **6**, 1 (1974).

[91] R. L. Fork, O. E. Martinez and J. P. Gordon, *Negative dispersion using pairs of prisms*, Optics Letters **9**, 150 (1984).

[92] D. Kopf, G. Zhang, R. Fluck, M. Moser and U. Keller, *All-in-one dispersion-compensating saturable absorber mirror for compact femtosecond laser sources*, Optics Letters **21**, 486 (1996).

[93] F. X. Kärtner, N. Matuschek, T. Schibli, U. Keller, H. A. Haus, C. Heine, R. Morf, V. Scheuer, M. Tilsch and T. Tschudi, *Design and fabrication of double-chirped mirrors*, Opt. Lett. **22**, 831–833 (1997).

[94] B. R. Bennett, R. A. Soref and J. A. Del Alamo, *Carrier-induced change in refractive index of InP, GaAs and InGaAsP*, IEEE Journal of Quantum Electronics **26**, 113 (1990).

[95] R. Paschotta, R. Häring, A. Garnache, S. Hoogland, A. C. Tropper and U. Keller, *Soliton-like pulse-shaping mechanism in passively mode-locked surface-emitting semiconductor lasers*, Applied Physics B **75**, 445 (2002).

[96] O. D. Sieber, M. Hoffmann, V. J. Wittwer, M. Mangold, M. Golling, B. W. Tilma, T. Südmeyer and U. Keller, *Experimentally verified pulse formation model for high-power femtosecond VECSELs*, Applied Physics B 1 (2013).

[97] H. Haus, *Parameter ranges for CW passive mode locking*, Quantum Electronics, IEEE Journal of **12**, 169 (1976).

[98] R. Grange, *Near infrared semiconductor saturable absorber mirrors for high repetition rate lasers*, Ph.D. thesis, ETH Zürich, 2006.

[99] V. Petrov, U. Griebner, D. Ehrt and W. Seeber, *Femtosecond self mode locking of Yb:fluoride phosphate glass laser*, Optics Letters **22**, 408 (1997).

[100] P. Wasylczyk, P. Wnuk and C. Radzewicz, *Passively modelocked, diode-pumped Yb:KYW femtosecond oscillator with 1 GHz repetition rate*, Opt. Express **17**, 5630–5635 (2009).

[101] P. W. Smith, Y. Silberberg and D. A. B. Miller, *Mode locking of semiconductor diode lasers using saturable excitonic nonlinearities*, Journal of the Optical Society of America B **2**, 1228 (1985).

[102] M. N. Islam, E. R. Sunderman, I. Bar-Joseph, N. Sauer and T. Y. Chang, *Multiple quantum well passive mode locking of a NaCl color center laser*, Applied Physics Letters **54**, 1203 (1989).

[103] Y. Silberberg, P. W. Smith, D. A. B. Miller, B. Tell, A. C. Gossard and W. Wiegmann, *Fast nonlinear optical response from proton-bombarded multiple quantum well structures*, Applied Physics Letters **46**, 701 (1985).

[104] G. J. Spühler, K. J. Weingarten, R. Grange, L. Krainer, M. Haiml, V. Liverini, M. Golling, S. Schön and U. Keller, *Semiconductor saturable absorber mirror structures with low saturation fluence*, Appl. Phys. B: Lasers Opt. **81**, 27 (2005).

[105] N. Sarukura, Y. Ishida, T. Yanagawa and H. Nakano, *All solid-state cw passively mode-locked Ti:sapphire laser using a colored glass filter*, Applied Physics Letters **57**, 229 (1990).

[106] K. V. Yumashev, V. P. Mikhailov, P. V. Prokoshin, S. P. Jmako and I. V. Bodnar, *CuInSSe-doped glass saturable absorbers for the passive mode-locking of neodymium lasers*, Applied Physics Letters **65**, 2768 (1994).

[107] P. T. Guerreiro, S. Ten, N. F. Borrelli, J. Butty, G. E. Jabbour and N. Peyghambarian, *PbS quantum-dot doped glasses as saturable absorbers for mode locking of a Cr:forsterite laser*, Appl. Phys. Lett. **71**, 1595 (1997).

[108] K. Wundke, S. Pötting, J. Auxier, A. Schülzgen, N. Peyghambarian and N. F. Borrelli, *PbS quantum-dot-doped glasses for ultrashort-pulse generation*, Applied Physics Letters **76**, 10 (2000).

[109] A. Lagatsky, C. Leburn, C. Brown, W. Sibbett, A. Malyarevich, V. Savitski, K. Yumashev, E. Raaben and A. Zhilin, *Passive mode locking of a Cr4+:YAG laser by PbS quantum-dot-doped glass saturable absorber*, Optics Communications **241**, 449 (2004).

[110] S. Schmitt-Rink, D. A. B. Miller and D. S. Chemla, *Theory of the linear and nonlinear optical properties of semiconductor microcrystallites*, Physical Review B **35**, 8113 (1987).

[111] M. Grundmann, J. Christen, N. N. Ledentsov, J. Böhrer, D. Bimberg, S. S. Ruvimov, P. Werner, U. Richter, U. Gösele, J. Heydenreich, V. M. Ustinov, A. Y. Egorov, A. E. Zhukov, P. S. Kop'ev and Z. I. Alferov, *Ultranarrow Luminescence Lines from Single Quantum Dots*, Physical Review Letters **74**, 4043 (1995).

[112] D. Lorenser, H. J. Unold, D. J. H. C. Maas, A. Aschwanden, R. Grange, R. Paschotta, D. Ebling, E. Gini and U. Keller, *Towards wafer-scale integration of high repetition rate passively mode-locked surface-emitting semiconductor lasers*, Applied Physics B **79**, 927 (2004).

[113] A. A. Lagatsky, F. M. Bain, C. T. A. Brown, W. Sibbett, D. A. Livshits, G. Erbert and E. U. Rafailov, *Low-loss quantum-dot-based saturable absorber for efficient femtosecond pulse generation*, Applied Physics Letters **91**, 231111 (2007).

[114] C. Scurtescu, Z. Y. Zhang, J. Alcock, R. Fedosejevs, M. Blumin, I. Saveliev, S. Yang, H. Ruda and Y. Y. Tsui, *Quantum dot saturable absorber for passive mode locking of Nd:YVO4 lasers at 1064 nm*, Applied Physics B: Lasers and Optics **87**, 671 (2007).

[115] I. N. Stranski and L. Krastanow, *Zur Theorie der orientierten Ausscheidung von Ionenkristallen aufeinander*, Sitz. Ber. Akad. Wiss. Math.-naturwiss. Kl. Abt. IIb **146**, 797 (1938).

[116] F. Houzay, C. Guille, J. Moison, P. Henoc and F. Barthe, *First stages of the MBE growth of InAs on (001)GaAs*, Journal of Crystal Growth **81**, 67 (1987).

[117] J. M. García, G. Medeiros-Ribeiro, K. Schmidt, T. Ngo, J. L. Feng, A. Lorke, J. Kotthaus and P. M. Petroff, *Intermixing and shape changes during the formation of InAs self-assembled quantum dots*, Applied Physics Letters **71**, 2014 (1997).

[118] H. Saito, K. Nishi and S. Sugou, *Shape transition of InAs quantum dots by growth at high temperature*, Applied Physics Letters **74**, 1224 (1999).

[119] D. M. Bruls, J. W. A. M. Vugs, P. M. Koenraad, H. W. M. Salemink, J. H. Wolter, M. Hopkinson, M. S. Skolnick, F. Long and S. P. A. Gill, *Determination of the shape and indium distribution of low-growth-rate InAs quantum dots by cross-sectional scanning tunneling microscopy*, Applied Physics Letters **81**, 1708 (2002).

[120] M. Grundmann, O. Stier and D. Bimberg, *InAs/GaAs pyramidal quantum dots: Strain distribution, optical phonons, and electronic structure*, Physical Review B **52**, 11969 (1995).

[121] J. M. Moison, F. Houzay, F. Barthe, L. Leprince, E. André and O. Vatel, *Self-organized growth of regular nanometer-scale InAs dots on GaAs*, Applied Physics Letters **64**, 196 (1994).

[122] H. Fu, L.-W. Wang and A. Zunger, *Excitonic exchange splitting in bulk semiconductors*, Physical Review B **59**, 5568 (1999).

[123] I. Pelant and J. Valenta, *Luminescence Spectroscopy of Semiconductors* (Oxford University Press, 2012).

[124] H. Jiang and J. Singh, *Strain distribution and electronic spectra of InAs/GaAs self-assembled dots: An eight-band study*, Physical Review B **56**, 4696 (1997).

[125] F. Adler, M. Geiger, A. Bauknecht, F. Scholz, H. Schweizer, M. H. Pilkuhn, B. Ohnesorge and A. Forchel, *Optical transitions and carrier relaxation in self assembled InAs/GaAs quantum dots*, Journal of Applied Physics **80**, 4019 (1996).

[126] J.-Y. Marzin and G. Bastard, *Calculation of the energy levels in InAs-GaAs quantum dots*, Solid State Communications **92**, 437 (1994).

[127] S. V. Gaponenko, *Optical Properties of Semiconductor Nanocrystals* (Cambridge University Press, 1998).

[128] C. B. Murray, D. J. Norris and M. G. Bawendi, *Synthesis and characterization of nearly monodisperse CdE (E = sulfur, selenium, tellurium) semiconductor nanocrystallites*, Journal of the American Chemical Society **115**, 8706 (1993).

[129] U. Bockelmann, *Electronic relaxation in quasi-one- and zero-dimensional structures*, Semiconductor Science and Technology **9**, 865 (1994).

[130] A. Lagatsky, C. Brown and W. Sibbett, *Highly efficient and low threshold diode-pumped Kerr-lens mode-locked Yb:KYW laser*, Opt. Express **12**, 3928–3933 (2004).

[131] D. A. Yarotski, R. D. Averitt, N. Negre, S. A. Crooker, A. J. Taylor, G. P. Donati, A. Stintz, L. F. Lester and K. J. Malloy, *Ultrafast carrier-relaxation dynamics in self-assembled InAs/GaAs quantum dots*, Journal of the Optical Society of America B **19**, 1480 (2002).

[132] U. Bockelmann and T. Egeler, *Electron relaxation in quantum dots by means of Auger processes*, Physical Review B **46**, 15574 (1992).

[133] Y. Toda, O. Moriwaki, M. Nishioka and Y. Arakawa, *Efficient Carrier Relaxation Mechanism in InGaAs/GaAs Self-Assembled Quantum Dots Based on the Existence of Continuum States*, Physical Review Letters **82**, 4114 (1999).

[134] H. P. Porte, P. Uhd Jepsen, N. Daghestani, E. U. Rafailov and D. Turchinovich, *Ultrafast release and capture of carriers in InGaAs/GaAs quantum dots observed by time-resolved terahertz spectroscopy*, Applied Physics Letters **94**, 262104 (2009).

[135] P. C. Sercel, *Multiphonon-assisted tunneling through deep levels: A rapid energy-relaxation mechanism in nonideal quantum-dot heterostructures*, Physical Review B **51**, 14532 (1995).

[136] D. F. Schroeter, D. J. Griffiths and P. C. Sercel, *Defect-assisted relaxation in quantum dots at low temperature*, Physical Review B **54**, 1486 (1996).

[137] S. W. Lin, C. Balocco, M. Missous, A. R. Peaker and A. M. Song, *Coexistence of deep levels with optically active InAs quantum dots*, Physical Review B **72**, 165302 (2005).

[138] G. J. Spühler, S. Reffert, M. Haiml, M. Moser and U. Keller, *Output-coupling semiconductor saturable absorber mirror*, Appl. Phys. Lett. **78**, 2733 (2001).

[139] C. Saraceno, C. Schriber, M. Mangold, M. Hoffmann, O. Heckl, C. Baer, M. Golling, T. Südmeyer and U. Keller, *SESAMs for High-Power Oscillators: Design Guidelines and Damage Thresholds*, IEEE Journal of Selected Topics in Quantum Electronics **18**, 29 (2012).

[140] M. Haiml, R. Grange and U. Keller, *Optical characterization of semiconductor saturable absorbers*, Applied Physics B **79**, 331 (2004).

[141] L. R. Brovelli, U. Keller and T. H. Chiu, *Design and operation of antiresonant Fabry-Perot saturable semiconductor absorbers for mode-locked solid-state lasers*, Journal of the Optical Society of America B **12**, 311 (1995).

[142] E. R. Thoen, E. M. Koontz, M. Joschko, P. Langlois, T. R. Schibli, F. X. Kärtner, E. P. Ippen and L. A. Kolodziejski, *Two-photon absorption in semiconductor saturable absorber mirrors*, Applied Physics Letters **74**, 3927 (1999).

[143] R. Grange, M. Haiml, R. Paschotta, G. J. Spühler, L. Krainer, M. Golling, O. Ostinelli and U. Keller, *New regime of inverse saturable absorption for self-stabilizing passively mode-locked lasers*, Appl. Phys. B: Lasers Opt. **80**, 151 (2005).

[144] D. Maas, A. Bellancourt, M. Hoffmann, B. Rudin, Y. Barbarin, M. Golling, T. Südmeyer and U. Keller, *Growth parameter optimization for fast quantum dot SESAMs*, Opt. Express **16**, 18646–18656 (2008).

[145] M. C. Pujol, M. A. Bursukova, F. Güell, X. Mateos, R. Solé, J. Gavaldà, M. Aguiló, J. Massons, F. Díaz, P. Klopp, U. Griebner and V. Petrov, *Growth, optical characterization, and laser operation of a stoichiometric crystal KYb(WO4)2*, Physical Review B **65**, 165121 (2002).

[146] A. Giesen, H. Hügel, A. Voss, K. Wittig, U. Brauch and H. Opower, *Scalable concept for diode-pumped high-power solid-state lasers*, Applied Physics B **58**, 365 (1994).

[147] G. Palmer, M. Siegel, A. Steinmann and U. Morgner, *Microjoule pulses from a passively mode-locked Yb:KY(WO4)2 thin-disk oscillator with cavity dumping*, Optics Letters **32**, 1593 (2007).

[148] C. Saraceno, O. Heckl, C. Baer, C. Schriber, M. Golling, K. Beil, C. Kränkel, T. Südmeyer, G. Huber and U. Keller, *Sub-100 femtosecond pulses from a SESAM modelocked thin disk laser*, Applied Physics B: Lasers and Optics **106**, 559 (2012).

[149] A. McWilliam, A. A. Lagatsky, C. T. A. Brown, W. Sibbett, A. E. Zhukov, V. M. Ustinov, A. P. Vasil'Ev and E. U. Rafailov, *Quantum-dot-based saturable absorber for femtosecond mode-locked operation of a solid-state laser*, Opt. Lett. **31**, 1444 (2006).

[150] A. Schmidt, S. Rivier, W. B. Cho, J. H. Yim, S. Y. Choi, S. Lee, F. Rotermund, D. Rytz, G. Steinmeyer, V. Petrov and U. Griebner, *Sub-100 fs single-walled carbon nanotube saturable absorber mode-locked Yb-laser operation near 1 μm*, Opt. Express **17**, 20109–20116 (2009).

[151] A. Schmidt, S. Rivier, G. Steinmeyer, J. H. Yim, W. B. Cho, S. Lee, F. Rotermund, M. C. Pujol, X. Mateos, M. Aguiló, F. Díaz, V. Petrov and U. Griebner, *Passive mode locking of Yb:KLuW using a single-walled carbon nanotube saturable absorber*, Opt. Lett. **33**, 729–731 (2008).

[152] I. H. Baek, S. Y. Choi, H. W. Lee, W. B. Cho, V. Petrov, A. Agnesi, V. Pasiskevicius, D.-I. Yeom, K. Kim and F. Rotermund, *Single-walled carbon nanotube saturable absorber assisted high-power mode-locking of a Ti:sapphire laser*, Optics Express **19**, 7833 (2011).

[153] H. Iliev, I. Buchvarov, S. Y. Choi, K. Kim, F. Rotermund, U. Griebner and V. Petrov, *Steady state mode-locking of a 1.34 μm Nd:YVO4 laser using a single-walled carbon nanotube saturable absorber*, Applied Physics B **106**, 1 (2012).

[154] S. Iijima and T. Ichihashi, *Single-shell carbon nanotubes of 1-nm diameter*, Nature **363**, 603 (1993).

[155] C. Journet, W. K. Maser, P. Bernier, A. Loiseau, M. L. de la Chapelle, S. Lefrant, P. Deniard, R. Lee and J. E. Fischer, *Large-scale production of single-walled carbon nanotubes by the electric-arc technique*, Nature **388**, 756 (1997).

[156] P. Nikolaev, M. J. Bronikowski, R. Bradley, F. Rohmund, D. T. Colbert, K. Smith and R. E. Smalley, *Gas-phase catalytic growth of single-walled carbon nanotubes from carbon monoxide*, Chemical Physics Letters **313**, 91 (1999).

[157] S. B. Sinnott and R. Andrews, *Carbon Nanotubes: Synthesis, Properties, and Applications*, Critical Reviews in Solid State and Materials Sciences **26**, 145 (2001).

[158] R. Saito, M. Fujita, G. Dresselhaus and M. S. Dresselhaus, *Electronic structure of graphene tubules based on C60*, Physical Review B **46**, 1804 (1992).

[159] T. W. Odom, J. L. Huang, P. Kim and C. M. Lieber, *Structure and electronic properties of carbon nanotubes*, J. Phys. Chem. B **104**, 2794–2809 (2000).

[160] S. M. Bachilo, M. S. Strano, C. Kittrell, R. H. Hauge, R. E. Smalley and R. B. Weisman, *Structure-assigned optical spectra of single-walled carbon nanotubes*, Science **298**, 2361 (2002).

[161] R. Saito, M. Fujita, G. Dresselhaus and M. S. Dresselhaus, *Electronic structure of chiral graphene tubules*, Applied Physics Letters **60**, 2204 (1992).

[162] P. Avouris, M. Freitag and V. Perebeinos, *Carbon-nanotube photonics and optoelectronics*, Nature photonics **2**, 341–350 (2008).

[163] A. Jorio, G. Dresselhaus and M. S. Dresselhaus, in *Carbon Nanotubes*, Vol. 111 of *Topics in Applied Physics*, edited by A. Jorio, G. Dresselhaus and M. S. Dresselhaus (Springer Berlin / Heidelberg, 2008).

[164] V. Scardaci, A. G. Rozhin, F. Hennrich, W. I. Milne and A. C. Ferrari, *Carbon nanotube-polymer composites for photonic devices*, Physica E: Low-dimensional Systems and Nanostructures **37**, 115–118 (2007).

[165] J. H. Yim, W. B. Cho, S. Lee, Y. H. Ahn, K. Kim, H. Lim, G. Steinmeyer, V. Petrov, U. Griebner and F. Rotermund, *Fabrication and characterization of ultrafast carbon nanotube saturable absorbers for solid-state laser mode locking near 1 μm*, Appl. Phys. Lett. **93**, 161106 (2008).

[166] S. Kivistö, T. Hakulinen, A. Kaskela, B. Aitchison, D. P. Brown, A. G. Nasibulin, E. I. Kauppinen, A. Härkönen and O. G. Okhotnikov, *Carbon nanotube films for ultrafast broadband technology*, Optics Express **17**, 2358–2363 (2009).

[167] K. Kashiwagi and S. Yamashita, *Deposition of carbon nanotubes around microfiber via evanascent light*, Opt. Express **17**, 18364–18370 (2009).

[168] H. G. Rosa and E. A. de Souza, *Thin films incorporating carbon nanotubes used as saturable absorbers to passively mode-lock Erbium-doped fiber lasers*, Microwave and Optoelectronics Conference (IMOC), 2009 SBMO/IEEE MTT-S International -, 453–455 (2010).

[169] J. Wang, Y. Chen and W. J. Blau, *Carbon nanotubes and nanotube composites for nonlinear optical devices*, Journal of Materials Chemistry **19**, 7425–7443 (2009).

[170] N. Minami, Y. Kim, K. Miyashita, S. Kazaoui and B. Nalini, *Cellulose derivatives as excellent dispersants for single-wall carbon nanotubes as demonstrated by absorption and photoluminescence spectroscopy*, Applied Physics Letters **88**, 093123 (2006).

[171] E. Van Stryland, *The effect of pulse to pulse variation on ultrashort pulsewidth measurements*, Optics Communications **31**, 93 (1979).

[172] J.-C. M. Diels, J. J. Fontaine, I. C. McMichael and F. Simoni, *Control and measurement of ultrashort pulse shapes (in amplitude and phase) with femtosecond accuracy*, Applied Optics **24**, 1270 (1985).

[173] L. Kornaszewski, G. Maker, G. Malcolm, M. Butkus, E. Rafailov and C. Hamilton, *SESAM-free mode-locked semiconductor disk laser*, Laser & Photonics Reviews **6**, L20–L23 (2012).

[174] K. G. Wilcox and A. C. Tropper, *Comment on SESAM-free mode-locked semiconductor disk laser*, Laser & Photonics Reviews **7**, 422–423 (2013).

[175] L. Kornaszewski, G. Maker, G. Malcolm, M. Butkus, E. U. Rafailov and C. Hamilton, *Reply to comment on SESAM-free mode-locked semiconductor disk laser*, Laser & Photonics Reviews **7**, 555–556 (2013).

[176] L. A. Ostrovskii, *Propagation of Wave Packets and Space-time Self-focusing in a Nonlinear Medium*, Soviet Journal of Experimental and Theoretical Physics **24**, 797 (1967).

[177] G. I. Stegeman and E. M. Wright, *All-optical waveguide switching*, Optical and Quantum Electronics **22**, 95 (1990).

[178] N. R. Belashenkov, S. V. Gagarskii and M. V. Inochkin, *Nonlinear refraction of light on second-harmonic generation*, Optics and Spectroscopy **66**, 806 (1989).

[179] G. Cerullo, S. De Silvestri, A. Monguzzi, D. Segala and V. Magni, *Self-starting mode locking of a cw Nd:YAG laser using cascaded second-order nonlinearities*, Optics Letters **20**, 746 (1995).

[180] S. Holmgren, V. Pasiskevicius and F. Laurell, *Generation of 2.8 ps pulses by mode-locking a Nd:GdVO4 laser with defocusing cascaded Kerr lensing in periodically poled KTP*, Optics Express **13**, 5270 (2005).

[181] H. Iliev, D. Popmintchev, I. Buchvarov, S. Kurimura, U. Griebner and V. Petrov, in *Nd:GdVO4 Laser Passively Mode-Locked by Cascaded Nonlinearity in Periodically-Poled Lithium Tantalate*, *OSA Technical Digest (CD)*, Conference on Lasers and Electro-Optics (Optical Society of America, 2010), CMNN3.

[182] C. Schäfer, C. Fries, C. Theobald and J. A. L'huillier, *Parametric Kerr lens mode-locked, 888 nm pumped Nd:YVO4 laser*, Optics Letters **36**, 2674 (2011).

[183] H. Iliev, I. Buchvarov, S. Kurimura and V. Petrov, *1.34 μm Nd:YVO4 laser mode-locked by SHG-lens formation in periodically-poled stoichiometric lithium tantalate*, Optics Express **19**, 21754 (2011).

[184] S. Mukhopadhyay, S. Mondal, S. P. Singh, A. Date, K. Hussain and P. K. Datta, *Dual colour cw mode-locking through soft aperture based on second order cascaded nonlinearity*, Optics Express **21**, 454 (2013).

[185] L. Qian, X. Liu and F. Wise, *Femtosecond Kerr-lens mode locking with negative nonlinear phase shifts*, Optics Letters **24**, 166 (1999).

[186] B. Jacobsson, V. Pasiskevicius and F. Laurell, *Single-longitudinal-mode Nd-laser with a Bragg-grating Fabry-Perot cavity*, Optics Express **14**, 9284 (2006).

[187] T.-y. Chung, A. Rapaport, V. Smirnov, L. B. Glebov, M. C. Richardson and M. Bass, *Solid-state laser spectral narrowing using a volumetric photothermal refractive Bragg grating cavity mirror*, Optics Letters **31**, 229 (2006).

[188] B. Jacobsson, *Spectral control of lasers and optical parametric oscillators with volume Bragg gratings*, Ph.D. thesis, KTH, Laser Physics, 2008.

[189] P. N. Butcher and D. Cotter, *The Elements of Nonlinear Optics* (Cambridge University Press, 1991).

[190] W. Wiechmann, S. Kubota, T. Fukui and H. Masuda, *Refractive-index temperature derivatives of potassium titanyl phosphate*, Optics Letters **18**, 1208 (1993).

[191] K. Fradkin, A. Arie, A. Skliar and G. Rosenman, *Tunable midinfrared source by difference frequency generation in bulk periodically poled KTiOPO4*, Applied Physics Letters **74**, 914 (1999).

[192] K. Kato and E. Takaoka, *Sellmeier and Thermo-Optic Dispersion Formulas for KTP*, Applied Optics **41**, 5040 (2002).

[193] S. Wang, *Fabrication and characterization of periodically poled KTB and RB-doped KTB for applications in the visible and UV*, Ph.D. thesis, KTH, 2005.

[194] G. D. Boyd and D. A. Kleinman, *Parametric Interaction of Focused Gaussian Light Beams*, Journal of Applied Physics **39**, 3597 (1968).

[195] M. Sheik-Bahae, A. Said, T.-H. Wei, D. Hagan and E. W. Van Stryland, *Sensitive measurement of optical nonlinearities using a single beam*, IEEE Journal of Quantum Electronics **26**, 760 (1990).

[196] M. Sheik-Bahae, D. J. Hagan and E. W. Van Stryland, *Dispersion and band-gap scaling of the electronic Kerr effect in solids associated with two-photon absorption*, Physical Review Letters **65**, 96 (1990).

[197] A. G. Selivanov, I. A. Denisov, N. V. Kuleshov and K. V. Yumashev, *Nonlinear refractive properties of Yb3+-doped KY(WO4)2 and YVO4 laser crystals*, Applied Physics B **83**, 61 (2006).

[198] M. A. Solodyankin, E. D. Obraztsova, A. S. Lobach, A. I. Chernov, A. V. Tausenev, V. I. Konov and E. M. Dianov, *Mode-locked 1.93 μm thulium fiber laser with a carbon nanotube absorber*, Optics Letters **33**, 1336 (2008).

[199] W. B. Cho, A. Schmidt, J. H. Yim, S. Y. Choi, S. Lee, F. Rotermund, U. Griebner, G. Steinmeyer, V. Petrov, X. Mateos, M. C. Pujol, J. J. Carvajal, M. Aguiló and F. Díaz, *Passive mode-locking of a Tm-doped bulk laser near 2 μm using a carbon nanotube saturable absorber*, Optics Express **17**, 11007 (2009).

[200] J. DiMaio, S. Rhyne, Z. Yang, K. Fu, R. Czerw, J. Xu, S. Webster, Y.-P. Sun, D. Carroll and J. Ballato, *Transparent silica glasses containing single walled carbon nanotubes*, Information Sciences **149**, 69 (2003).

[201] A. Boccaccini, D. Acevedo, G. Brusatin and P. Colombo, *Borosilicate glass matrix composites containing multi-wall carbon nanotubes*, Journal of the European Ceramic Society **25**, 1515 (2005).

[202] R. Davey, R. P. E. Fleming, K. Smith, R. Kashyap and J. Armitage, *Mode-locked erbium fibre laser with wavelength selection by means of fibre Bragg grating reflector*, Electronics Letters **27**, 2087 (1991).

[203] I. N. Bronstein and K. A. Semendjajew, in *Taschenbuch der Mathematik, 25*, edited by I. N. Bronstein and K. A. Semendjajew (Verlag Harri Deutsch, 1991).

[204] I. Walmsley, L. Waxer and C. Dorrer, *The role of dispersion in ultrafast optics*, Rev. Sci. Instrum. **72**, 1 (2001).

[205] P. Lazaridis, G. Debarge and P. Gallion, *Time-bandwidth product of chirped sech² pulses: application to phase-amplitude-coupling factor measurement*, Optics Letters **20**, 1160 (1995).

[206] F. Träger, in *Springer Handbook of Lasers and Optics*, edited by F. Träger (Springer, 2007).

Part II

Publications